NTech
Lehrstuhl für
Nukleartechnik

Technische Universität München

Technische Universität München

Lehrstuhl für Nukleartechnik

SIMULATION OF THORIUM MATERIAL PROPERTIES UNDER FISSION REACTOR CONDITIONS

José Ignacio Tijero Cavia

Vollständiger Abdruck der von der Fakultät für Maschinenwesen der Technischen Universität München zur Erlangung des akademischen Grades eines

Doktor-Ingenieurs (Dr.-Ing.)

genehmigten Dissertation.

Vorsitzender:	Prof. Dr. Rudolf Neu
Prüfer der Dissertation:	1. Prof. Rafael Macián-Juan, Ph.D.
	2. Prof. Dr. Rudy Konings
	Delft University of Technology

Die Dissertation wurde am 05.04.2017 bei der Technischen Universität München eingereicht und durch die Fakultät für Maschinenwesen am 04.09.2017 angenommen.

A mis padres, Marta y Ramón, por su eterno apoyo,
a mi abuelo Fernando, porque su sentido del humor es la mejor motivación de todas y
a la memoria de mis abuelos

Acknowledgments

I would like to express my gratitude to Prof. Rafael Macián-Juan for his support and help without them I could not overcome all the obstacles and problems that I had to cope with in the beginning of my doctoral work. I would also thank Prof. Rudy Konings for accepting me as his Ph.D. student.

I would also like to acknowledge Dr. Marcus Seidl for his special support, reliability and acceptance as mentor during this long way that is a Ph.D. thesis.

Many thanks to all the people and staff of the Institute of Transuranus Elements in Karlsruhe where I spent the best 6 months in my research work in an extraordinaire, unforgettable and international atmosphere. I would like to highlight from this experience at ITU the collaboration with Paul Van Uffelen, Arndt Schubert and Jacques Van Laar from whom I am eternally indebted for their support, critical view and guide. Without their help I could not have finished this Ph.D. thesis. I must also acknowledge M. Verwerft for his revision and the fruitful collaboration.

I would also like to express my deep acknowledge to all the colleagues at the Lehrstuhl für Nukleartechnik who helped me and with whom I have had a good time during coffee breaks.

Finally, I must express my gratitude to my whole family, especially to my parents who never gave up supporting and encouraging me during my stay here in Germany. I would also like to mention my acknowledge to my sister and my grandfather from whom I really know the bright side of life.

Contents

Acronyms

A

ANL - Argonne National Laboratory
AWBA - Advanced Water Breeder Applications

B

BAPL - Bettis Atomic Power Laboratory
BOL - Beginning of Cycle
BPNWL - Batelle Pacific North-West Laboratories
BWR - Boiling Water Reactor

C

CRAM - Chebyshev rational approximation method

D

DOE - U.S Department of Energy

E

EC - European Commission
ECF - Expended Core Facility
efpds - effective full power days
efph - effective full power hours
EGT - External Gelation of Thorium
EOL - End of Cycle
EPMA - Electron probe microanalysis

F

FBRs - Fast Breeder Reactors
fcc - face-centered cubic

H

HBS - High Burn-up Structure
HM - Heavy Metals
HTGR - High Temperature Gas Reactor
HTR - High-Temperature Reactor
HWR - Heavy Water Reactor

I

IAEA - International Atomic Energy Agency
INEEL - Idaho National Engineering and Environmental Laboratory

J

JAERI - Japan Atomic Energy Research Institute

JRC-ITU - Joint Research Center-Institute for Transuranium Elements

K

KWO - Kernkraftwerk Obrenheim

L

LMFBR - Liquid Metal-cooled Fast Breeder Reactor
LWBR - Light Water Breeder Reactor
LWR - Light Water Reactors

M

MCNP - Monte Carlo N-Particle
MOX - Mixed Oxides
MSBR - Molten Salt Breeder Reactor
MSID - Mass Spectrometric Isotopic Dilution
MSR - Molten-Salt Reactor
MTR - Material Testing Reactor

N

NEA - Nuclear Energy Agency

O

OECD - Organisation for Economic Co-operation and Development
OMICO - Oxide Fuels: Microstructure and Composition Variations
ORNL - Oak Ridge National Laboratory

P

PCMI - Pellet-Cladding Mechanical Interaction
PHWR - Pressurized Heavy Water Reactors
PIE - Post Irradiation Experiments
PSI - Paul Scherr Institute
PWR - Pressurized Water Reactor

R

RBWR - Reduced Moderation Boiling Water Reactor

S

SAPS - Shippingport Atomic Power Station
sc - simple crystal
SCK•CEN - Studiecentrum voor Kernenergie•Centre d'étude de l'énergie Nucléaire
SIMFUEL - Simulated Fuel
SKI - Swedish Nuclear Power Inspectorate

T

TC - Thorium Cycle

TD - Theoretical Density

TEM - Transmission Electron Microscopy

TUBRNP - Transuranus Burn-up

V

vic-pac - vibratory compaction

Y

YSH - Yttrium Stabilized Hafnia

List of Figures

List of Tables

Abstract

This thesis aims at the extension of the applicability of the TRANSURANUS fuel performance code to thorium-based fuels. Two thoria fuels have separately been studied during this work: (Th,Pu)O_2 and (Th,U)O_2. The implementation of both fuels in TRANSURANUS was done in three parts: (i) a revision of the correlations of the material properties, (ii) the extension of the TRANSURANUS burn-up model, and (iii) the modification of the fission gas release parameters.

Recent updated correlations, both from laboratory measurements along with new post irradiation experimental data obtained at JRC-ITU (Joint Research Center-Institute for Transuranium Elements) and from open literature, were used in the implementation of the thermo-mechanical properties in the TRANSURANUS source code which are: Elasticity constant, Poisson's ratio, strain due to swelling, thermal strain, thermal conductivity, creep strain, yield stress, rupture strain, heat capacity, density, solidus-liquidus melt temperature, heat of melting, emissivity and fraction of heavy metals.

An extension of the standalone TUBRNP (Transuranus Burn-up) version for thorium fuels was developed by completing the depletion equations for the most relevant nuclides ^{232}Th, ^{233}U and ^{234}U and the extension of breeding of ^{235}U through a sequence of neutron absorption reactions, involved in the thorium cycle. The update of the one-energy group effective cross section for neutron radiative capture and neutron-induced fission, which are burn-up and radially averaged, was done with the help of the 2-D continuous-energy Monte Carlo code Serpent. The absorption in the range of epithermal energies of neutrons is accounted by introducing a power-shape radial functions in the set of the Bateman equations for the nuclides ^{240}Pu and ^{232}Th. An analytical method is presented to derive these functions from Serpent simulations.

The modification of the most representative parameters for the fission gas release in TRANSURANUS was carried out by the extension of the a-thermal model, the review of the effective diffusion coefficient that leads the intra-granular treatment in TRANSURANUS and the surface tension and grain boundary tension that calculates the dihedral angle in the inter-granular treatment.

The validation of TUBRNP for (Th,Pu)O_2 type fuels was carried out in two steps. A comparison of the normalised radial distributed concentrations of Th, U, Pu, Nd, Xe and Cs between TUBRNP, Serpent and EPMA (Electron probe microanalysis) data points measured on a sample from a rodlet irradiated at KWO (Kernkraftwerk Obrenheim) allows checking the correctness in the derivation of the radial functions. In a second step, a comparison of the radially averaged values of the same elements between TUBRNP, Serpent, EPMA and benchmark codes under same conditions indicates the agreement in the computation of the one-group

cross sections.

On-line fuel centre temperature measurements and PIE (Post Irradiation Experiments) on the gap size of a rodlet irradiated in the Beryllium-moderated experimental reactor at the SCK•CEN (Studiecentrum voor Kernenergie•Centre d'étude de l'énergie Nucléaire) as part of the OMICO project were utilized to validate graphically and quantitatively the full version of TRANSURANUS at low burn-up for (Th,Pu)O_2 fuels.

For (Th,U)O_2 fuels isotopic compositions measured in a rod segment from the LWBR (Light Water Breeder Reactor) Shippingport irradiation programme were employed to validate the calculation of the 1-g cross sections in TUBRNP for this type of fuel. As part of the same irradiation programme, the fission gas release rate measured by puncture in a fuel rod irradiated at the Shippingport LWBR in the United States was used to validate the extended athermal fission gas release treatment in TRANSURANUS.

1

Introduction

The use of thorium in nuclear reactors has always been considered since the 50s when the nuclear industry was developed for the purpose of power generation. From 1977 to 1982 a PWR (Pressurized Water Reactor)-based core at the Shippingport power station in Pennsylvania, USA was loaded with assemblies of (Th,U)O_2-ThO_2. In Germany, more concretely in Hamm, thorium-based pebbles were irradiated in the final core of the THTR-300, a HTR (High-Temperature Reactor) from 1983 to 1989 [33, 26]. Nonetheless, despite of all of those tests and the effort done by world-wide institutions, thorium has never reached a degree of development as uranium or MOX (Mixed Oxides) fuels.

Nowadays, the interest in thorium has been risen again due to the intention of developing safe and clean fuels with which the nuclear industry can cope with the current power generation challenges. In India, where it is thought to exist abundant thorium resources, thorium-based pellets are being tested in experimental reactors. Furthermore, there is an ongoing project to run a MSR (Molten-Salt Reactor) that contains a thorium-based blanket [34]. In Norway, the company ThorEnergy recently launched the program "Seven-Thirty" [35] that comprises the fabrication and later irradiation in the experimental HWR (Heavy Water Reactor) in Halden of (Th,U)O_2-(Th,Pu)O_2 pellets. The EC (European Commission) has supported economically the experimental test of thorium fuels in two projects, Thorium Cycle [2, 19] and OMICO [31, 32] and their PIE as part of the LWR (Light Water Reactors) Deputy [36].

The application of thorium as nuclear fuel lies in the potential breeding of ^{233}U through a neutron capture (Equation 1.1) and its posterior neutron-induced fission to generate the power expected. ^{233}U, as a fissile nuclide in a nuclear reactor, possesses two main advantages with respect to the conventional ^{235}U and ^{239}Pu. On one side, less fissile content is employed to sustain the chain due to the improvement of the neutronic economy and on the other side, the production of high toxic heavy actinides from ^{239}Pu radiative capture is considerably reduced. However, the breeding of ^{232}U through a (n,2n) reaction from ^{233}U is regarded as the main disadvantage because this isotope is the head of a high gamma emitters chain.

$$^{232}Th \xrightarrow{n,\gamma} {}^{233}Th \xrightarrow{\beta^-} {}^{233}Pa \xrightarrow{\beta^-} {}^{233}U \tag{1.1}$$

Since ^{232}Th is a fertile material, an external nuclide that produces that neutron is required to start up the cycle. To this end, ^{233}U, ^{235}U or ^{239}Pu are initially added to the pure ThO_2 in order to be burned out in the first stages of the irradiation of the fuel. For example, plutonium weapon-grade produced in MOX reactors can be incinerated in thorium-based fuels,

contributing in this way to non-proliferation purposes.

The simulation of the nuclear fuel behaviour is important for licensing purposes and for interpreting experiments with new fuels. It involves the assessment of temperature distributions and stresses, as well as the evolution of the various fissile and fertile isotopes. TRANSURANUS is a fuel performance code developed at the JRC-ITU in Karlsruhe and written in the FORTRAN language that simulates the behaviour of a single fuel rod under operation or transient conditions given the irradiation history [37]. TRANSURANUS makes use of experimentally-derived correlations for a set of thermo-mechanical properties for different type of fuels such us MOX or uranium carbides.

The standalone TRANSURANUS burn-up model TUBRNP computes the local power density and the burn-up [38, 39, 40]. It is derived from the RADAR model [41] and is used in other fuel performance codes like Frapcon [9]. In TUBRNP the Bateman equations for the most representative nuclides are solved incrementally by using the one-group effective cross sections for neutron capture and neutron-induced fission with the thermal neutron flux calculated by solving the diffusion equation derived from the neutron transport equation. The strong absorption of neutron in the epithermal region of neutron energies in ^{240}Pu and ^{238}U is accounted by inserting power-shape radial profiles.

This thesis describes the extension of TRANSURANUS to thorium containing oxide fuels and its validation with experimental data from different research programmes. In the following chapter a summary of the utilization of thorium as nuclear fuel is described as well as its advantages and disadvantages. In the third chapter, a survey of the correlations of the thermo-mechanical properties for (Th,U)O_2 and (Th,Pu)O_2 is reported. The thermo-mechanical properties employed in TRANSURANUS are: Elasticity constant, Poisson's ratio, strain due to swelling, thermal strain, thermal conductivity, creep strain, yield stress, rupture strain, heat capacity, density, solidus-liquidus melt temperature, heat of melting, emissivity and fraction of heavy metals. The application of the Vergard's law as a linear interpolation between pure oxides is seen as the most accurate approach for the full correlation for the ceramic compounds in cases where there are no combined correlations published.

In the fourth chapter of the thesis, the extension the applicability of TUBRNP to thorium-based fuels is explained. To this end, the depletion equation of ^{232}Th, ^{233}U and ^{234}U has been incorporated as well as the breeding of ^{235}U through neutron capture from ^{234}U. 2-D simulations performed with the multi-group Monte Carlo code Serpent [42] were carried out to calculate the one-group effective cross section and the radial strong absorption functions for ^{232}Th and ^{238}U in contrast to the experimental fit of these functions previously applied for conventional fuels.

In the fifth chapter, the last analysis of the performance of a nuclear fuel is the behaviour of the release of fission gases born after the fission events. During the irradiation of the fuel,

several mechanisms are clearly distinguished [43] which are grouped in TRANSURANUS in four treatments: athermal, intra-granular, inter-granular and HBS (High Burn-up Structure). The extension of the three first treatments for thorium-based fuel was carried out since there are no data of HBS reported for thorium fuels.

The validation of the first version of TRANSURANUS for thorium fuels is done in the following chapters. In chapter number six, the validation of TUBRNP for (Th,Pu)O_2 was done by comparing the results from the simulations to measurements performed in a sample irradiated during the Thorium Cycle project [44]. The validation was done in two separated steps, on one side, the comparison between the both codes and the experimental data of the radial averaged concentrations of the elements Th, U, Pu, Nd, Xe and Cs have proven that the computation of the one-group cross sections was successfully achieved and on the other side the graphical comparison of the normalized radial profiles of the aforementioned elements stands for the successful approach of deriving the radial profile functions from Serpent analytically.

In the seventh chapter, on-line centre temperature recorded in instrumented rods B_i and H_i irradiated at SCK•CEN [31, 32] as well as gap size measured in rod B_i in the framework of OMICO project were utilized to validate the full version of TRANSURANUS for (Th,Pu)O_2 fuels. A parallel comparison of these results to the analysis done in the MOX rod G_i concluded that the TRANSURANUS thorium fuels version has reached a level of refinement comparable to uranium-MOX fuels already validated.

In the eighth chapter, the validation of (Th,U)O_2 was done. The TRANSURANUS version for (Th,U)O_2 fuels could only be validated by means of the numerical comparison of radially averaged isotopic concentrations obtained from the data reported from the Shippingport programme [21]. Furthermore, from Shippingport reports, the fission gas release rate value measured by puncture in the rod-N was contrasted to the extension of the TRANSURANUS Turnbull's athermal fission gas release model previously implemented.

In the last section of the thesis, the outcome and perspectives are summarised, as well as two appendices and the bibliography used along this work.

2

Thorium as nuclear fuel

Thorium was discovered by the Swiss chemist Jöns Jakob Berzelius in 1828 in the analysis of a mineral found in Norway and was named after the Norse god of thunder, Thor [1, 45]. The utilization of thorium as a potential nuclear fuel has always been recognized since the development of the nuclear industry in the mid of 50s. The two main reasons that make thorium attractive as nuclear fuel are its abundance on the crust and the breeding of ^{233}U through neutron capture.

Country	Tonnes	Percentage
Australia	489000	19
USA	400000	15
Turkey	344000	13
India	319000	12
Venezuela	300000	12
Brazil	302000	12
Norway	132000	5
Egypt	100000	4
Russia	75000	3
Greenland	54000	2
Canada	44000	2
South Africa	18000	1
Other countries	33000	1

Table 1 Resources of thorium per country [24]

Thorium is found in association with oxygen forming the minerals thorite $ThSiO_4$ [8, 46], thorianite ThO_2 [8] or in combination with uranium uranothorianite (Th,>50%U)O_2 [45]. However, the most common source of thorium is as substitute of La or Ce in monazite (Ce,La)PO_4

whose thorium content can be found to be between 3.5 and 10% [47]. In contrast, the content of uranium in monazite is reported to be between 0.1 and 0.4% [45], clearly lower than thorium. In addition to the larger abundance, thorium is also more widely distributed on the Earth crust than uranium ores. Table 1 sorts the known thorium resources in the world for different countries [24].

As can be seen in the full thorium cycle represented in Figure 1, through a neutron capture in ^{232}Th and two beta decays of 22.2 minutes and 27 day of ^{233}Th and ^{233}Pa respectively, finally ^{233}U is bred. Since ^{232}Th is a fertile actinide, a fissile material like ^{233}U, ^{235}U or ^{239}Pu is required to add to the thorium matrix to produce the primary neutrons and start up the cycle.

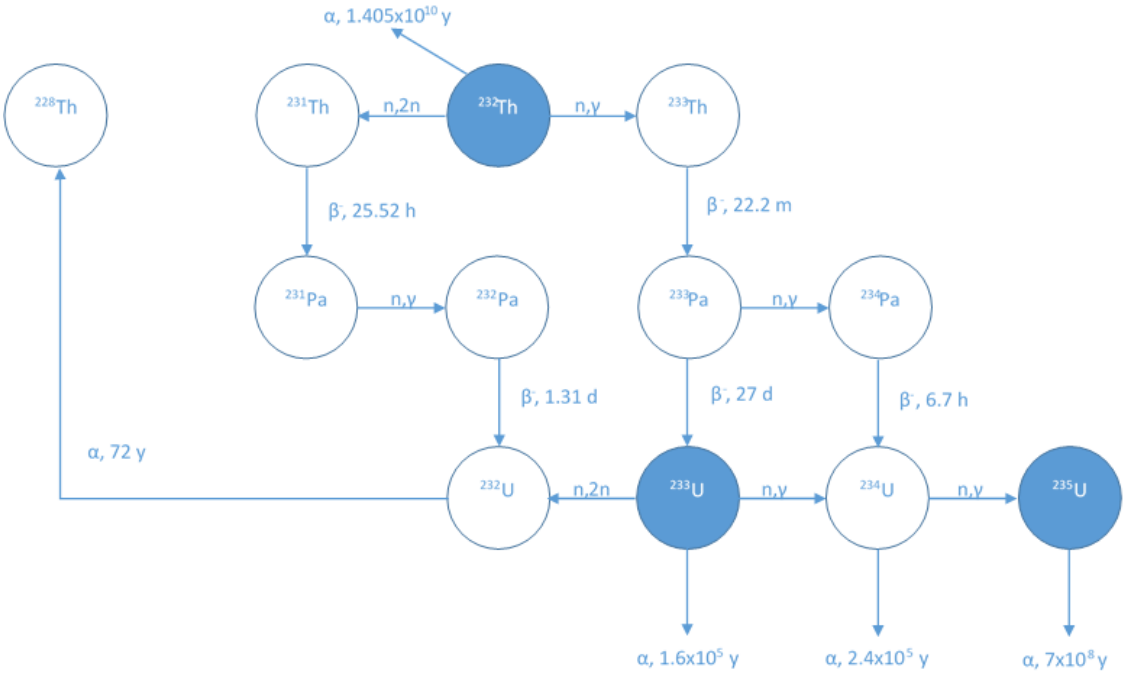

Figure 1 Thorium cycle

Table 2 lists the microscopic fission and capture cross section, σ_f and σ_c, the average neutrons born after fission, ν, and the fission factor, η, for ^{233}U, ^{235}U and ^{239}Pu. The advantage of ^{233}U with respect to the conventional fission actinides relies on its larger fission factor. For a incident neutron energy of 0.025 eV, within the thermal range, the η for ^{233}U calculated by Lung [1] is 2.27, larger than 2.04 and 2.12 for ^{235}U and ^{239}Pu respectively. A large fission factor means that for a given number of fissions there is a much smaller burn of ^{233}U than for either of the other two fissile elements. The importance of the neutrons born after fission, ν, lies in the fact that the higher this number is, the less fuel atoms are needed to sustain the chain reaction. For ^{233}U, the number of neutrons produced after the destruction of the atom (2.5) are similar to ^{239}Pu that possesses the largest value (2.9) at these energies.

	^{233}**U**	^{235}**U**	^{239}**Pu**
σ_f (barns)	527	579	741
σ_c (barns)	54	100	267
ν	2.5	2.4	2.9
$\eta = \frac{\nu\sigma_f}{\sigma_f+\sigma_c}$	2.27	2.04	2.12

Table 2 Comparison of fission factors

As can be appreciated in Table 2, ^{239}Pu has also the largest fission cross section, σ_f among the actinides compared, with a value of 741 barns. A high fission cross section entails that fewer neutrons are lost by being captured by non-fissile materials in the fuel or in the structure [1]. However, the capture cross section of ^{239}Pu is the largest, 267 barns, implying a high possibility of producing ^{240}Pu, whose capture cross section is also high, leading to the possibility of building up new heavier isotopes such as Cf or Am. Thus, as irradiation proceeds, the likelihood of neutron capture increases and the amount of ^{239}Pu to provide sufficient reactivity is correspondingly decreased [1]. ^{235}U can be seen as an intermediate nuclide among the others regarding the neutronic properties due to its fission cross section, which is larger than ^{233}U but in contrast its capture cross section is two times that of ^{233}U and a sequence of neutron captures will not breed any further fissile isotopes of interest.

The presence of ^{233}Pa is particularly important due to the impact produced by this isotope in the thorium cycle. As can be seen in Figure 1 the half-life of ^{233}Pa is is 27 days, large enough to open the likelihood that a radiative capture reaction in this nuclide would occur with a non-dismissable capture cross section in the thermal region of 40 barns [1]. By capturing a neutron in ^{233}Pa, ^{233}U is no longer bred and, instead, ^{234}Pa is produced, which immediately decays to ^{234}U (6.7 hours) reducing the amount of fissile material in the fuel. ^{233}Pa must also be taken into account after reactor shutdown when it provides the main source of radioactivity from the actinide group and the breeding of ^{233}U introduces a positive reactivity in the reactor that may affect the operation of the reactor margins. In fast reactors where neutrons have a high kinetic energy around 1 MeV, the breeding of ^{234}Pa can be dismissed because the radiative capture cross section of ^{233}Pa is negligible. Beside other reasons, this also makes thorium very attractive for fast reactors.

The main drawback in the thorium cycle lies in the breeding of ^{232}U through the (n,2n) reaction of ^{233}U. ^{232}U is at the head of decay chain as depicted in Figure 2 [1]. Except the first two members, ^{232}U and ^{228}Th, all the nuclides have very short half-lives. The most important gamma emitters are ^{208}Tl and ^{212}Bi, with 2.6 and up to 1.8 MeV gamma energy decay and very short half-lifes of 3.1 and 60.6 minutes respectively [1]. ^{212}Po comes from ^{212}Bi through β^- decay (66.3 $\%$) with the gamma emission range previously mentioned. ^{212}Po then decays

to ^{208}Pb by emitting an α particle with an immediate half-life of 0.3 μs. The high energized gamma particles, with the very short decay time of almost all the members of the decay chain and the impossibility of separating ^{232}U from ^{233}U make the presence of ^{232}U a real disadvantage for handling irradiated thorium-based fuel. However, the aforementioned (n,2n) reaction is very unlikely to happen since the cross section of the reaction is very small in the thermal range. In the resonance region where FBRs (Fast Breeder Reactors) are operated the possibility that this reaction takes places is even smaller. For this reason, the usage of thorium in FBRs is also an attractive option.

Thorium fuel fabrication would not present many difficulties since UO_2 or MOX techniques, which have been mastered over the years, may in principle be adopted. The necessity of adding an initial high fissionable material such as ^{233}U, ^{235}U or ^{239}Pu requires the same safety measurements, like glove box and shielding, as already established for MOX fuels. Furthermore, the possibility of building-up ^{232}U and its consequent high gamma decay chain implies the need for extra gamma ray shielding. The higher melting point of ThO_2 (around 3600 K [48]), larger than UO_2 (approximately 3120 K [48]), is regarded as the main disadvantage that thorium fuel fabrication presents. Although this high melting point will avoid fuel melting during irradiation, for fuel manufacturing it is seen as an impediment due to the requirement of high sintering temperatures (around 2000°C) in order to obtain high-density pellets and prevent grain pull-out during its irradiation. Small additions of Nb_2O_5 or U_3O_8 will contribute in the reduction of the sintering temperature to below 1200°C [47].

One of the the first techniques developed for fuel fabrication was the powder-pellet route, whose essential steps are milling, granulation and binder addition, cold pelletization and sintering [47]. This process was used in the manufacture of fuel pellets that were then irradiated at Shippingport power station. The generation of radiotoxic aerosols by handling large amount of fine powders (< 1μm) is the main disadvantage presented in this process [49].

The sol-gel process (Figure 3) avoids the generation and handling of the fine powder by involving the usage of liquids and dust-free microspheres, which results, at the end, in an excellent microhomogeneity of the fuel. For example, this technique was utilized in the preparation of the rodlet irradiated at KWO [2]. This technique can be incorporated in reprocessing plants and its steps can also be enhanced and remotely controlled. The EGT (External Gelation of Thorium) was developed in Germany for the HTGR (High Temperature Gas Reactor) and it differs from sol-gel in the utilization of inflammable and high radiolytical stable ammonia and ammonium hidroxyde for the preparation of the solutions [47]. A slight modification of this later technique is the ammonia internal gelation process in which the thorium, uranium and plutonium are mixed with hexa methylene tetra amine $(CH_2)_6N_4$ that finally releases ammonia used for the pellet preparation. The pressing stage of the sol-gel process can also be improved by introducing the vic-pac (vibratory compaction). A combination of the powder-pellet and sol-gel process called sol-gel pellezitation technique uses dust-free sol-gel derived microspheres instead of powder, thus overcoming the problems emerged by the use of radiotoxic

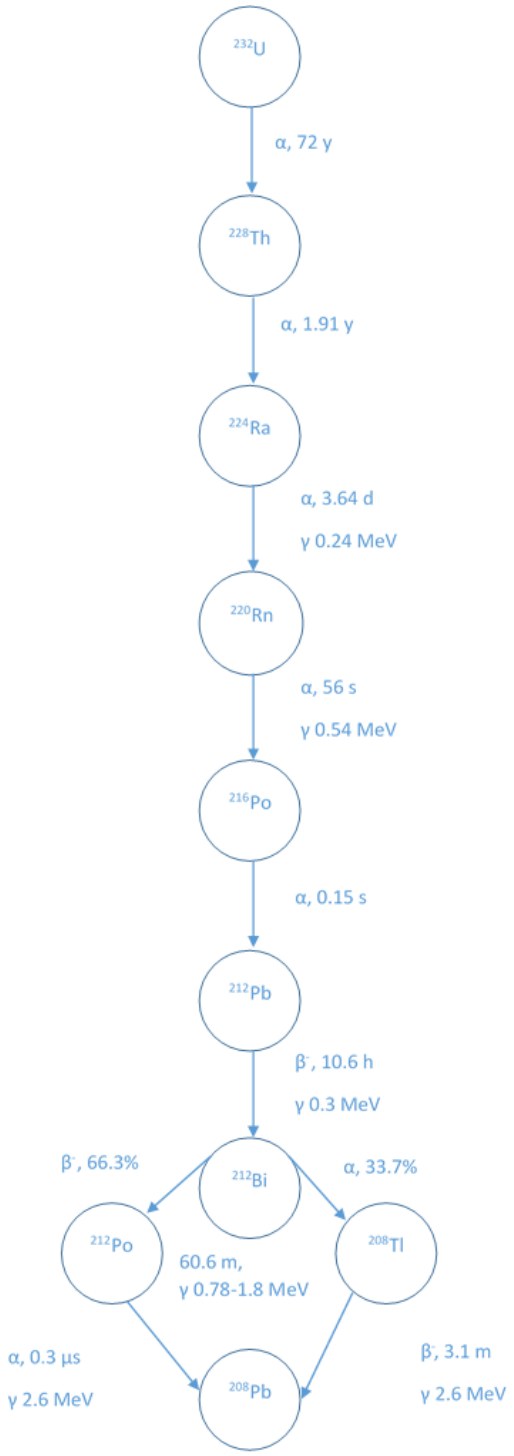

Figure 2 ^{232}U decay chain [1]

powder. This process is ideally suited, for instance, for (Th,^{233}U)O_2 [49]. A simplification of the sol-gel manufacture process is the impregnation technique in which firstly high porosity ThO_2 pellets are manufactured and then impregnated with uranyl nitrate followed by sintering to obtain high density pellets [34]. The high melting point of thorium was the reason of coating thorium-based ceramic in graphite matrix. This process was developed in Germany and used for HTGR as well.

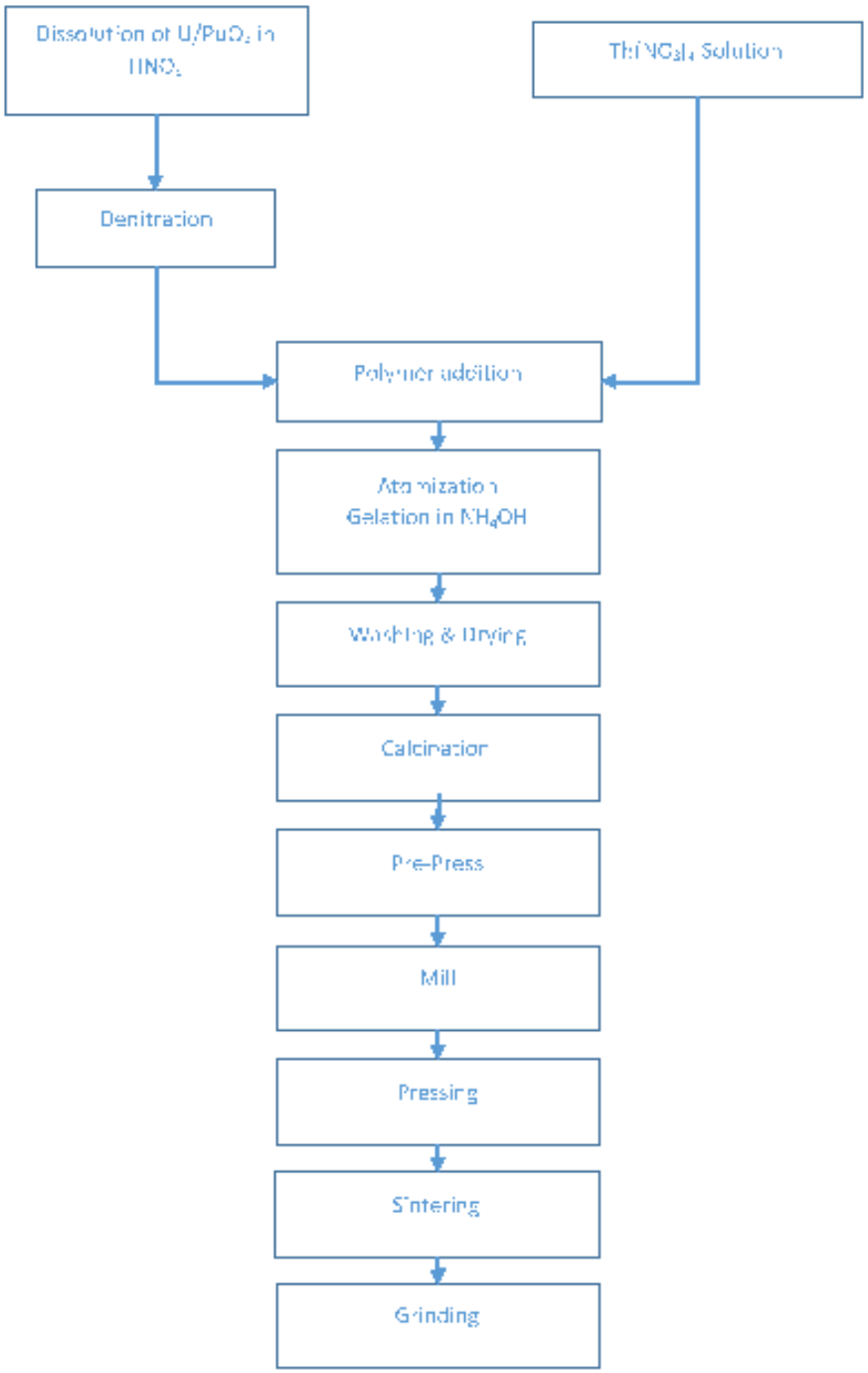

Figure 3 Sol-gel flow chart [2]

Thorium-based fuels have been tested and studied along the nuclear industry history. The first use of thorium reported was in the USA at the Borax IV (2.4 MW(e)) & Elk River Reactors (24 MW(e)) from 1963 to 1968, where (Th,^{235}U)O_2 pellets were mounted in BWR (Boiling Water Reactor) assemblies. Later in 1977 at the Shippingport power station a full Light Water

Breeder core of ThO_2-(Th,U)O_2 was operated until its decommissioning in 1982. Also in USA but at ORNL (Oak Ridge National Laboratory) the first MSBR (Molten Salt Breeder Reactor) was tested from 1964 to 1969 with a thermal output energy of 7.5 MW_t. Again in USA prismatic blocks of made of (Th,^{235}U)O_2 coated fuel particles oxide and dicarbide were irradiated at Peach Bottom and Fort St. Vrain from 1966 to 1972 and 1976 to 1989 respectively. In Europe, (Th,^{235}U)O_2 coated fuel particles oxide included in a pin-in-block design [47] were irradiated at the Dragon reactor in UK as part of an OECD (Organisation for Economic Co-operation and Development)-Euroatom programme from 1966 to 1973. In Germany, pebbles of this type of fuel were also irradiated in the HTGR of AVR and THTR from 1967 to 1988 and 1985 to 1989 respectively [33]. Further in Germany, the first (Th,Pu)O_2 based pin fuels were tested in a BWR in Lingen in 1973. In Netherlands aqueous homogeneous pin assemblies of Th+HEU [34] were irradiated at SUSPOP/KSTR KEMA from 1974 to 1977 [47]. In Canada, fission gas release analysis were performed on 1-3% enriched thorium-uranium oxide samples subjected to power ramps at CANDU-type rectors in 1985 [33]. Despite all of these tests, thorium has never used and produced as nuclear fuel at an industrial scale and after Chernobyl accident, the research in new fuels almost disappeared.

Nowadays with the increased environmental awareness, thorium has recovered its importance as nuclear fuel. The EC has funded the TC (Thorium Cycle) [2] and OMICO [32, 31] in which (Th,Pu)O_2 test rodlets were irradiated under PWR conditions as part of the EURATOM 5^{th} Framework Programme for Research and Training in the field of Nuclear Energy (1998 - 2002). In Norway the company Thor Energy recently launched the program ”Seven-Thirty” that aims the manufacture and posterior test of (Th,U)O_2 and (Th,Pu)O_2 pins at OECD Halden Reactor [35].

In India, thorium properties and reprocessing aspects have been studied. The fabrication of aluminium clad ’J’ rods containing Al-ThO_2 pellets and their irradiation at the MTR (Material Testing Reactor) of CIRCUS was carried out in order to process the alloy Al–20%^{233}U for further analysis. Furthermore, Zircaloy clad test–pin assemblies containing (Th, Pu)O_2 and 4–7% PuO_2 pellets have successfully been irradiated up to burn-ups of 18000 MWd/t HM (Heavy Metals) without any failure [47]. ThO_2 pin assemblies with Zircaloy clad were introduced in the PHWR (Pressurized Heavy Water Reactors) KAPS 1 and 2, KGS 1 and 2, RAPS 2, 3 and 4 in order to flatten the neutron flux [34]. The ^{233}U obtained by reprocessing was lately applied in Th–20%U, Th–20%Pu, Th–20%Pu–4%U and Th–20%Pu–4%U–8%Zr fuel pins in LMFBR (Liquid Metal-cooled Fast Breeder Reactor) with excellent safety features, however the ^{233}U conversion factor reported was smaller than in PHWR [47].

The PUREX reprocessing method used for MOX fuels to separate U from Pu is adapted to thorium fuels with the name THOREX reagent and target. The distinction between both processes is the medium to dissolve spent thorium fuel. While in PUREX the wasted fuel can be dissolved in nitric acid, the thorium-based spent fuel is dissolved in THOREX reagent (13 M HNO_3 + 0.03 M F^- + 0.1 M Al^{3+}) due to its high matrix stability that practically renders tho-

rium insoluble in this acid [33]. This reprocessing method is strongly being studied, designed and enhanced in India [34].

The construction of a MSR with thorium in a mixture of ^{7}LiF, BeF_2 and Zr_2F_4 has always been projected because this type of reactor works in the epithermal range of neutrons, the best region for ^{233}U fissions, and purges volatile fission products and noble gases trapped in a charcoal bed [1]. However, the construction of this type of reactor is still under development and design.

3

Material properties

A review of the material properties for the thorium-based fuels, (Th,Pu)O_2 and (Th,U)O_2, was carried out in order to select the most accurate and recent correlations for material properties. The material properties that TRANSURANUS makes use of are: Elasticity constant, Poisson's ratio, strain due to swelling, thermal strain, thermal conductivity, creep strain, yield stress, rupture strain, heat capacity, density, solidus-liquidus melt temperature, heat of melting, emissivity and fraction of heavy metals. A considerable effort was made to find the correlations that account for the concentration of the pure oxides and other effects that may have an impact on them. This is the case, for instance, of thermal conductivity, whose applied correlation was a simpler model than the formulas used for the other nuclear fuels. For creep strain, the UO_2 correlation was adopted for thorium mixed fuels due to the lack of information on this property for thorium in the literature. For yield stress and rupture strain, the inferred correlations of ThO_2 were applied for (Th,Pu)O_2 since there are no data available for PuO_2. In Young's modulus and emissivity, approximation factors were introduce to derive the mentioned properties for PuO_2 and ThO_2 from MOX and UO_2 fuels respectively. In most of the cases, when the correlation that accounts for the concentration of the pure oxides is not published, a linear interpolation between the oxides by using Vergard's law was recommended according to Belle [8] (See Equation 3.1).

$$\begin{aligned} X_{(Th,Pu)O_2} &= X_{ThO_2}(1 - y_{PuO_2}) + X_{PuO_2} y_{PuO_2} \\ X_{(Th,U)O_2} &= X_{ThO_2} y_{ThO_2} + X_{UO_2}(1 - y_{ThO_2}) \end{aligned} \tag{3.1}$$

The interpolation variable for both mixed oxides differs. For (Th,Pu)O_2 the interpolation variable selected was the concentration of PuO_2, y_{PuO_2}, already declared and used for MOX cases. In contrast, for (Th,U)O_2 fuels the concentration of ThO_2, y_{ThO_2}, was chosen instead, because its computation in TRANSURANUS results easier than summing up all the isotopes of U. These concentrations are usually expressed in moles or atoms but can also be introduced in weight fraction. X is referred to any of the previously mentioned properties.

The Vergard's law states that the unit cell of size of cubic solid solutions varies linearly with molar composition [8]. Actinides such as Pu, Th or U in combination with oxygen form oxides solutions as fluorite-type lattice structure, i.e. a polycrystalline system that contains eight atoms of oxygen placed in a sc (simple crystal) structure within a fcc (face-centered cubic) structure where the four actinides atoms are placed (see Figure 4). The extension of the application of Vergard's law to any other property in thorium-based fuels is based on the inappreciable modification of the lattice volume of a ThO_2 solution due to UO_2 and PuO_2

have also the same lattice structure. Indeed, all tetravalent ions have similar radii, 5.5975, 5.4705 and 5.396 Å for Th^{+4}, U^{+4} and Pu^{+4} [8], and the substitution of a thorium cation by a uranium or plutonium cations will barely not affect its volume and structure.

Bakker et al. [50] stated that at high temperatures both ThO_2 and UO_2 ceramic oxides lattice parameters linearly decrease according to vapour pressure measurements that indicated that ThO_2 and UO_2 oxydes behave as ideal solutions. Therefore, he considered that both actinide oxides forms an ideal solid solution in the whole range of concentrations. Consequently, he recommended the employment of a linear interpolation by means of the application of the Vegard's law, Equation 3.1, for the material properties correlation for $(Th,U)O_2$ and $(Th,Pu)O_2$ fuels, reinforcing Belle's recommendation. The Vergard's law is named Neumann-Kopp's rule when a linear interpolation is applied for the heat capacity [25].

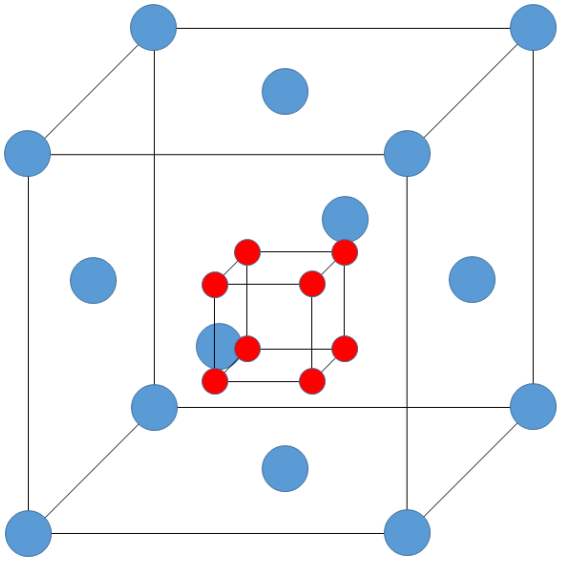

Figure 4 Cubic fluorite lattice structure for a MO_2, where M (blue) can be either Th, U or Pu. The oxygen atoms are represented in red

3.1. Elasticity constant

Figure 5 represents the stress-strain curve for a ceramic material. Up to point 'C', a stress applied to a sample is proportional to the strain that the sample is subjected. This region is well-recognized as Hook's law (Equation 3.2) where the proportional constant E between the stress σ and the strain ϵ stands for the elasticity or Young's modulus.

$$\sigma = E\epsilon \tag{3.2}$$

The behaviour of a material under Hook's law is known as elastic deformation, i.e. a material exposed to a stress will recover its original volume once the stress is no longer applied.

The earliest measurements of Young's modulus at different temperatures done by Spinner [51] in samples of pure ThO_2 with a certain variety of fabrication porosity showed that the elasticity modulus linearly decreases with the temperature. Spinner also reported the linear relationship between the elasticity constant and the porosity.

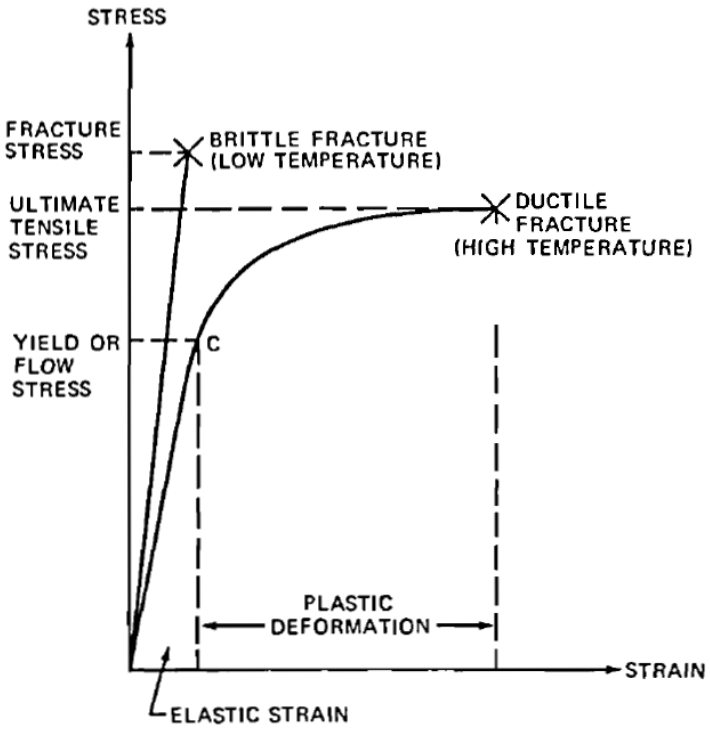

Figure 5 Stress-strain curve from Olander [3]

The Vegard's law (Equation 3.1) was employed to derive the correlation of the Young's modulus for (Th,U)O_2 and (Th,Pu)O_2 fuels from the expressions of the ThO_2, UO_2 and PuO_2 compounds [8]. The correlation implemented for ThO_2, Equation 3.3, was extracted from the Gmelin's book [4] and was also applied in the extension of FRAPCON to thorium fuels [10]. In this correlation the elasticity modulus linearly depends on the temperature and the porosity.

$$E_{ThO_2} = 253(1 - 2.21P)(1.003 - 1.405 \times 10^{-4} T_c) \tag{3.3}$$

The value of $253(GPa)$ is the elastic modulus at room temperature (25°C), T_c is the temperature in Celsius and P is the porosity expressed in units, whose range of validity is between 0.06 and 0.4 according to Belle [8]. Spinner [51] suggested a second order polynomial for the relationship between the Young's modulus and the porosity. However, Wolfe and Kaufman (1967) analysed these data and proposed a linear relationship between Young's modulus and porosity as reported by Hart [5]. Belle [8] also agreed with Wolfe and Kaufman and reported the selected correlation as shown in Equation 3.3. On the other side, Hart [5] and Belle [8] coincided with Spinner [51] in the temperature correlation. In that work, the temperature term is also multiplied by an exponential function of the temperature ($e^{-\frac{181}{T(K)}}$). Nevertheless, a

graphical comparison (see Figure 6) of both correlations only shows a small divergence at high temperatures between both correlations. Therefore, Gmelin's formulation was finally implemented in order to avoid possible problems in the computation of the exponential term in TRANSURANUS. Although the correlation of ThO_2 published by Hoch [52] presents a similar linear behaviour in the temperature term, as can be appreciated by comparing the slopes in Figure 6, the term measured at room temperature completely disagrees with the two previously expression. Therefore, this expression was also dismissed for this type of solid.

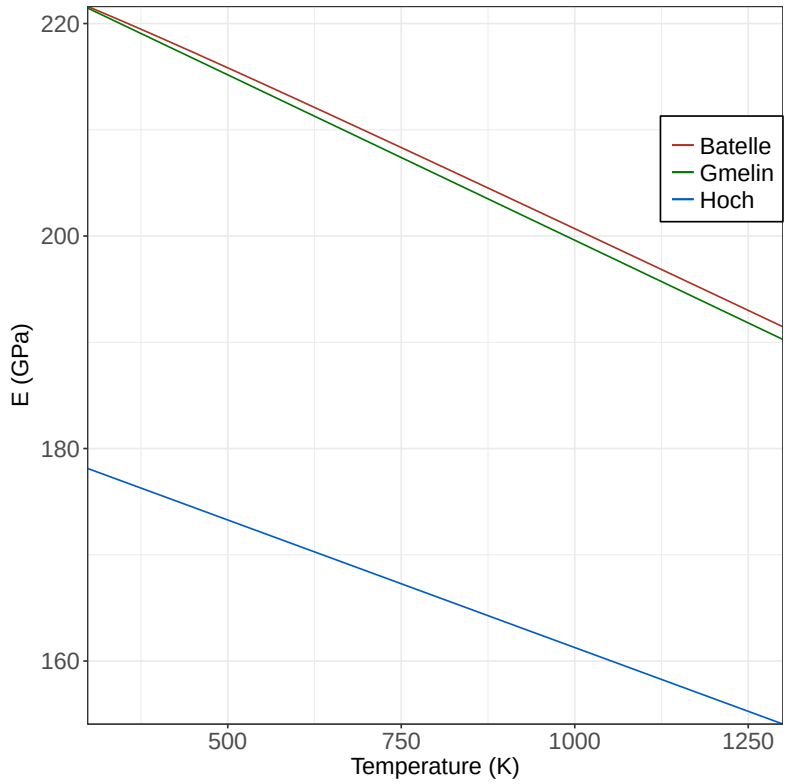

Figure 6 Comparison of the correlations for ThO_2 extracted from Gmelin's book [4] and Batelle report [5] at 5% of porosity

It is worth mentioning that Spinner observed a shortfall in the ThO_2 Young's modulus above 1300 K due to grain boundary relaxation [51]. Olander stated that the slide of two grains along their common grain boundary is produced by the movement of a common ledge on the grain boundary from the tensile side to the compressive side [3]. A ledge is a non-uniformity on the grain boundary of the same type found on external surfaces of solids commonly named as roughness [3]. The deformation due to sliding of grains past each other along the grain boundaries is a complementary phenomenon of the deformation of grain when the sample is under stress. This relaxation is caused by sliding along the grain boundaries and might be minimised by increasing the grain size [8], however this is not clear because with small grain size, the grain boundaries surfaces are thus smaller and the sliding phenomenon ought not to happen. The expression of this shortfall, Equation 3.4, was first derived by Spinner considering a second order polynomial function on the porosity term. For further details see

[51].

$$\frac{E_{ThO_2}}{E_{calc}} = 0.5\left(\frac{7+5\mu}{7+\mu-5\mu^2}\right) \tag{3.4}$$

E_{ThO_2} is the real Young's modulus and E_{calc} is the evaluation of the modulus from Equation 3.3, both expressed in GPa. μ is the Poisson's modulus. The correlation previously mentioned [5, 8] accounts for this deviation to viscous state in the exponential term. A shortfall of 50 % in the elasticity modulus is attained when μ takes the value of 0.28.

This shortfall of the elasticity modulus for ThO_2 materials was not implemented in TRANSURANUS because of two reasons: first, no recent measurements have been carried out regarding this property that would allow to contrast Spinner's observations. Secondly, the assumption of a second order polynomial dependency on the porosity in the derivation of the expression resulted in Equation 3.3 would not be consistent with the accepted linearity in the porosity term [4, 8, 10].

Equation 3.5 is the correlation selected for the UO_2 elasticity modulus and was taken from the Matpro handbook [53] and also recommended in the extension of Frapcon to (Th,U)O_2 [10]. The units are the same as in Equation 3.3, except for T, which is in Kelvin. The values of the elastic modulus reported at room temperature for UO_2 are typically between 223 [3] and 233 [52]. Marlowe and Kaznoff [5] also stated that the Young's modulus in UO_2 is 12% lower than the elastic modulus of ThO_2 [5] and corresponds to 233 GPa proposed by Hoch [52].

$$E_{UO_2} = 233.4(1-2.75P)(1.003-1.0915\times10^{-4}T) \tag{3.5}$$

No correlation for PuO_2 was found in the literature. Therefore, an extrapolation from MOX fuels in the Matpro library data [53] was applied to obtain the correlation for pure PuO_2 (Equation 3.6) as suggested in the OMICO report [10].

$$E_{PuO_2} = 233.4\times1.15(1-2.75P)(1.003-1.0915\times10^{-4}T) \tag{3.6}$$

Figure 7 compares the values of the three correlations finally chosen for the first TRANSURANUS thorium version. PuO_2 presents the highest value, since its correlation resulted from the multiplication of a factor that increased the expression of UO_2. This needs to be verified in the future with experiments. A comparison between the correlations of these oxides in Equations 3.3, 3.5 and 3.6 shows that ThO_2 is less sensitivity to porosity than UO_2 and PuO_2. This was also observed by Marlowe and Kaznoff and reported by Hart [5]. On the other side, ThO_2 and UO_2 present the same behaviour against the temperature as their slopes are identical (see Figure 7).

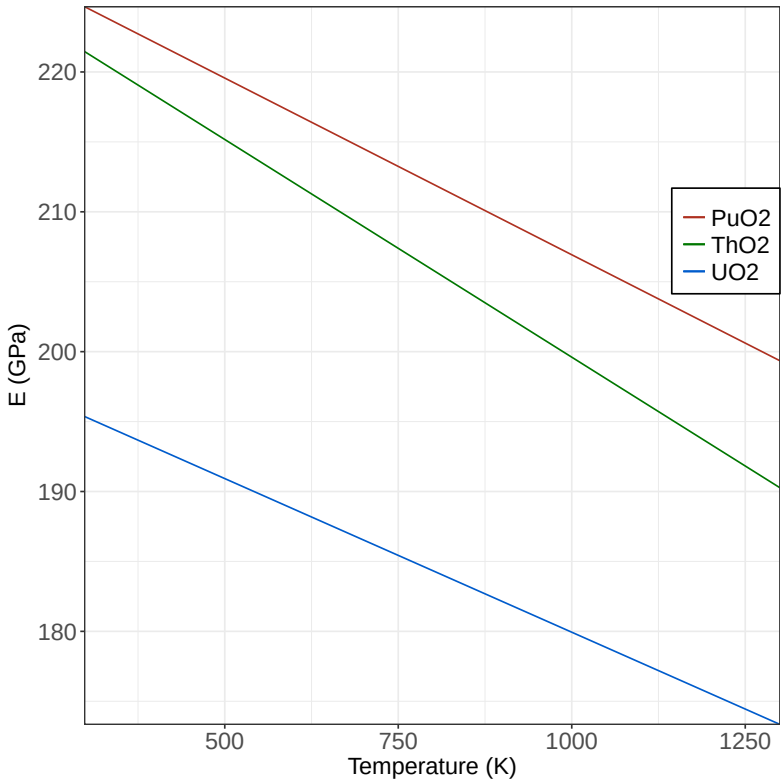

Figure 7 Comparison of the correlations of elasticity modulus

3.2. Poisson's ratio

For isotropic materials or for randomly oriented cubic polycrystalline materials that behave isotropically on a macroscopic scale and in absence of creep, plastic deformations and temperature changes [3], the Poisson's ratio is defined as [8, 54]:

$$\mu = \frac{E}{2G} - 1 \tag{3.7}$$

where μ has no units and E and G are the elastic and shear modulus respectively both expressed in MPa. The Poisson's ratio is temperature independent because both modulus have the same dependence on the temperature [51]. A linear interpolation was applied between ThO_2, UO_2 and PuO_2 in TRANSURANUS in order to get the correlation for the ceramic compounds. In Table 3 the values of Poisson's ratio for the three ceramic oxides with their respective references are listed:

	μ	Reference
ThO_2	0.28	[55, 10, 56, 8]
UO_2	0.32	[3, 55, 10, 18]
PuO_2	0.28	[55, 10]

Table 3 Poisson's ratio for ThO_2, UO_2 and PuO_2

3.3. Strain due to swelling

The estimation of the dimensional changes of a nuclear fuel during irradiation is of the utmost importance in order to prevent any type of failure in the rod. The substitution of lattice atoms by fission products either gas or solid atoms undergoes the fuel swelling [3].

In the OMICO project [10] and in the German-Brazilian project at Jülich Kernforschungsanlage [57] the value given by S.A. Rabin (see Equation 3.8) was proposed for (Th,U)O_2 fuels that accounts for the swelling due to solid products and fission gases. This expression was also adopted a first instance for (Th,Pu)O_2 cases.

$$\frac{\Delta V}{V} = \frac{1.25\%}{10MWd/kg(U+Th)} \tag{3.8}$$

The term $\frac{\Delta V}{V}$ is the total procent increment of volume due to the solid and gas fission products. According to Spino [58] the swelling due to solid fission products is between 0.15 and 0.45% per 10 GWd/tHM for UO_2 fuels and the swelling due to fission gases is approximately 0.56% per 10 GWd/tHM. Olander provided an intermediate value between the limits given by Spino of 0.32% per 10 GWd/tHM for UO_2 [3]. The sum of both contributions results in a total strain due to swelling for UO_2 fuels between 0.7 and 1%, lower than the value proposed in the OMICO project for (Th,Pu)O_2. Nevertheless, a sensitivity analysis for this property was carried out as part of the validation of the full TRANSURANUS version for (Th,Pu)O_2 fuels with gap size examinations in Chapter 7.

Loewen [56] proposed for (Th,U)O_2 version in FRAPCON a value of 0.8545% per 10 GWd/tHM that accounts for the two mechanisms of strain. This value was adopted for (Th,U)O_2 compounds in TRANSURANUS because it lies within the experimental range published by Spino for ceramic compounds.

3.4. Thermal strain

The temperature profile in the fuel yields among other effects an expansion of the volume of the pellet. This expansion may produce the interaction of the pellet-cladding whose imme-

diate consequences are the critical increment of the fuel temperature until the melting point due to the lose of convection in the gap and the cladding failure. The thermal expansion coefficient is approximated by the linear thermal expansion coefficient by:

$$\alpha_v = \frac{1}{V}\left(\frac{\partial V}{\partial T}\right)_P = \frac{1}{\Delta T}\frac{\Delta T}{V_0} \cong \frac{3}{\Delta T}\left(\frac{\Delta L}{L_0}\right) \tag{3.9}$$

where α_v is the thermal expansion coefficient, ΔV and ΔL are the volume and length increment. V_0 and L_0 are the initial volume and length respectively.

The expression of the linear thermal expansion (in %) selected for (Th,U)O_2 is represented in Equation 3.10 for temperatures below 923 K and Equation 3.11 when the temperate takes a value between the range 923 K $\leq$ T $\leq$ 2000 K. This expression was derived from the measurements done in more than 30 samples by Touloukian [59] and is recommended by various authors [33, 50, 60]. Nevertheless other authors [8, 10, 56] suggested the two order polynomial correlation given by Hoch [52] for ThO_2, because the later can be applied up to 2273 K, extending the temperature range of validity.

$$\begin{aligned}\left(\frac{\Delta L}{L}\right)_{(Th,U)O_2} &= -0.179 - (1 - y_{ThO_2})0.0149 \\ &+(5.097 \times 10^{-4} + (1 - y_{ThO_2})4.705 \times 10^{-4})T(K) \\ &+(3.732 \times 10^{-7} - (1 - y_{ThO_2})4.002 \times 10^{-7})T(K)^2 \\ &-(7.594 \times 10^{-11} - (1 - y_{ThO_2})11.98 \times 10^{-11})T(K)^3\end{aligned} \tag{3.10}$$

$$\begin{aligned}\left(\frac{\Delta L}{L}\right)_{(Th,U)O_2} &= -0.179 - (1 - y_{ThO_2})0.0149 \\ &+(5.097 \times 10^{-4} + (1 - y_{ThO_2})6.693 \times 10^{-4})T(K) \\ &-(7.594 \times 10^{-11} - (1 - y_{ThO_2})19.784 \times 10^{-11})T(K)^3\end{aligned} \tag{3.11}$$

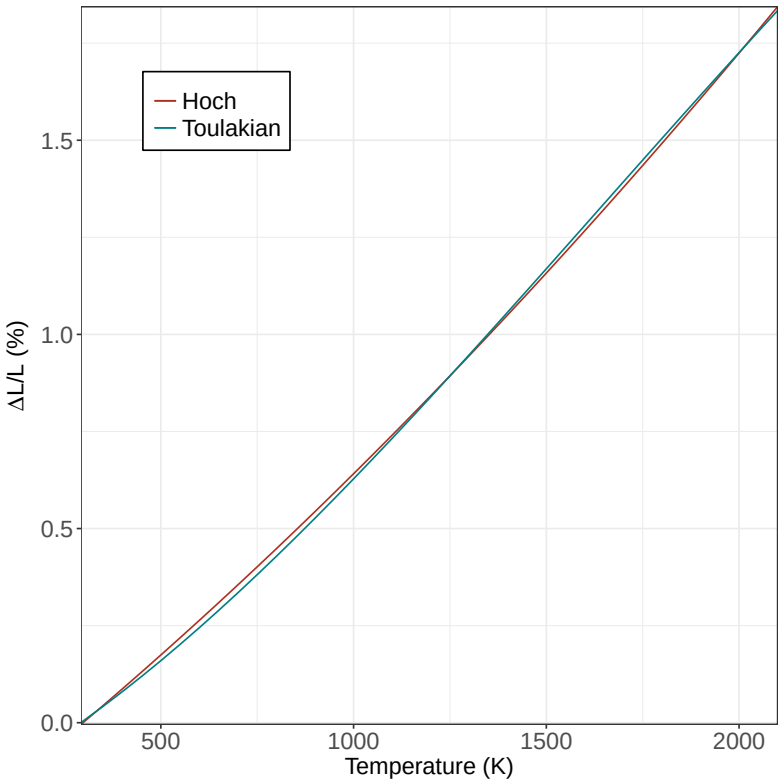

Figure 8 Comparison of the two linear themal expansion of ThO_2

On the other side, for ThO_2-PuO_2 mixed oxides the expression reported by Hoch [52] (Equation 3.12) was applied for the pure ThO_2. As was previously mentioned this expression can be applied up to 2273 K higher than the expression derived by Touloukian as pointed out by [8, 10, 56]. The reason of using a different expression for this fuel is that in the OMICO report [10], this correlaltion for (Th,Pu)O_2 fuels is explicitly recommended for FRAPCON whereas Bakker [50] suggested the employment of Touloukian's expression for the case of (Th,U)O_2 fuels. Figure 8 shows the similarity of both correlations, hence the utilization of one or other at any range of temperatures would not have any impact in the results of the simulations with thorium.

$$\left(\frac{\Delta L}{L}\right)_{ThO_2} = -0.2426 + 7.837 \times 10^{-4} T(K) + 9.995 \times 10^{-8} T(K)^2 \tag{3.12}$$

For pure PuO_2 oxides the value recommended in the OMICO project [10] from the material property nuclear database Matpro [53] (see Equation 3.13) was finally selected against the value fitted in the IAEA (International Atomic Energy Agency) Technical Report [60]. This expression published by the IAEA is indeed fitted from the correlation from the Matpro handbook. As can be seen in Figure 9, the adjust was not performed correctly, since both expressions are different. Therefore, the correlation from the Matpro handbook was finally selected

for PuO_2.

$$\left(\frac{\Delta L}{L}\right)_{PuO_2} = [-3.9735\times10^{-4}+8.4955\times10^{-6}T_c+2.1518\times10^{-9}T_c^2+3.7143\times10^{-13}T_c^3]\times100 \tag{3.13}$$

T_c being the temperature expressed in Celsius.

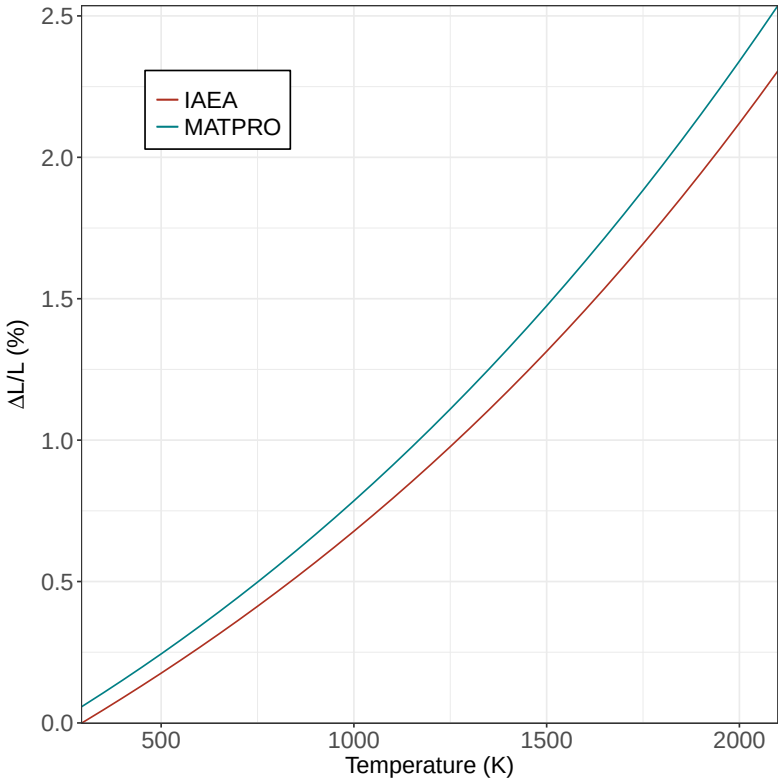

Figure 9 Comparison of the two linear themal expansion of PuO_2

Figure 10 compares the linear thermal expansion of the three oxides. At temperatures below 1000 K, the values of PuO_2 and UO_2 are practically identical, but above this temperature the value of PuO_2 increases more than UO_2. The lower value of ThO_2 presented in the Figure 10 draws the conclusion of a lower thermal expansion of this ceramic compound. This is an advantage to avoid further strains in the pellet that may undergo interaction with the cladding.

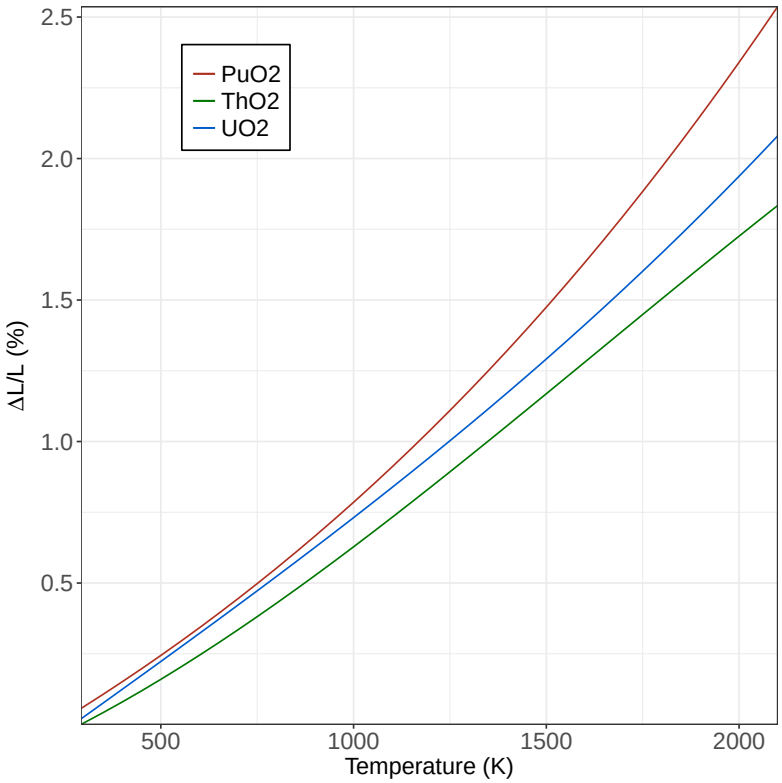

Figure 10 Comparison of the linear thermal expansion of ThO_2, UO_2 and PuO_2

3.5. Thermal conductivity

The transmission of heat within an ionic solid can be regarded as the solid behaves as an ideal gas in which the particles are phonons and therefore the kinetic theory of ideal gases can be applied. Phonons can be described as photons travelling within a solid. Therefore, the conduction of the heat depends on how the phonons behave in the bulk which is accounted by the macroscopic quantity, thermal conductivity [3]. The expression derived from the kinetic theory for the thermal conductivity for ionic solid is expressed below (see Figure 3.14).

$$\lambda = \frac{1}{A + BT} \tag{3.14}$$

In Equation 3.14 the term A represents the interaction of the phonons with the material, for example impurities or lattice atoms whereas the term B is the interaction phonon-phonon (Umklapp process) and T stands for the temperature in Kelvin. For UO_2 fuels, the correlation implemented in TRANSURANUS accounts in the terms A and B for the different phenomena (i.e. impurities growth or changes in the stoichiometry) that happens to the fuel during irradiation. In contrast, for ThO_2 fuels the Lucuta's model [61] was applied. This model degrades the thermal conductivity by means of factors that represent those phenomena. Equation 3.15

represents the Lucuta's factorized thermal conductivity.

$$k_{(Th,U/Pu)O_2} = k_p \times k_{dfp} \times k_{pfp} \times k_0 \tag{3.15}$$

$k_{(Th,U/Pu)O_2}$ is the thermal conductivity of a thorium-based system whose units are expressed in $Wm^{-1}K^{-1}$. k_p is a factor that takes into account the degradation of the thermal conductivity due to the porosity, whereas k_{dfp} and k_{pfp} degrade the thermal conductivity because of the dissolved and precipitated fission products respectively. The expression of these three factor are represented in Equation 3.16. k_0 is the thermal conductivity of a fresh fuel whose form is represented in Equation 3.14 where the term A is a function of the complementary oxide typically UO_2 or PuO_2 while B should be constant.

$$\begin{aligned} k_p &= 1 - \sigma P; \sigma = 2.6 - 0.5\frac{T}{1000} \\ k_{dfp} &= \left(\frac{1.09}{\beta^{3.265}} + \frac{0.0643}{\sqrt{\beta}}\sqrt{T}\right) arctan\left(\frac{1}{\frac{1.09}{\beta^{3.265}} + \frac{0.0643}{\sqrt{\beta}}\sqrt{T}}\right) \\ k_{pfp} &= 1 + \frac{0.019\beta}{3 - 0.019\beta}\frac{1}{1 + e^{-\frac{T-1200}{100}}} \end{aligned} \tag{3.16}$$

P is the porosity in units, β means the burn-up in at.% and T is the temperature in Kelvin.

	$(Th,Pu)O_2$	$(Th,U)O_2$
A (mKW^{-1})	6.071 $\times$ 10^{-3} + 5.72 $\times$ 10^{-1}[PuO_2] - 5.937 $\times$ 10^{-1}[PuO_2]^2	4.195$\times$ 10^{-4} +1.112 [UO_2] -4.499$\times$ [UO_2]^2
B (mW^{-1})	2.4 $\times$ 10^{-4}	2.248$\times$ 10^{-4} +9.17 $\times$ 10^{-4} [UO_2] -4.164 $\times$ 10^{-3} [UO_2]^2
Reference	[62]	[50, 63]

Table 4 A and B functions chosen for $(Th,Pu)O_2$ and $(Th,U)O_2$ fuels in TRANSURANUS

Table 4 gathers the correlations of the terms A and B in Equation 3.14 chosen for the thermal conductivity in TRANSURANUS. For $(Th,Pu)O_2$ fuels the expressions fitted from experimental data done by Cozzo were selected [62]. The values published by Basak [64] and Rodriguez [65] also coincided to the thermal conductivity derived by Cozzo for the given temperatures and PuO_2 concentrations. As was previously commented, the term B stands for the phonon-phonon scattering mechanism and therefore this term must be independent of the Pu-U concentration as Cozzo inferred for $(Th,Pu)O_2$ cases [62]. As can be appreciated in Figure 12 that compares the term B from different authors, the correlation reported by IAEA is the only one that reflects the non-dependency of therm B according to Cozzo. However, looking at Figure 11 where the term A is displayed along different concentrations of U/PuO_2, the value provided by IAEA is again a constant, neglecting the concentration of the complementary actinides. Consequently, this correlation was disregarded. The correlations of both

terms derived by Murabayashi [63] and reported by Bakker [50] and Hania [33] were the final choice. Although the term B slightly varies with the concentration of UO_2, its expression fits with the experimental data points obtained by Kutty [49]. Most recent review done by the IAEA [60] suggests the application of the expressions gathered by Belle et al. [8]. The reason that this recommendation was turned down was that the term A weakly depends on the UO_2 content. The expression derived by Konings et al. [66] was also neglected because the correlation did not have the corresponding shape of Equation 3.14 according to Olander [3]. Previous measurements done by Springer and reported by Hart [5] for (Th,U)O_2 were disregarded due to lack of consistency in the results. In this report, measurements of thermal conductivity from irradiated (Th,U)O_2 samples through the flash laser technique were carried out by Matolich and Storhok (1970). The results reported contradicted the theory, since the thermal conductivity of the irradiated samples was larger than the fresh samples of (Th,U)O_2. They attributed this anomaly to the high irradiation temperature, that annealed the lattice damage. To conclude, the formulation derived in this report omits the therm A in Equation 3.14.

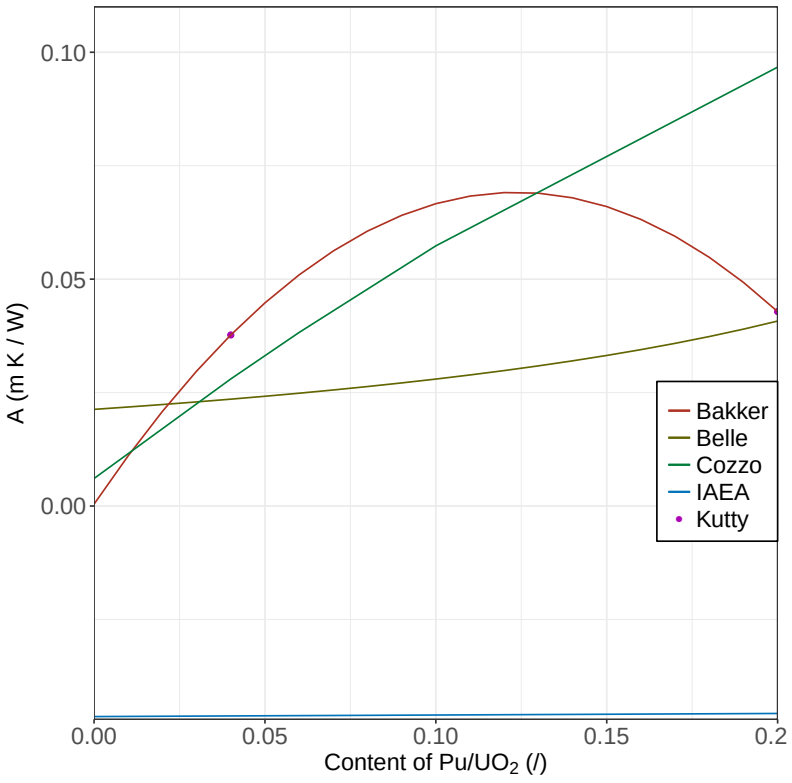

Figure 11 Comparison of parameter A as function of Pu/UO_2 concentration

Figure 13 compares the three thermal conductivities of the pure oxides used in TRANSURANUS along the temperature. The curve of PuO_2 was extrapolated from Cozzo's correlation due to the lack of experimental data for this solid. It can also be observed that the thermal conductivity of ThO_2 is larger than of UO_2 below 1100 K but then the thermal conductivity of UO_2 becomes larger.

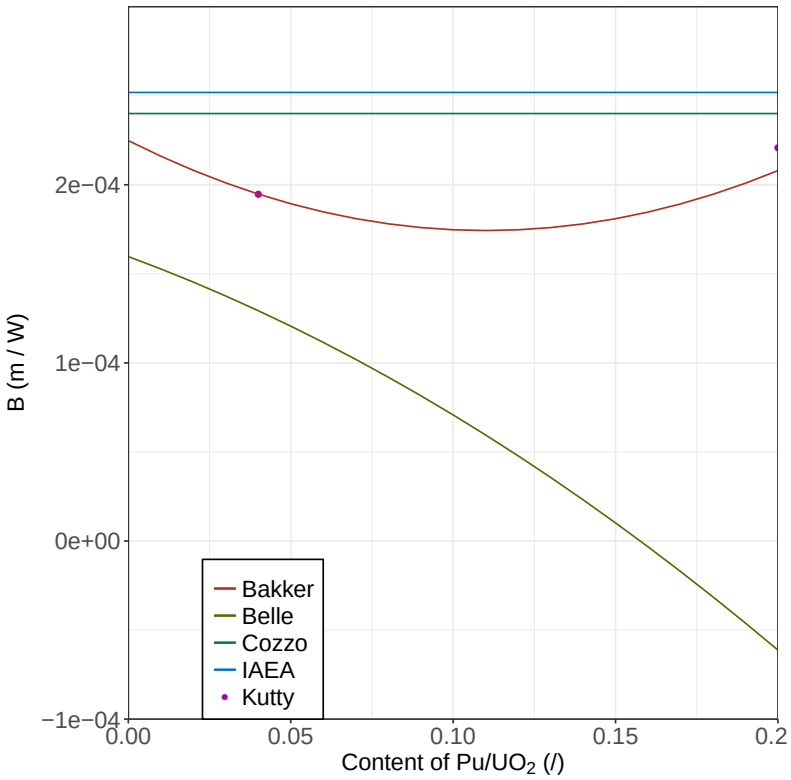

Figure 12 Comparison of parameter B as function of Pu/UO_2 concentration

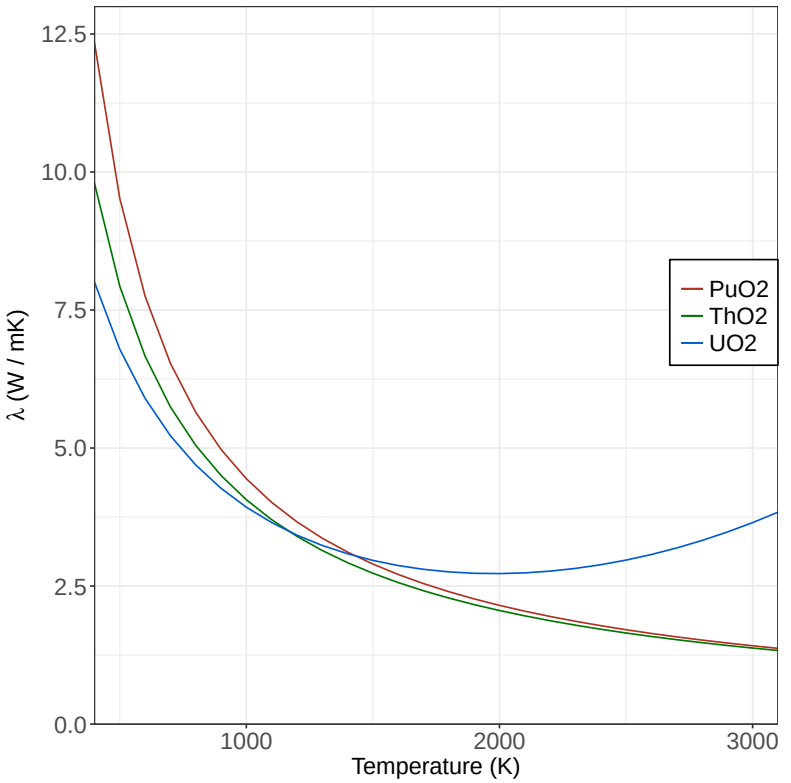

Figure 13 Comparison of the thermal conductivity between the threes oxides, ThO_2, PuO_2 and UO_2

The thermal conductivity of UO_2 reaches a minimum at temperatures around 2000 K, then the curve increases again. This increment in the thermal conductivity is attributed to the contribution of free electrons to the heat transfer. The expression of the thermal conductivity that accounts for both the phonon and electron transmission is represented in Equation 3.17 for UO_2 fuels.

$$\lambda = \frac{1}{A + BT} + \frac{C}{T^2} exp\left(\frac{-D}{T}\right) \tag{3.17}$$

On the other side, the strict +4 electron valence in Th neglects the contribution of free electron on the thermal conductivity in comparison to U whose oxidation states are +4, +5 and +6 due to the presence of electrons in the orbital 5f [62, 8]. However, the temperature range in Cozzo's experiment was between 500 and 1600 K [62], slightly lower than the temperatures from which the electrons may contribute to the heat conduction in UO_2 fuels. An extension of the range of temperatures from 1600 K is highly recommended for further experiments in order to verify that the electron term in Equation 3.17 is negligible for ThO_2.

3.6. Creep rate

According to Olander [3] creep is defined as a slow-motion plastic deformation. All the experiments have demonstrated that the plastic deformation of UO_2 polycrystalline lattice happens along the slip planes $\{110\}$ and $\{100\}$. When a shear stress is applied, sheets of uranium atoms are displaced around the dislocation contained in the glide plane. Due to the large variety of mobile defects such as dislocations or vacancies, dozens of mechanisms have been proposed [3]. Among all of these mechanisms only two are the most acceptable, the stress-induced vacancy migration and the climb controlled dislocation that yield a deformation of the grains in the solid [3].

The intra-granular diffusional vacancy theory develop by Nabarro-Herring is the most representative theory that explains this creep mechanism. It differs from grain boundary diffusional vacancy theory proposed by Coble in the way that vacancies flow from the poles, where tensile stresses are applied in a sphere-shape grain to the equator, where the tensile stresses are null. Nabarro-Herring theory states that the vacancy motions occur in the interior of the grain, whereas Coble claimed that the movement of vacancies takes places along the grain boundary. This difference has repercussion in the Arrenius-shape Nabarro-Herring creep rate expression (Equation 3.18) in two ways. Coble's formula, in contrast, inversely depends on the cube of the grain radius not on the square, as Habarro-Herring derived. Secondly, in the exponential term the activation energy for Coble's formulation is the grain-boundary diffusion activation energy, while in Equation 3.18 E_{vol} is the volumetric activation energy as the diffusion of vacancies happens within the grain. Generally, the volumetric activation energy tends to be larger than the grain boundary activation energy. On the opposite side, Coble's theory

keeps the same linearity for the applied stress [3].

$$\dot{\epsilon} = \frac{B\sigma}{d^2} exp\left(\frac{E_{vol}}{kT}\right) \tag{3.18}$$

$\dot{\epsilon}$ is the creep rate in h^{-1}, d is the grain diameter in μm, E_{vol} is the volumetric activation energy of vacancy diffusion as was previously described, k is the Boltzmann's constant that takes the value of 1.38064852 $\times$ 10^{-23} m^2 kg s^{-2} K^{-1}, T is the temperature and σ is the stress in psi. B is a constant that embeds among other parameters the volume diffusion coefficients of vacancies [3] by accounting for the vacancy jump frequency.

Nonetheless, at low temperatures and high stresses, another mechanism, climb dislocation, is found to govern creep rate. Weertman [67] has proposed two closely related models to describe the creep due to dislocation climb. In the first model a dislocation that is subjected to a shear stress climbs around a pinned dislocation that is immobile. The formulation of this model shows that the creep rate linearly depends on the cube of the stress, and its activation energy is the dislocation volume diffusion. The second mechanism proposed by Weertman assumes that the creep rate is generated by the mutual annihilation of pairs of dislocations. The difference between this later mechanism and the first one is that the exponent of the stress of this mechanism is 4.5, instead of 3, as can be appreciated in Equation 3.19.

$$\dot{\epsilon} = B'\sigma^{4.5} exp\left(\frac{E'_{vol}}{kT}\right) \tag{3.19}$$

E'_{vol} stands for the volumetric activation energy for dislocation annihilation and the other parameters have the same meaning as previously described. The strong dependence of the creep rate to the stress powered to 4.5 is in very good agreement with many experiments in different materials [3].

The irradiation of nuclear fuels produces within the grain either vacancies, when a lattice atom is fissioned, or dislocations caused by the displacement of lattice atoms by means of the elastic collision with high energy fission fragments. The increase of the concentration of these defects due to irradiation increases the value of the pre-exponential term and, therefore, enhances the creep rate.

The most complete formulation of creep rate was proposed by Solomon et al. [68, 69, 70] and was used in the fuel performance code LIFE-I to simulate the Experiment Breeder Reactor II (EBR-II) conditions for UO_2 fuels.

$$\dot{\epsilon} = A(\dot{F})\sigma^{4.5} exp\left(\frac{-Q}{RT}\right) + \frac{A_1(\dot{F})\sigma}{d^2} exp\left(\frac{-Q_1}{RT}\right) + C\sigma\dot{F} \tag{3.20}$$

Where $\dot{F}$ is the fission rate in fissions/s cm^3, Q and Q_1 represent the activation energy for dislocation and vacancies respectively and are equal to 132 kcal/mol and 90 kcal/mol. The

larger value of the dislocations compared to that of vacancies activation energy measured agrees well with the theory derived by Olander [3]. R is the well-known universal gas constant and the other parameters are described above. The fission rate-dependency in the pre-exponential terms have the following form:

$$A(\dot{F}) = \frac{1.38 \times 10^{-4} + 4.6 \times 10^{-17}\dot{F}}{-90.5 + D}$$
$$A_1(\dot{F}) = \frac{9.73 \times 10^{6} + 3.24 \times 10^{-6}\dot{F}}{-87.7 + D} \tag{3.21}$$

where D is the theoretical density expressed in %, with the limitation that both functions are only valid for theoretical densities above 92 %.

In Equation 3.20 the two mechanism of creep, with the fission-enhanced creep terms added can be easily distinguished. There is an extra term that considers the fission-induced creep directly, which is temperature independent as observed at low temperatures [68, 3]. The value of C in Equation 3.20 is 4.827$\times 10^{-31}$.

Even for UO_2 the data published are very limited. Solomon's formulation was thus adopted for thorium-based fuels as first approximation. For ThO_2-UO_2 systems, Equation 3.20 was implemented entirely in TRANSURANUS. Measurements carried out by Poteat [71] in samples of pure ThO_2 with small amount of impurities between 1400 and 1800°C and an applied stress range from 4000 to 11000 psi drew the conclusion that the activation energy for creep by vacancy self-diffusion, Q_1 has the value of 112 kcal/mol, with a range of uncertainty of $\pm$ 7 kcal/mol in the same order of the value proposed by Solomon. This value was not taken into account because the original Solomon's formulation was kept. Belle et al. [8] reported experimental results which showed that the activation energies (96.65 and 173 kcal/mol respectively) were slightly higher to the values exposed by Solomon. However, the stresses were powered to 1.47 and 4.36 respectively, which are different from the theory and Solomon's observations. The experiments mentioned in Belle's book were performed on samples with an initial grain size between 120 - 220 μm [8] larger as normal grain size for nuclear fuels in reactors. Therefore, Belle's formulations were also rejected.

For ThO_2-PuO_2 fuels, as first step the MOX correlation proposed in the Matpro handbook was considered [53]. This formulation was also obtained from experiments and gathered by Evans [72]. Nevertheless, this correlation mainly differs in the exponential term which is modified by the inclusion of the porosity and the content of plutonium. Neither Solomon [68] nor Olander [3] declared the dependence of the thermal term upon the porosity and plutonium content. Moreover, Belle [8] claimed that the inclusion of UO_2 in a ThO_2 polycrystalline structure has an influence only in the pre-exponential term. Consequently, Matpro formulation was totally disregarded. The application of Vegard's law was required to implement the correlation for (Th,Pu)O_2 fuels in TRANSURANUS.

For the thorium dioxide, Equation 3.20 was adopted from UO_2. For PuO_2 the MOX correla-

tion suggested in the FEMAXI handbook [18] derived from the SKI (Swedish Nuclear Power Inspectorate) report [73] was adopted as a first approximation:

$$\dot{\epsilon}_{PuO_2} = \frac{2.63 \times 10^5 + 8.93 \times 10^{-13}\dot{F}}{-87.7 + \rho} \frac{\sigma}{d^2} exp\left(\frac{-Q}{RT}\right) + C\sigma\dot{F} \tag{3.22}$$

where $\dot{\epsilon}_{PuO_2}$ is the creep rate in s^{-1}, $\dot{F}$ is the fission rate in fissions/m^3s, σ is the stress in MPa and the rest of parameters are explained before with identical units. The pre-exponential constants differs because the units are different, but a simple conversion shows that they are the same. From Equation 3.22 it can be appreciated that the climb-dislocation mechanism was not accounted for PuO_2.

3.7. Yield stress

In plasticity, the yield stress is the stress at which the elastic deformation (Hook's law) ends and the permanent deformation (plasticity) starts (see Figure 5). The primary tensile studies on irradiated thorium pellets were carried out by Bement in 1961 [74]. In this work, ThO_2 specimens doped with C, N, H, Fe, Ca, Al, Be and Si were irradiated at MTR from 0.1% to 2% at. burn-up and then some of them annealed at different temperatures. Finally, those specimens were subjected to tensile stress and the elongation-stress curves were obtained. The inclusion of C and the various techniques employed during fabrication process caused a different grain size in the samples [74]. From the stress-strain curves obtained from the experiments, the yield stress could be extracted and then a experimental fit that only depends on the burn-up was performed. A least square adjust was applied to these experimental data to derive the correlation which is represented in Equation 3.23. Figure 14 shows the experimental points from Bement [74] and the linear correlation inferred. As can be observed, there is a great scatter in the experimental data, and this might be attributed to the different initial grain size of the samples due to the various fabrication methods and the annealing treatments that differed in time and in the annealing temperature.

$$\sigma_{ThO_2} = (102.4815 \times \beta + 40.3346)10^{-3} \tag{3.23}$$

Here, σ_{ThO_2} is expressed in psi and β is the burn-up in at%

For pure UO_2, the correlation already implemented in TRANSURANUS was used:

$$\begin{aligned} \sigma_{UO_2} &= 13.6 + \frac{T_c}{4500}; T_c < 1733.824 \\ \sigma_{UO_2} &= 66 - 0.03 \times T_c; T_c \geq 1733.824 \end{aligned} \tag{3.24}$$

where σ_{UO_2} is yield stress of UO_2 expressed in kp/mm^2 and T_c is the temperature referred in Celsius. In case PuO_2 the value of ThO_2 was used as first approximation.

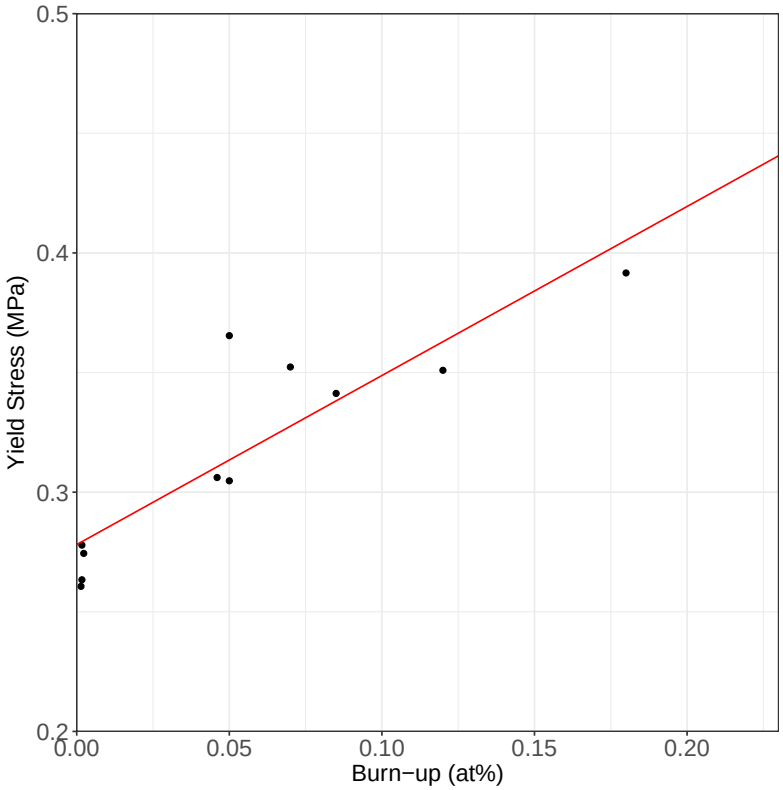

Figure 14 Yield stress of ThO_2

3.8. Rupture strain

The rupture strain is the strain at which the sample or the material breaks after being subjected to tensile tensions (see Figure 5). Figure 15 displays the correlation calculated by means of least square adjust from the experimental data points obtained by Bement [74] when he analysed the elastic-plastic behaviour of irradiated ThO_2 pellets. The inverse dependence of the rupture strain along the burn-up (see Equation 3.25) can be explained as the more burn-up to the sample is applied, the more damage is caused in it as vacancies and dislocations are the source of cracks formation that eventually yield the fracture of the sample. In this case, the experimental data show less scatter than in the yield stress derived from the same publication.

$$\epsilon_{ThO_2} = \frac{1}{2.7212 + 40.3346\beta} \tag{3.25}$$

ϵ_{ThO_2} stands for the rupture strain in % and β is the burn-up expressed in at%.

The correlation used in TRANSURANUS for UO_2 is the following:

$$\begin{aligned} \epsilon_{UO_2} &= 0; T_c < 1400 \\ \epsilon_{UO_2} &= 10^7; T_c \geq 1400 \end{aligned} \tag{3.26}$$

where T_c is the temperature in Celsius. As was done in the case of yield stress the correlation

inferred (Equation 3.25) from Bement [74] data points was used for PuO_2. Therefore, no necessity to introduce the Vergard's law for (Th,Pu)O_2.

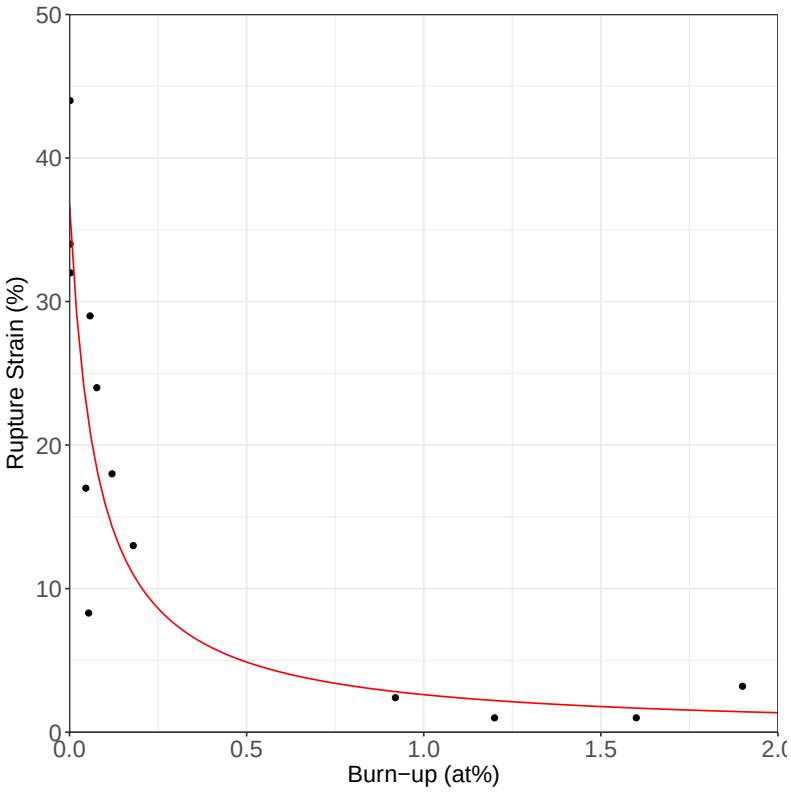

Figure 15 Rupture strain of ThO_2

3.9. Heat Capacity

The total heat capacity of a real solid is the sum of the heat capacities of all excited modes in the system [34]. These excited levels are lattice vibrations (phonons), electron contributions and point defect formation [34, 55]. The accepted formulation for the heat capacity for UO_2 based on these three contributions is the following [6, 34, 55]:

$$C_p = \frac{C_1 \theta^2 e^{\frac{\theta}{T}}}{T^2 \left(e^{\frac{\theta}{T}} - 1\right)^2} + 2C_2 T + \frac{C_3 E_a e^{-\frac{E_a}{T}}}{T^2} \tag{3.27}$$

where C_p is the heat capacity in J/mol K, C_1 C_2 and C_3 are constants, θ is the Debye temperature expressed as $\frac{\hbar w_D}{k}$, $\hbar = \frac{h}{2\pi}$ is the reduced Planck's contant, w_D is the Debye's frequency of the solid that only depends on volume [3] and k is the Boltzmann's constant. Finally E_a is the activation energy for defect formation.

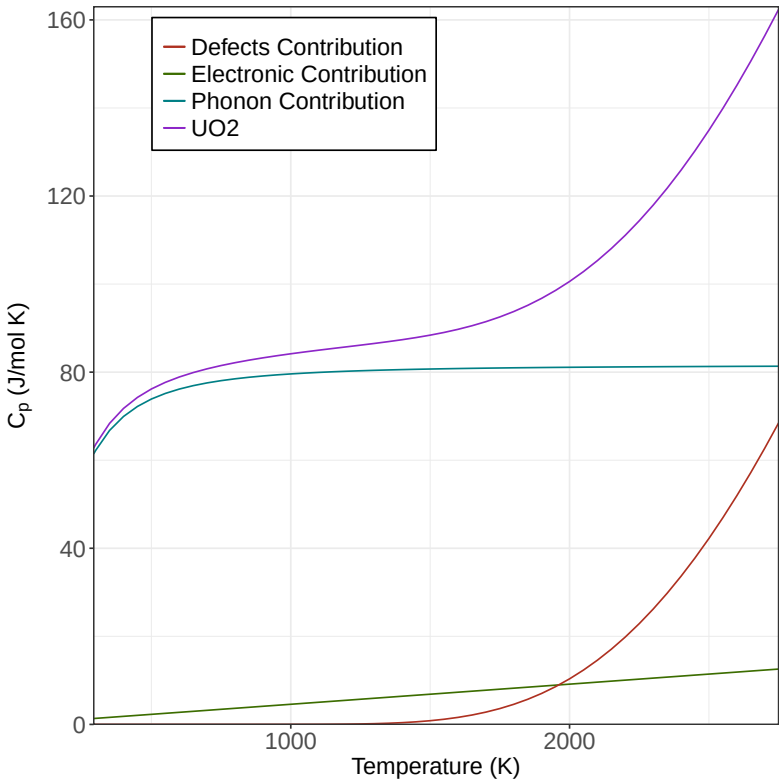

Figure 16 Heat capacity of UO_2 from [6]. The three contributions can clearly be appreciated

From Equation 3.27 and Figure 16 the three contributions can clearly be distinguished. The first contribution that has the characteristic form of a Debye's integral is the phonon contribution, whose range of validity is up to 1800 K [3, 6, 34, 55]. Debye's theory differred from Einstein's by the assumption that the atoms in a solid vibrate in unison and do not oscillate independently, as Einstein stated.

The electronic contribution ($\propto T$) was derived from the free electron Fermi Gas Model [34]. Its range of application is up to 2000 K [6]. Finally, the last term accounts for the increment of the heat capacity due to the formation of lattice defects [6]. The term is valid from 1500 K to 2670 K when the Frenkel defects are the most important. Above this temperature threshold, the Frenkel defects are saturated and Schottky point defects become more important. It is important to mention that, generally, authors do not agree in the temperature thresholds in which each contribution is valid.

Valu [25] carried out measurements of the enthalpy in samples of $(Th_{1-y},Pu_y)O_2$ solid solutions with y=0.03, 0.08, 0.3, 0.54 and 0.85, which were performed in a range of temperatures between 476 K and 1790 K. Once the correlations of the enthalpy were inferred from the experimental results, the heat capacity expressions were obtained from the derivation of the enthalpy according to the thermodynamic (see Equation 3.28). He also stated the fulfillment

of the Neumann-Klopp rule for intermediate compounds.

$$C_p = \left(\frac{\partial H}{\partial T}\right)_P \tag{3.28}$$

The correlation resulting from Equation 3.28 follows the second order Maier–Kelly type polynomial equation as can be seen in Equation 3.29.

$$C_p = A + B \times T + \frac{C}{T^2} \tag{3.29}$$

Where T is the temperature in Kelvin and A, B and C are parameters to fit. This polynomial is the simplification of Equation 3.27 by means of a Taylor's expansion in the exponential terms for high temperatures. This simplified expression was obtained by Belle [8] for pure ThO_2 for temperatures between 323 K and 3400 K [8] from the derivation of the empirical correlation of the enthalpy (see Equation 3.28). Nonetheless, correlations from more recent experiments also gathered by Belle neglected the third term $\frac{e^{-\frac{E_a}{T}}}{T^2}$, i.e. defect-formations from 3.27 despite the temperature (2950 K) at which they were performed [8]. Dash [75] also fitted his measurements in samples of ThO_2 through the methods of differential scanning and multi high temperature calorimeter with already published data to second order polynomial. However, this polynomial was extended to a third order for the samples $(Th_{1-y},U_y)O_2$ when y took the values of 0.0196, 0.0392, 0.0588, 0.098 and 0.1964 in order to account the effect of point defects creation at temperatures above 1500 K.

Van Uffelen [10] and Loewen [56] suggested the utilization the expression of the heat capacity published by Belle represented in Equation 3.27, that omits the defect formation term.

Figure 17 compares all the correlations found in the literature for ThO_2. All the displayed correlations show similar behaviour. The correlation from Victor [76] was neglected because its temperature range of study is only valid at low temperatures (up to 1200 K). The correlation published by Dash [75] was not adopted because the parameter C in Equation 3.29 seems to be small because it reduces the influence of the term $\frac{1}{T^2}$ since the strong decrease at low temperatures is not accounted as happens to the other correlations. The value given by Hoch [52] and suggested in the IAEA report [60] looks like the most completed expression for ThO_2 and follows Equation 3.27. On the other side, the correlation given by Belle and suggested by Van Uffelen [10] and Loewen [56] omits the last term in Equation 3.27, consequently this option was disregarded. Valu's expression was chosen for ThO_2 since, it is fitted on more recent experimental data, in contrast to Hoch's [52] formula which indeed is more theoretical. The values of the parameters A, B and C from Valu's work are shorted in Table 5. It must be highlighted the two approaches to derive an accurate expression for the heat capacity from experimental results. In case that an enthalpy correlation is obtained from fitting measurements of the enthalpy on samples, the heat capacity is then derived from Equation 3.28. The expression of the heat capacity follows typically the second order Maier–Kelly type polynomial equation represented in Equation 3.29. On the other side, in other works the Debye's

temperature and other parameters are calculated and they are then introduced in Equation 3.27.

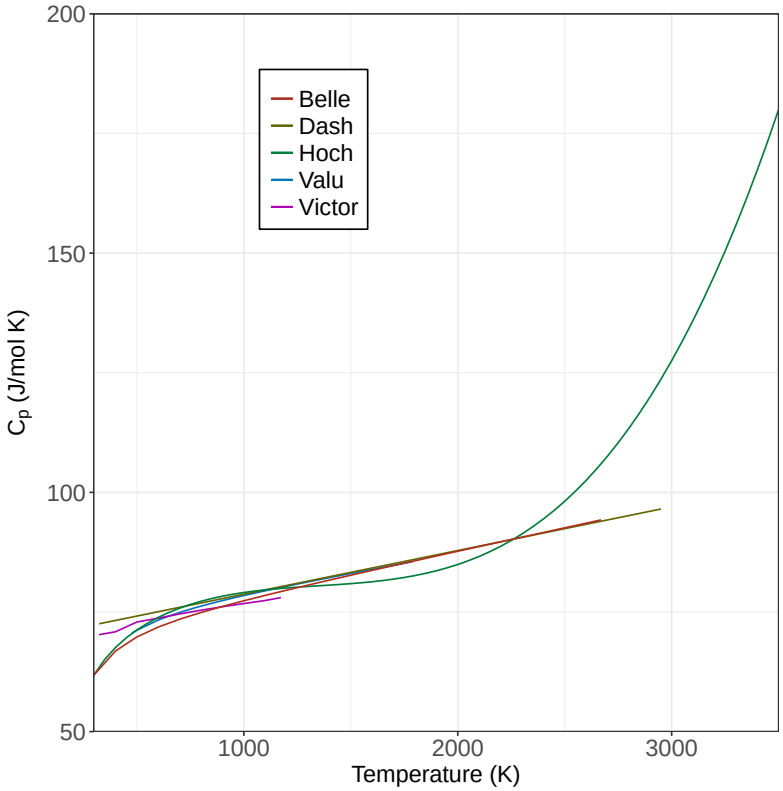

Figure 17 Comparison of the heat capacity values of ThO_2

	ThO_2	PuO_2
A (J K^{-1} mol^{-1})	71.492	81.948
B $\times$ 10^{-3} (J K^{-2} mol^{-1})	8.0241	11.956
C $\times$ 10^{4} (J K mol^{-1})	-107.7745	-171.2313

Table 5 Values of the parameters from Equation 3.29 according to Valu [25]

Figure 18 compares the two values found in the literature for PuO_2. Although the theoretical Matpro correlation was also suggested by Van Uffelen [10], the final choice was the fitted expression of the second order Maier–Kelly type polynomial equation (see Equation 3.29) from Valu in accordance to his work for the ThO_2-PuO_2 system. The values of the parameters A, B and C for PuO_2 are also listed in Table 5.

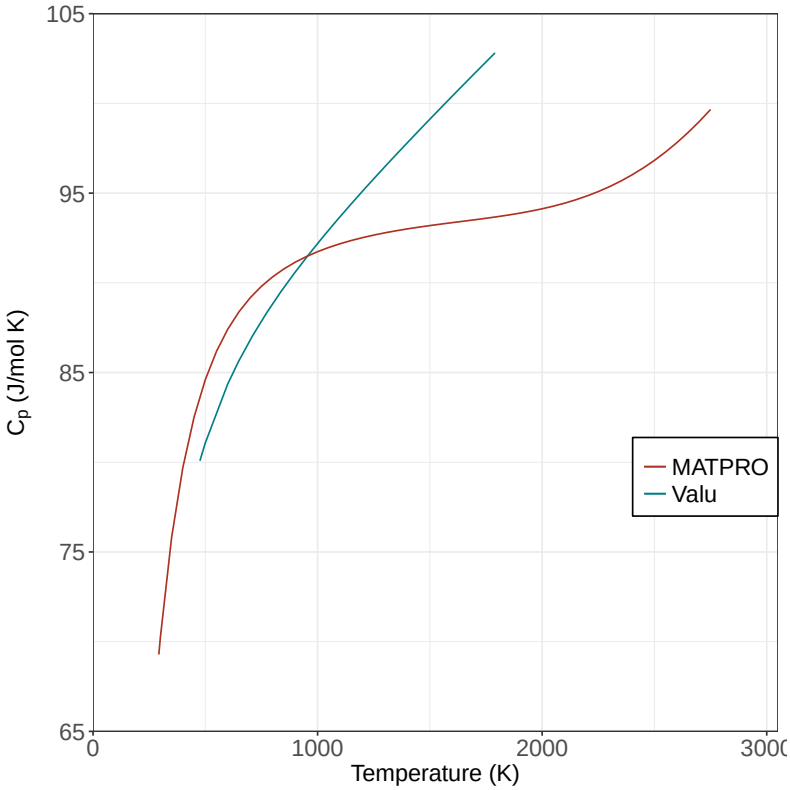

Figure 18 Comparison of the heat capacity values of PuO_2

The expression utilized for UO_2 is already implemented in TRANSURANUS:

$$C_{p,UO_2} = 12.54 + T(0.0170 + T(-0.117 \times 10^{-4} + T0.307 \times 10^{-8})) \tag{3.30}$$

where C_{p,UO_2} is expressed in cal / mol K and T is in Kelvin. This expression has the same shape of Equation 3.27, but its computation is easier in TRANSURANUS.

Figure 19 compares the values of the heat capacity along the temperature of the three ceramic compound implemented in TRANSURANUS. The simplification of the theoretical heat capacity (Equation 3.27) to a second order polynomial (Equation 3.29) is a good approximation up to temperatures of 1800 K, because at this range the slopes are practically parallel and lineal. Moreover, this correlation would not produce any problems in the computations due to exponential functions. Serizawa [77] attributed the lowest value of the specific capacity for ThO_2 to its electronic contribution since ThO_2 has no excitation level in the 5f electrons.

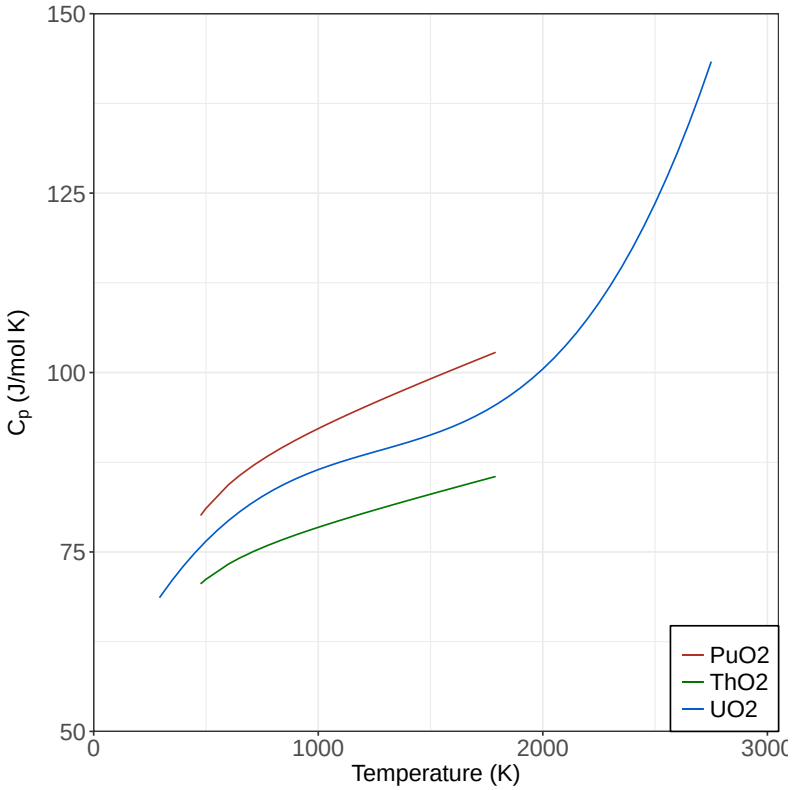

Figure 19 Comparison of the heat capacity correlation for ThO_2, UO_2 and PuO_2 in TRANSURANUS

In case that the temperature of the material crosses the melting point, the heat capacity correlations previously elected are no longer valid. The values of the heat at constant pressure for liquid state proposed for the three ceramic compounds are listed in Table 6:

	$C_{p,liq}$ (J /g K)	Reference
ThO_2	0.234	[60]
PuO_2	0.503	[60]
UO_2	$(0.931 + \frac{4.9215\times10^9}{T^2})1.10^{-3}$	[78]

Table 6 Heat capacity in liquid state for ThO_2, PuO_2 and UO_2

3.10. Density

In TRANSURANUS, the density is calculated by taking into account the current porosity and elongation of the fuel pellet [54, 79]. The density of a mixed oxide system is thus computed by means of linear interpolation of the densities at 25°C and of the concentration of the oxides. Table 7 lists the value of this densities of ThO_2, UO_2 and PuO_2 at normal conditions for the (Th,U)O_2 and (Th,Pu)O_2 mixed oxides.

	ρ^0 (g/cm^3)	Reference
ThO_2	10.00	[8]
UO_2	10.96	[80]
PuO_2	11.45	[10]

Table 7 Density of the pure oxides

3.11. Solidus-Liquidus melting temperature

The solidus-liquidus treatment in TRANSURANUS for thorium-based fuels has been simplified by not distinguishing the solidus-liquidus transition area, i.e. once the fuel reaches the temperature of fusion, the phase transformation from solid to liquid immediately takes place. The melting points for the three mixed ceramics are listed in Table 8. The melting point of a compound is directly related to the bonds of the atoms in its structure, i.e. with a higher atomic bond, a higher melting point. This atomic bond is affected by the electronic configuration of the atoms. For example U, an element that occupies 5f orbitals, will see its atomic bond weaker and therefore, its melting point will be reduced. Among all the actinide elements, Pu exhibits the lowest melting point because it has a $5f^4$ configuration with three degenerated levels [77, 34]. On the other side, the non-occupied 5f electrons in Th results in, that this element has only an oxidation state of +4, and consequently, its melting point would be higher.

	Melting point (K)	Reference
ThO_2	3640	[8]
PuO_2	2701	[78]
UO_2	3120	[78]

Table 8 Comparison of the melting points for ThO_2, PuO_2 and UO_2

Figure 20 compares the correlations found in the literature for the mixed oxide (Th,U)O_2. The two curves proposed by Belle [8] and FRAPCON [9] represent the threshold between the phases solidus-solidus+liquidus and solidus+liquidus-liquidus respectively.

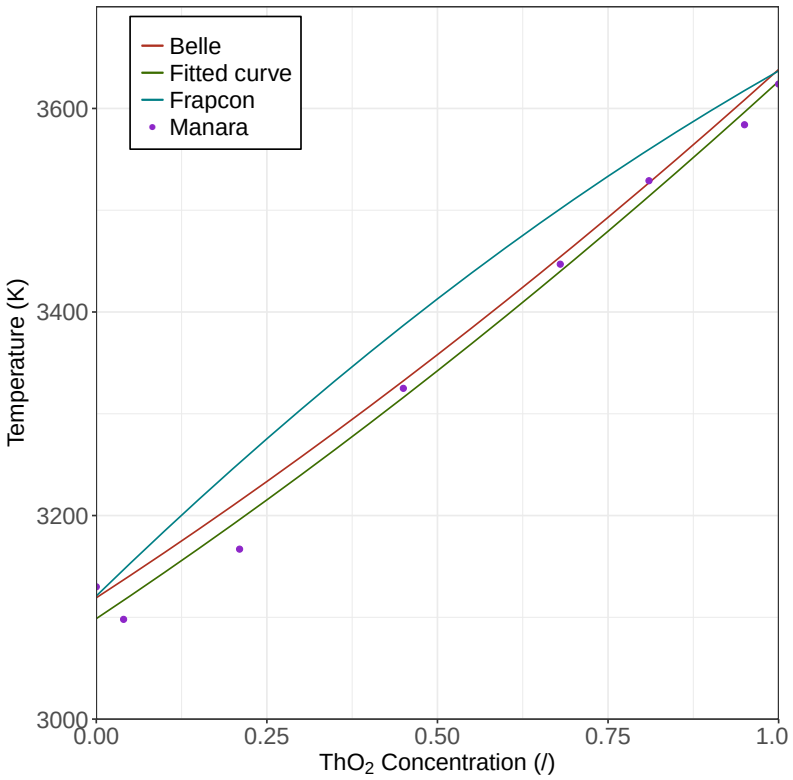

Figure 20 Comparison of the solidus-liquidus melting temperature between Manara [7], Belle [8] and Frapcon [9] for (Th,U)O_2 fuels

The correlation obtained (Equation 3.31) from Manara's experimental data was proposed to be implemented in TRANSURANUS because the data from which was derived are the most recent among all the measurements and the curve represents the threshold solidus-solidus+liquidus curve, having, thus, an extra safety barrier for future simulations regarding fuel pellet failure due to melting.

$$T = 81.754[ThO_2]^2 + 446.21[ThO_2] + 3098.7 \tag{3.31}$$

Figure 21 compares the melting temperature of (Th,Pu)O_2 as a function of PuO_2 concentration found in the literature. The linear interpolation proposed by Van Uffelen [10] in the OMICO report between the melting points of the two mixed oxides is a rough approximation. However, in the experimental work performed by Manara for (Th,Pu)O_2 systems the value of the melting point of PuO_2 is lower than the value accepted by several authors [78, 34]. A least square adjustment was performed to obtain a two order polynomial (see Equation 3.32) that depends on the PuO_2 concentration from Manara's work and, then, it was proposed for the implementation in TRANSURANUS.

$$T = 664.03[PuO_2]^2 - 1192.2[PuO_2] + 3554.1 \tag{3.32}$$

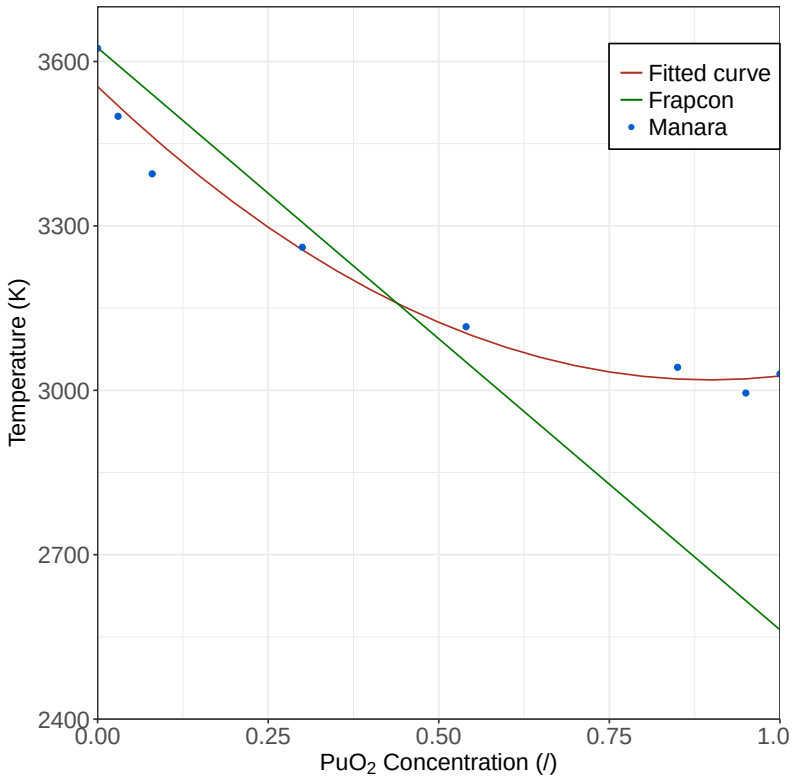

Figure 21 Comparison of the solidus-liquidus melting temperature of Van Uffelen [10] and Manara

3.12. Heat of melting

The enthalpy of melting or fusion is defined as the heat needed to apply to a certain material in order for it to change from solid to liquid state. The values of heat of melting for the three pure ceramic oxides are listed in Table 9. Liner interpolations using ThO_2 concentration as interpolator for (Th,U)O_2 and PuO_2 content for (Th,Pu)O_2 were applied.

	Heat of melting (J/g)	Reference
ThO_2	380.4364	[8, 33]
UO_2	259.3	[6, 33]
PuO_2	245.4	[78, 33]

Table 9 Heat of melting values of ThO_2, UO_2 and PuO_2

3.13. Emissivity

The heat exchange between two bodies without contact and no fluid among them is driven by radiation transmission characterized by the Stefan-Boltzmann's law. In this law the net heat exchanged is proportional to the difference of the temperatures of both bodies to the fourth power times a constant called emissivity, whose value is lower than 1 when they are not black bodies, i.e. they do not absorb all the radiation they receive. The heat exchange due to radiation is the leading mechanism only at high temperatures because of this fourth power.

Loewen [56] claims that there is a difference of 3.85 % between the emissivity of UO_2 and ThO_2 fuels in the spectrum of visible light. This approximation was applied to the temperature-independent value of UO_2 from Harding [81] for a certain range of the spectrum. The value resulted for ThO_2 is 0.817275.

TRANSURANUS uses a simplified correlation of the emissivity of UO_2 from Fink [6]. In this correlation at temperatures up to 3120 K the emissivity for wavelengths between 400 and 700 nm is approximated to a constant:

$$\epsilon_{UO_2} = 0.839; T < 3120$$
$$\epsilon_{UO_2} = 1 - 0.16096 \times exp[-3.7897 \times 10^{-4}\Delta T - 3.2718 \times 10^{-7}(\Delta T)^2]; T \geq 3120 \quad (3.33)$$

ΔT stands for $T - 3120$.

Van Uffelen [10] suggested the correlation from the Matpro handbook [53] of MOX fuels for PuO_2 due to the lack of data for this oxide. The correlation is represented in Equation 3.34 where T T is the temperature expressed in Kelvin.

$$\epsilon_{PuO_2} = 0.7856 + 1.5263 \times 10^{-5}T \quad (3.34)$$

3.14. Fraction of heavy metals

The fraction of heavy metals is defined as the ratio between the mass of the heavy metal and the total mass in a lattice, i.e the mass of heavy metals plus the mass of oxygen. The lattice structure in the ceramic compounds used as nuclear fuels follows the CaF_2 crystalline structure, illustrated in Figure 4. The cations, Th, U or Pu, represented in blue are placed in a fcc, while the oxygen atoms, in red, are formed as part of a sc. In this particular polycrystalline lattice there are 4 atoms of heavy metals for 8 of oxygen.

An intermediate configuration in which the content of thorium is 50% was assumed, since thorium as nuclear fuel can be used either as a breeder for ^{233}U when its composition is the

largest (around 90%) or as an additive (less than 10%) like gadolinium [82, 83]. The definition of fraction of heavy metals is therefore defined as follows:

$$FHM = \frac{Massof(Th + U/Pu)ingrams}{Massof(ThO_2 + U/PuO_2)ingrams} = \frac{4(atoms)(0.5 \times 232.038\left(\frac{g^{232}Th}{mol}\right) + 0.5 \times Mm_{U/Pu})}{4(atoms)(0.5 \times 232.038\left(\frac{g^{232}Th}{mol}\right) + 0.5 \times Mm_{U/Pu}) + 8(atoms)16\left(\frac{gO}{mol}\right)} \tag{3.35}$$

The molecular masses Mm for U and Pu were 233.039 and 239.052 respectively that corresponded to the molecular masses of ^{233}U and ^{239}Pu because these nuclides are used to initiate the neutron chain in the fuel. It can also be used the molecular mass of ^{235}U, but this isotope has not been used for the validation of the full TRANSURANUS version for thorium fuels. Nevertheless, its inclusion may not differ too much from the value obtained from ^{233}U. Table 10 summarises the two values calculated from Equation 3.14. The values are quite akin and show that almost 90% of the proportion of the initial mass of the nuclear fuel is formed by the heavy metals.

System	Fraction of heavy metals
ThO_2-UO_2	0.87903
ThO_2-PuO_2	0.88041

Table 10 Comparion of the values of fraction of heavy metals for both thorium-based fuels

4

Extension of the TRANSURANUS burn-up model

One of the first steps in describing fuel rod behaviour is to calculate the power distribution, i.e. at each fuel position the fraction of fissile material burnt or local burn-up, the conversion of ^{232}Th to ^{233}U and the subsequent buildup and fission of the higher U isotopes. Indeed, the power density provides the source term for the temperature calculation, affecting most mechanisms in the code, as well as the source term for the radioactive fission products. The equations used constitute the so-called burn-up models.

Several codes have been developed to calculate the concentration of those radioactive fission products in the fuel throughout the time. One of the most used codes is ORIGEN 2.2 [84] developed at the ORNL. This code is generally coupled with MCNP (Monte Carlo N-Particle) from which the neutron flux and the one-group cross sections are calculated and then used as input parameters for ORIGEN calculations.

The corresponding module included in the TRANSURANUS fuel rod performance code is called TUBRNP and is currently used for oxides fuels with U and Pu. The standalone TUBRNP model is based on the prior depletion model RADAR [41]. TUBRNP is employed in other fuel performance codes like Frapcon [9] and Falcon [85] or as reference in the development of newer codes like BISON [86], AMP [87], the Femaxi model PLUTON [88] and Dionisio [89].

In the standalone TUBRNP model [38, 39, 40] the local power density, $q'''(r)$ is proportional to the one-energy-group effective cross sections for neutron-induced fission $\sigma_{f,k}$, the most relevant nuclides concentration $N_k(r)$ in the thorium fuel cycle, and the thermal neutron flux, $\phi(r)$ derived from the diffusion equation:

$$q'''(r) \propto \sum_k \sigma_{f,k} N_k(r) \phi(r) \tag{4.1}$$

where $q'''(r)$ has units of W/mm^3, the fission cross sections $\sigma_{f,k}$ are introduced in cm^2. $N_k(r)$ are expressed in number of atoms per mm^3, while the thermal neutron flux $\phi(r)$ is accounted in neutron per cm^2 and s.

4.1. Thermal neutron flux

The thermal neutron flux is calculated by solving the diffusion approximation to Boltzmann equation in cylindrical coordinates. This approximation is explained in Appendix A

$$-\Delta\phi(r) + \kappa^2\phi(r) = 0 \tag{4.2}$$

κ stands for the inverse diffusion length and is defined as follows:

$$\kappa = \sqrt{\frac{\Sigma_{a,therm}}{D}}; \Sigma_{a,therm} = \sum_l N_l(r)\sigma_{a,therm,l} \tag{4.3}$$

where $\sigma_{a,therm,l}$ is the microscopic absorption cross section in the thermal range. The subscripts l refers to the most distinctive nuclides accounted for in the thorium cycle. The diffusion coefficient D is calculated as:

$$D = \frac{1}{3\Sigma_t} \tag{4.4}$$

where $3\Sigma_t$ is usually named as the macroscopic transport cross section whose computation is identical to the thermal absorption macroscopic cross section in Equation 4.3. The strict application of the diffusion theory approximates the transport cross section to the elastic scattering cross section, i.e. the diffusion theory assumes an isotropic medium with low neutron absorption.

$$\Sigma_t \approx \Sigma_s \tag{4.5}$$

Commonly, in nuclear fuels this last assumption is not true. The isotopes of U, Pu or Th that form the structure of a nuclear material have a great neutron absorption either for radiative capture (^{232}Th or ^{240}Pu) or neutron-induced fission (^{233}U, ^{235}U and ^{239}Pu). In TUBRNP the diffusion coefficient is approximated by a geometrical factor and a parameter fitted through experimental data, neglecting Equation 4.5. However, a first check of Equation 4.5 was carried out. Normalised power density profiles of two simulations of (Th,Pu)O_2 and UO_2 at very low burn-ups, around 1 MWd/kg HM, depicted a flatter profile of the first fuel in comparison to the UO_2 case study. At this very low burn-up, the diffusion of neutrons is the driver mechanism of heat generation within the fuel. In the extension of TUBRNP to thorium-based fuel no modification for the diffusion constant was implemented and the fitted approach of D was kept.

Eventually, Equation 4.2 is solved analytically by means of Bessel functions [40, 38, 39, 28]:

$$\phi(r) \propto I_0(\kappa r) \tag{4.6}$$

where $I_0(\kappa r)$ is the Bessel function of the fist kind in cylindrical coordinates for normal pellets. In case of annular pellets the solution is the Bessel's function of the second kind , $J_0(\kappa r)$.

4.2. Microscopic cross sections

TUBRNP makes use of the one energy group (spectrum averaged) effective microscopic cross sections for the neutron capture and the neutron-induced fission. The word 'effective' means that after averaging over the neutron spectrum, the microscopic cross sections are then averaged over the geometry and the burn-up or time as described in Equation 4.7.

$$\sigma = \frac{1}{T_{bp}} \int_0^{T_{bp}} \left(\frac{\int_V \int_0^\infty \sigma(E)\phi(\vec{r}, E, bu) dE dV}{\int_V \int_0^\infty \phi(\vec{r}, E, bu) dE dV} \right) dbu \tag{4.7}$$

The term T_{bp} stands for the irradiation time, E is the incident neutron energy, $\vec{r}$ is the position vector and bu the variable that represents the burn-up. $\phi(\vec{r}, E, bu)$ is the neutron flux and finally $\sigma(E)$ and σ are the evaluated and averaged cross sections.

In order to average these cross sections over the spectrum, the continuous-energy Monte Carlo code Serpent [42] was utilized to calculate the neutron flux, $\phi(\vec{r}, E, t)$. The main difference between transport codes like Serpent or MCNP and TUBRNP is the approach of the scalar flux calculation. The transport codes usually employs statistical approaches like collisions rate theory with the main disadvantage of greater computing time.

The representation of the fission cross section of the ^{240}Pu nuclide derived from a Serpent simulation along the burn-up in Figure 23a is a clear example that in almost all the nuclides the time average operation can be omitted.

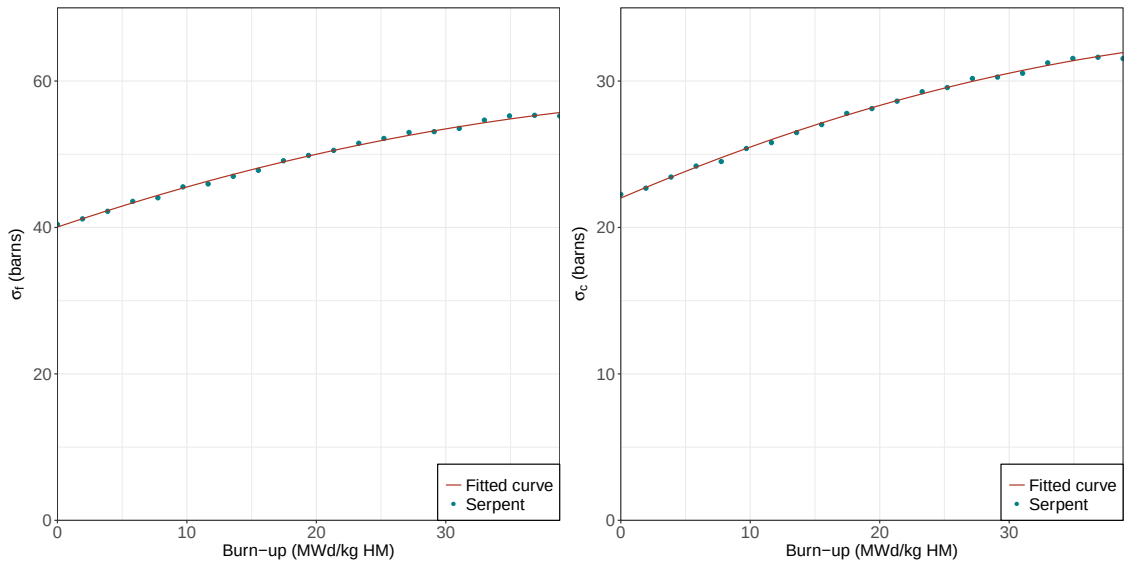

(a) Fission cross section

(b) Capture cross section

Figure 22 Capture and fission-induced cross sections (in barns) of ^{239}Pu

However, in other cases this operation can not be performed because the strong dependence

of the cross section on the burn-up. The radiative capture cross sections of the plutonium isotopes ^{239}Pu, ^{240}Pu and ^{241}Pu and the fission cross section of ^{239}Pu and ^{241}Pu calculated from Serpent, strongly depend on the burn-up, as illustrated in Figures 22a to 23b. Due to this reason, a square root adjust was done to infer the burn-up- dependent correlation that was then included in TRANSURANUS.

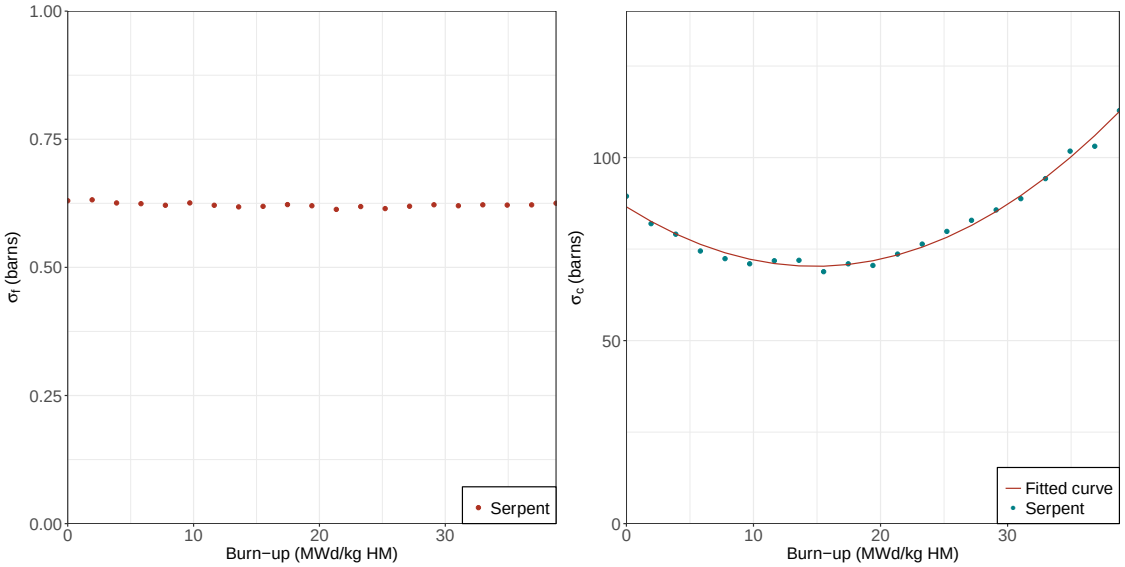

(a) Fission cross section (b) Capture cross section

Figure 23 Capture fission-induced cross section (in barns) of ^{240}Pu

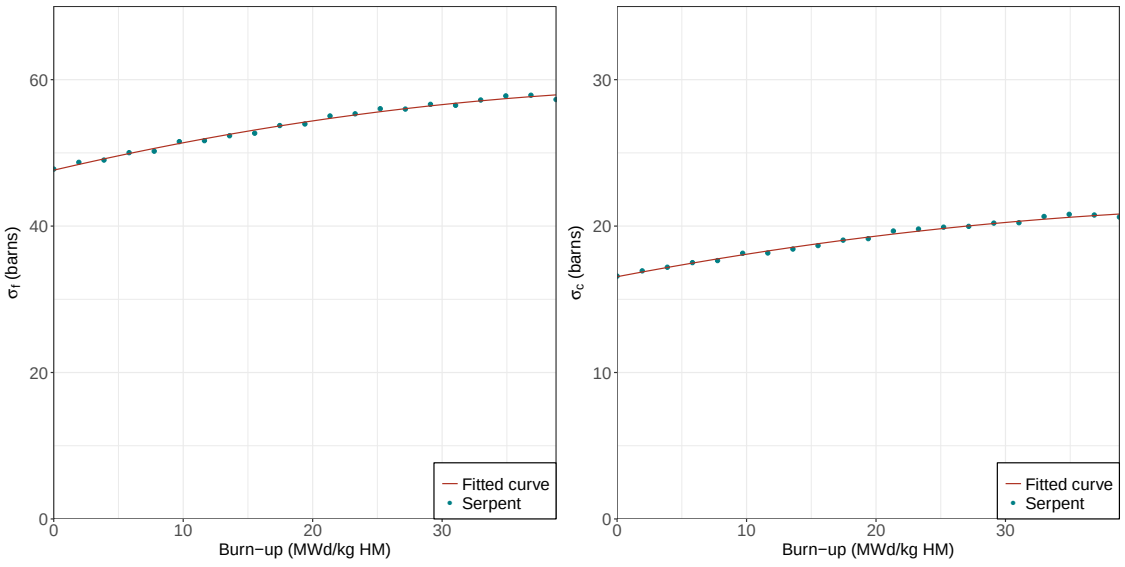

(a) Fission cross section (b) Capture cross section

Figure 24 Capture and fission-induced cross sections (in barns) of ^{241}Pu

This burn-up dependence that these isotopes possess is attributed to the high resonance peaks in the epithermal range of energy (0.625-10 eV) (see Figure 25) that harden the neu-

tron spectrum. The largest peak corresponds to the radiative capture cross section of ^{240}Pu. However the peak that this nuclide shows at the same neutron energy in the case of fission cross section, does not influence in the flux. The height of these resonance peaks (around 50 barns) is comparable to the other fission cross sections of ^{239}Pu and ^{241}Pu that do not exhibit any peak in that neutron energy. These two last isotopes have enough larger resonances in both reactions than ^{240}Pu at approximately 0.5 eV that may influence in the shape of the neutron spectrum. The values of their cross sections calculated with Serpent are smaller as can be appreciated in Figure 25. The increment or decrement of the concentration of these nuclides along the time will harden or smoothen the neutron spectrum respectively, and consequently the one-group effective cross section will vary throughout the time or burn-up. The most important cross section in this particular case is the radiative capture of ^{240}Pu that shows a strong second order polynomial shape. When the cross section is descending, before reaching the minimum, the breeding of this nuclide through capture reaction from ^{239}Pu takes places and hence the neutronic flux is hardened due to the strong absorption of ^{240}Pu in the epithermal range. After the minimum, less ^{240}Pu is bred as lower fresh content of ^{239}Pu remains in the fuel, and therefore there is no more neutron absorption of ^{240}Pu and the neutron flux is smoothened again.

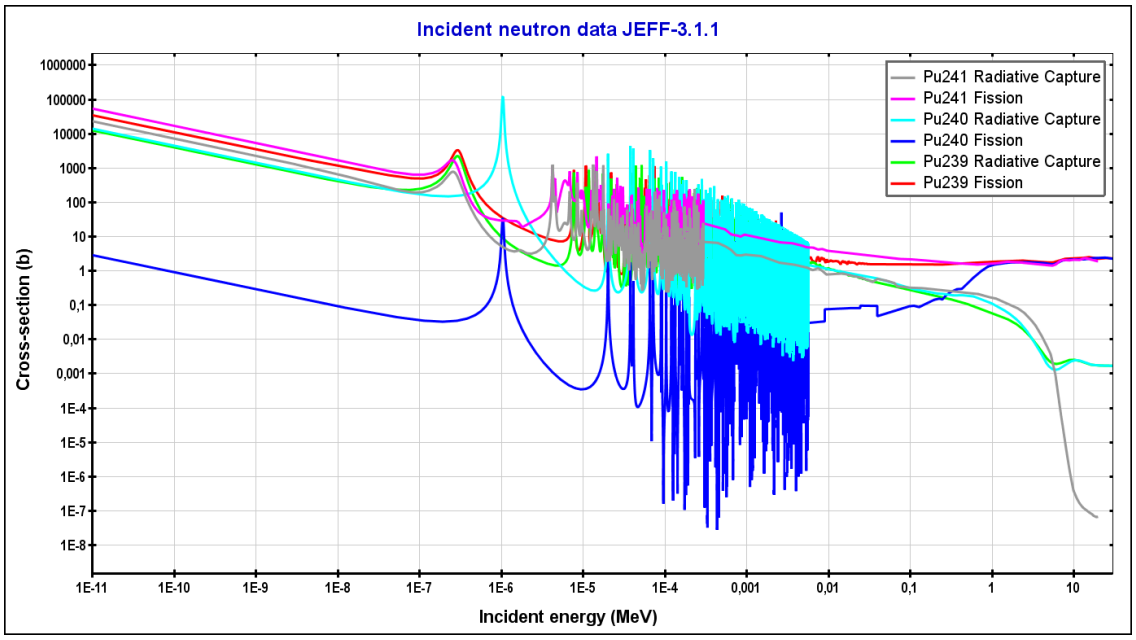

Figure 25 Comparison of the radiative capture and fission cross section (in barns) of ^{239}Pu, ^{240}Pu and ^{241}Pu generated with NEA program JANIS-4.0 [11]

The phenomenon of the neutron spectrum being hardened by the inclusion of Pu can be clearly appreciated by comparing Figure 26 and 27. In Figure 26 at neutron energies between 0.1 and 1 eV the shape of the Boltzmann distribution of the thermal neutron spectrum can clearly be appreciated whereas in Figure 27 the spectrum cannot be recognized. The inclusion of plutonium, especially ^{240}Pu with its resonance peak at the same range of neutron energies distorts the shape of the flux. Moreover, at EOL (End of Cycle), when a large amount

of plutonium is incinerated, the neutron spectrum is smoothened, again and the Boltzmann distribution can be appreciated.

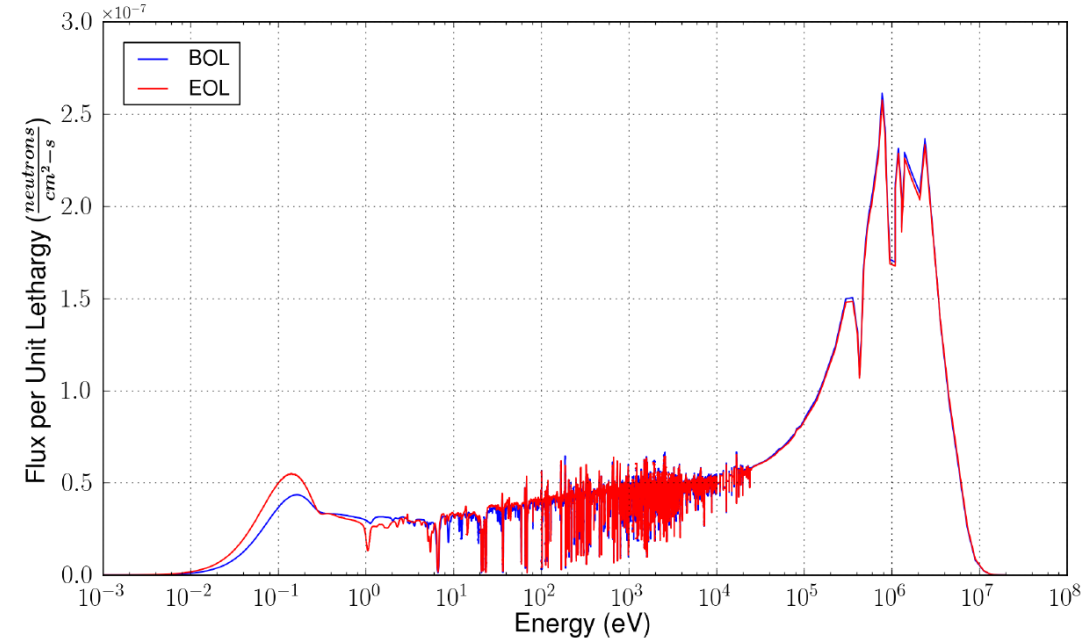

Figure 26 Neutron spectra at BOL and EOL of Th-U fuel extracted from [12]

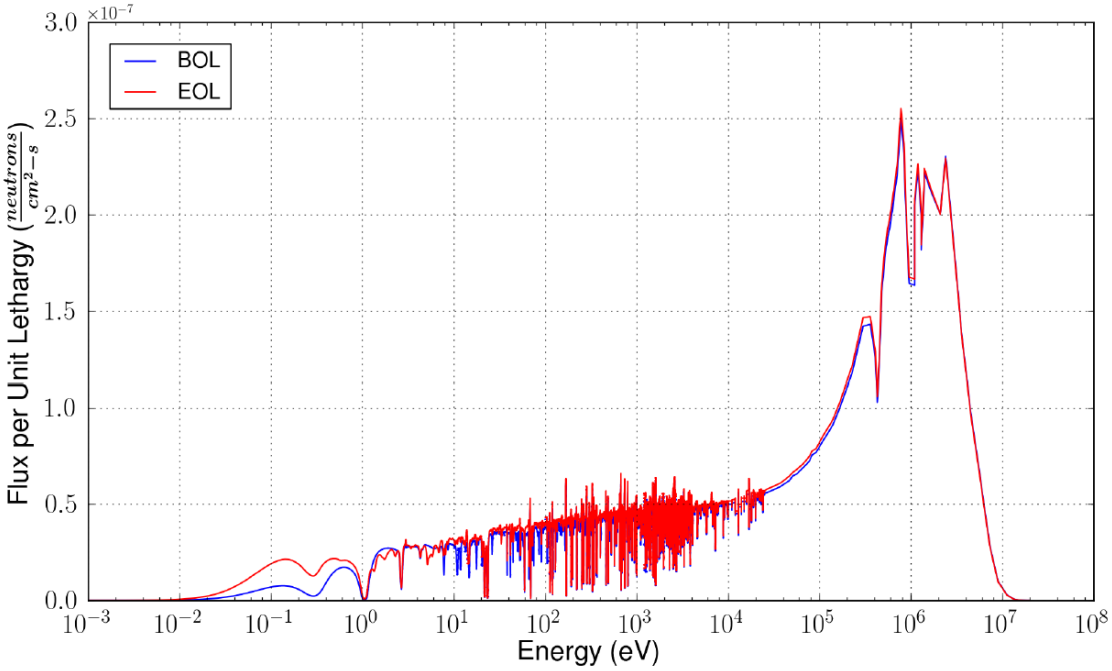

Figure 27 Neutron spectra at BOL and EOL of Th-Pu fuel extracted from [12]

4.2.1. Radial power profile functions

The computation of the one-group energy or spectrum average cross section, Equation 4.7 results in a constant value for the whole range of incident neutron energy. This averaged value underestimates the evaluated cross section at the epithermal range of energies, which can clearly be contemplated in Figure 28. The displayed capture cross section of ^{240}Pu that was PWR spectrum averaged from JANIS-4.0 [11] is smaller in some ranges of neutron incident energies.

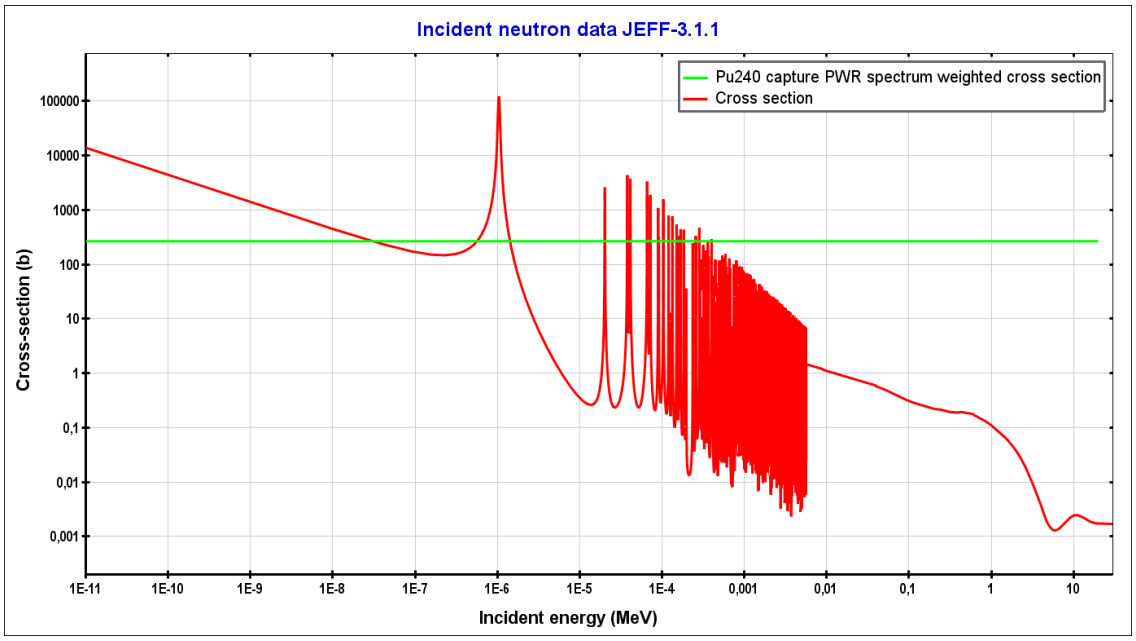

Figure 28 Comparison of the PWR spectrum average absorption and evaluated absorption cross section (red) of ^{240}Pu generated with NEA program JANIS-4.0 [11]

The resonances in the epithermal range of energies have an impact in the concentration of the nuclides along the pellet radius, especially at the rim of the pellet. A neutron, born after a fission event, possesses a high kinetic energy, typically 2 MeV (see Figure 28). The neutron will be slowed down by elastic collisions with light nuclei in the moderator. At slower velocities the neutrons have more possibilities to produce a reaction with the atom, for example a fission, or, in the case of Figure 28, a radiative capture as the cross sections are larger. Nevertheless, during the slow-down process the neutrons can be captured by atoms with high resonance peaks before the thermal energy range (below 0.625 eV energies in Figure 29). This phenomenon is called self-shielding and takes place in the outer region of the pellet, because this area is the nearest part of the pellet to the moderator, where the elastic collisions with water atoms occur.

In order to account for the resonance absorption in the epithermal range at the rim of the pellet for thorium-based fuels cases, radial form functions $f_i(r)$ are developed and included in the depletion equations of ^{232}Th and ^{240}Pu, see Equations 4.11. In contrast to previous developments [38, 39, 40] in which these functions were fitted from experimental data, a the-

oretical approach is presented. The main idea is based on the ratio between the absorption reaction rates of these two nuclides and ^{233}U. The election of ^{233}U is due to this nuclide does not present resonance peaks in the epithermal range [1].

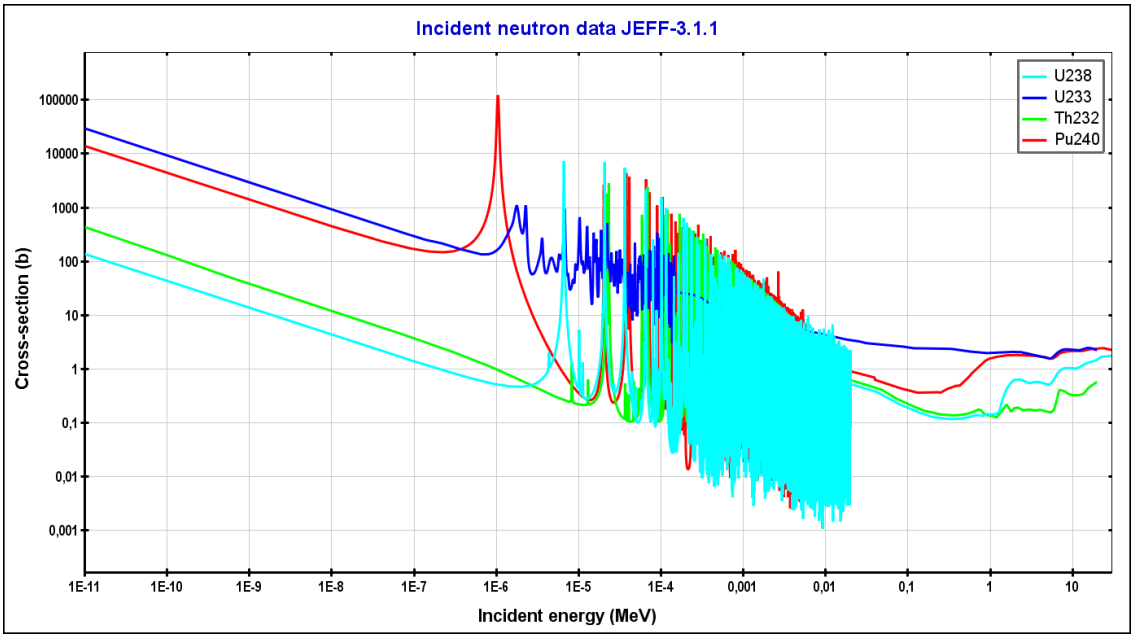

Figure 29 Absorption cross sections (in barns) of the nuclides ^{240}Pu, ^{238}U, ^{233}U and ^{232}Th generated with the NEA program JANIS-4.0 [11]

Two simulations were run with Serpent by using the tool 'detector' [42]. In the first simulation, the absorption reactions were calculated in 10 equi-volume rings in which the pellet was divided while in the second simulation the pellet was not subdivided. The purpose of this second simulation was the volume-normalisation of the absorption rates. The normalised function $h_k(r)$ where k refers to ^{232}Th, ^{240}Pu and ^{233}U:

$$h_k(j) = \frac{\frac{\int_{V_j}\int_0^\infty \sigma_{a,k}(E)\phi(\vec{r},E)d^3\vec{r}dE}{\int_{V_j}\int_0^\infty \phi(\vec{r},E)d^3\vec{r}dE}}{\frac{\int_{V_{pellet}}\int_0^\infty \sigma_{a,k}(E)\phi(\vec{r},E)d^3\vec{r}dE}{\int_{V_{pellet}}\int_0^\infty \phi(\vec{r},E)d^3\vec{r}dE}} \tag{4.8}$$

i.e. as a ratio of a detector for ring j over a detector for the whole fuel pellet. Here $\phi(\vec{r},E)$ is the neutron flux derived from the Boltzmann equation, $\sigma_{a,k}(E)$ expresses the microscopic absorption cross section and V_j and V_{pellet} are the volumes of the ring j and the whole pellet, respectively. Finally, the ratios between the nuclides ^{232}Th and ^{240}Pu and ^{233}U are computing in each of the 10 rings.

$$f_{Th232/Pu240}(j) = \frac{h_{Th232/Pu240}(j)}{h_{U233}(j)} \tag{4.9}$$

As a final step, a root mean square adjust was made to fit the values obtained in the computation of $f_{Th232/Pu240}(j)$ in each equi-volume ring j to the analytical function represented in

Equation 4.10 [38, 40, 39].

$$f(r) = 1 + a \times e^{-b(R_{pellet}-r)^c} \tag{4.10}$$

Here a, b and c are fitting parameters and R_{pellet} is the outer fuel radius. In order to verifiy that this approach was correctly performed, those parameters for ^{240}Pu were previously derived from a 3.5 wt.% ^{235}U enriched rod in a MOX assembly whose specifications were identical to the KWO assembly (see Section 6.1). The graphical and numerical comparison of the parameters are displayed in Figure 30 and Table 11 respectively. The appreciable difference is due to the non-normalised implemented function in TUBRNP, actually TUBRNP volumetrically normalises these functions during its execution. Although the TUBRNP function was fitted on a wide range of MOX fuel scenarios, the shape and curvature of both functions can be regarded as similar.

	TRANSURANUS	Serpent
a	3.45	1.45
b	3.0	0.589
c	0.45	0.129

Table 11 Comparison of the fitting constants in the resonance functions

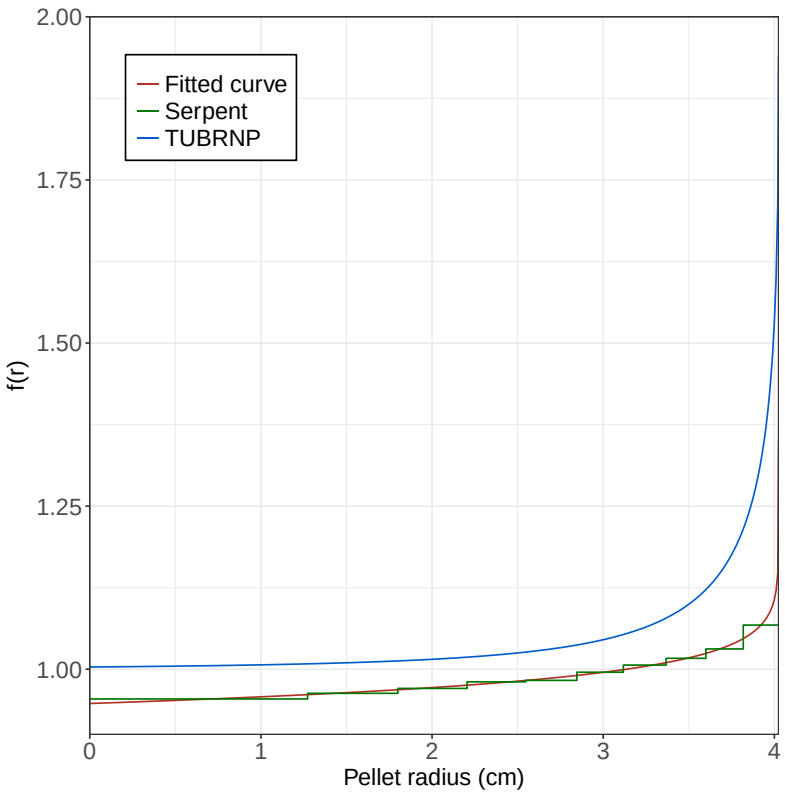

Figure 30 Comparison of the radial profile functions from TRANSURANUS and derived from a certain MOX simulation

On the other side, Figure 31 shows the resonance function for ^{240}Pu in (Th,Pu)O_2 fuels, whose shape is smoother for this type of fuels than in MOX. This method was also employed by Mieloszyk [13] for the extension of the FRAPCON code from MCNP to (Th,U)O_2 fuels under low moderation conditions. A graphical comparison of the function inferred through Equation 4.8 in this work to the derived by Mieloszyk for ^{232}Th is depicted in Figure 32. The difference between both functions at the rim of the pellet can be attributed to the type of reactor (i.e. neutron spectrum) used in each simulation. While in this work, the studied case was a PWR assembly from KWO, in Mieloszyk's work the reactor considered was a RBWR (Reduced Moderation Boiling Water Reactor). This low-moderator reactor tends to produce less neutron absorption reactions on the periphery of the fuel pellet, hence the flatter profile shown in Figure 32 in comparison to conventional LWR.

In Mieloszyk's work a radial profile function for ^{238}U was also included. However, an analysis of this process for ^{238}U (not shown in this work) reveals that its radial power function is flat, hence there is no need to include it. Moreover, the contribution of ^{238}U to any type of thorium-based fuel can be dismissed. The breeding of ^{238}U through a sequence of radiative capture reactions from ^{233}U is unlikely to happen since the fission cross sections of ^{233}U and ^{235}U are larger than their neutron capture cross sections [1].

In the extension of Frapcon to Th-Pu fuels, Insulander [90] also inserted a radial power shape function for ^{239}Pu. An identical assessment led to the same conclusion for ^{238}U. Furthermore, a graphical comparison of the cross section for all the plutonium isotopes in Figure 25 shows no relevant resonance peak for ^{239}Pu in the range of epithermal energies (0.625-100 eV), and therefore no necessity to introduce radial absorption functions was required for this nuclide. The fitted parameters of the radial power-shape function of ^{240}Pu and ^{232}Th for (Th,Pu)O_2 are listed in Table 12. For (Th,U)O_2 fuels the same parameters of ^{232}Th are used, while in ^{240}Pu the resonance absorption is neglected because Pu is not considered in this type of fuel.

	^{232}Th	^{240}Pu
a	1.95	1.34
b	2.56	0.931
c	0.531	0.815

Table 12 Fitting parameters a, b and c of ^{232}Th and ^{240}Pu [26]

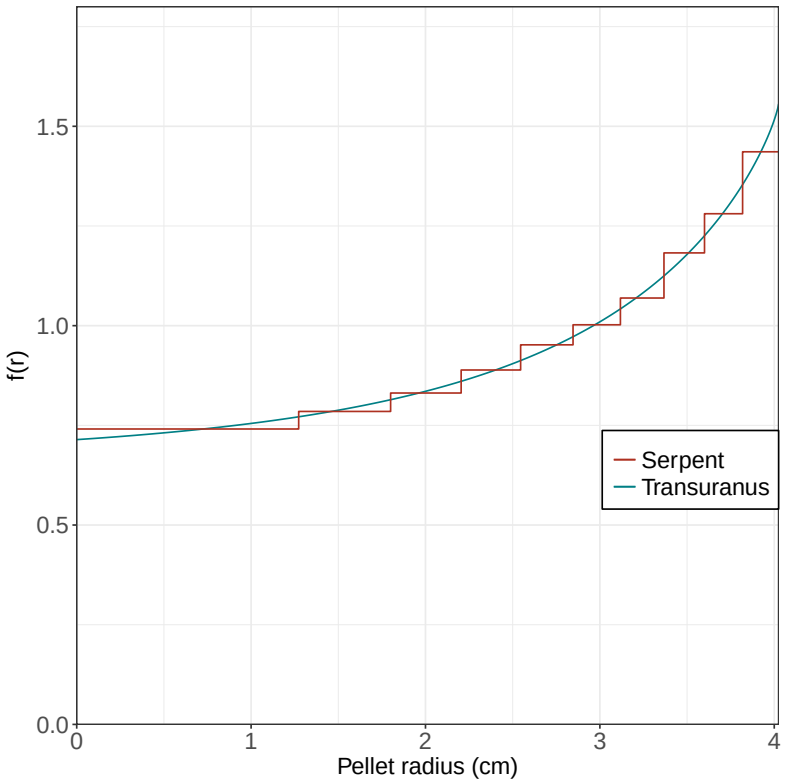

Figure 31 Radial profile function of ^{240}Pu for Th-Pu fuels derived from Serpent and included in TRANSURANUS

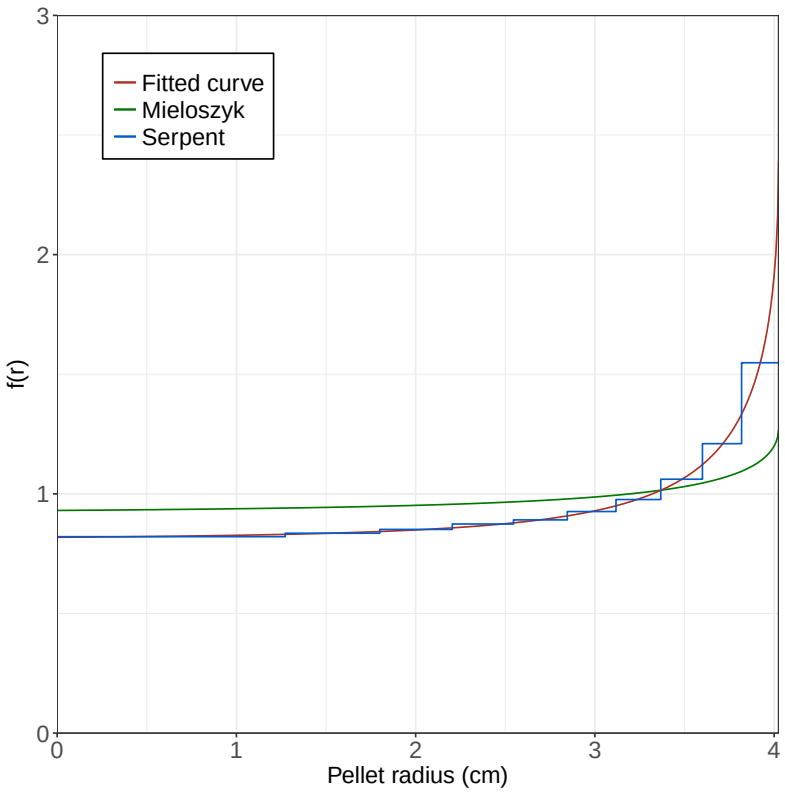

Figure 32 Comparison of radial profile functions derived from Serpent and included in TRANSURANUS for ^{232}Th for Th-Pu cases to the one derived by Mieloszyk [13] for Th-U fuels

4.3. Depletion Equations in the Thorium cycle

The TUBRNP model has been extended in this work for thorium-based fuels by including the set of Bateman equations that describe the isotopic behaviour through the time and as a function of the radius. The set of depletion equations in TUBRNP for thorium fuels is extended to include the nuclides ^{232}Th, ^{233}U and ^{234}U and the breeding of ^{235}U through neutron capture in ^{234}U. In this first thorium version of TUBRNP the generation of ^{233}U is approximated to an immediate radiative capture in ^{232}Th by neglecting the formation of ^{233}Th and ^{233}Pa. The generation of ^{232}U through a (n,2n) reaction is also disregarded due to the small cross section of this reaction [1].

$$\begin{aligned}
\frac{dN_{Th232}(r)}{dbu} &= -A\sigma_{a,Th232}N_{Th232}(r)f_{Th232}(r) \\
\frac{dN_{U233}(r)}{dbu} &= -A(\sigma_{a,U233}N_{U233}(r) - \sigma_{c,Th232}N_{Th232}(r)f_{Th232}(r)) \\
\frac{dN_{U234}(r)}{dbu} &= -A(\sigma_{a,U234}N_{U234}(r) - \sigma_{c,U233}N_{U233}(r)) \\
\frac{dN_{U235}(r)}{dbu} &= -A(\sigma_{a,U235}N_{U235}(r) - \sigma_{c,U234}N_{U234}(r))
\end{aligned} \tag{4.11}$$

where $N_k(r)$ is the concentration of nuclide k, $\sigma_{a,k}$ and $\sigma_{c,k}$ are the one-group effective absorption and capture cross section, $f_{Th232}(r)$ is a radial form function, that takes into account the resonance absorption of epithermal neutrons, as described in Subsection 4.2.1. A is a conversion factor that transforms the original time step into the burn-up step, dbu [38].

$$A = 0.8815\frac{\rho_{fuel}}{\alpha\sum_k \sigma_{f,k}N_k} \tag{4.12}$$

In Equation 4.12, ρ_{fuel} is the fuel density, $\sigma_{f,k}$ and N_k are the fission cross section and concentration of nuclide k respectively and finally, α is a conversion factor that takes the value of 3.8 $\times$ 10^{-16} [38].

The last implementation in TUBRNP for thorium-fueled cases was the yield fission products of ^{233}U. Table 13 collects the fission yields for all the fission products included in TUBRNP.

Fission product	^{233}U Fission yield
^{137}Cs	6.2045×10^{-2}
^{80}Kr	3.0507×10^{-7}
^{82}Kr	7.0235×10^{-5}
^{83}Kr	1.0699×10^{-2}
^{84}Kr	1.6974×10^{-2}
^{85}Kr	5.2303×10^{-3}
^{86}Kr	3.0880×10^{-2}
^{142}Nd	3.3062×10^{-8}
^{143}Nd	5.9068×10^{-2}
^{144}Nd	4.6554×10^{-2}
^{145}Nd	3.3989×10^{-2}
^{146}Nd	2.5290×10^{-2}
^{148}Nd	1.2939×10^{-2}
^{150}Nd	4.8731×10^{-3}
^{126}Xe	4.8442×10^{-11}
^{128}Xe	6.3709×10^{-8}
^{129}Xe	6.9967×10^{-10}
^{130}Xe	3.2488×10^{-5}
^{131}Xe	3.5653×10^{-2}
^{132}Xe	4.7975×10^{-2}
^{133}Xe	5.9825×10^{-2}
^{134}Xe	6.2896×10^{-2}
^{135}Xe	5.4715×10^{-2}
^{136}Xe	8.5850×10^{-2}

Table 13 ^{233}U Fission yields

5

Extension of the TRANSURANUS fission gas release models

Figure 33 illustrates the fission yields of the fission products for the actinides ^{233}U, ^{235}U and ^{239}Pu. As can be observed there are two fission yield peaks of about 10% at approximately atomic masses 90 and 140 respectively. This means that most probable fission products born have atomic masses around those values, corresponding to either metallic precipitates (Mo, Tc, Ru, Rh or Pd) or oxide precipitates (Rb, Cs, Ba, Zr, Nb, Mo or Te) or noble gases (Xe or Kr) [91].

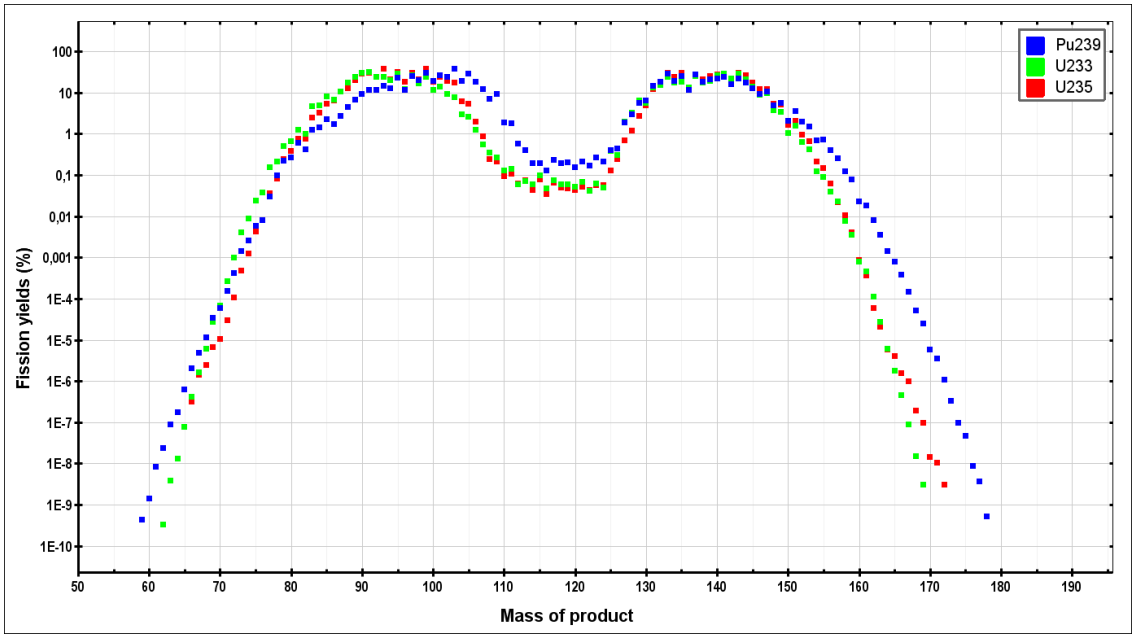

Figure 33 Comparison of the fission yields of ^{233}U, ^{235}U and ^{239}Pu along the atomic mass of the fission products generated with NEA program JANIS-4.0 [11]

The inclusion of these fission products in the fuel lattice has consequences directly on the behaviour of the fuel. For example, due to their low solubility, the fission gases or volatile products (Cs or Te) may either be rejected from the fuel pin (gas release), or precipitate as small pockets [92], for example inter-granular bubbles, in the lattice (swelling). In the case of the gas is released to the free volume within the rod, the pressure correspondingly increases and the cladding is subjected to an stress that can ultimately result in rod failure. In addition, the fission gases inside the pin decrease the gap conductance, increasing the fuel temperature profile. An increment of the fuel temperatures enhances further fission gas release and

initiates a non-stable process. If the fission gases precipitate within the fuel matrix, they might do it as bubbles. These bubbles occupy a larger volume than the fissile atoms or the solid products atoms segregated. The precipitation of these bubbles leads to a swelling of the fuel, which may enhance the PCMI (Pellet-Cladding Mechanical Interaction), especially in power transients. Another important aspect of the retention of the bubbles in the fuel pellet is the degradation of the thermal conductivity that may cause an increment of the temperature [3]. These two effects, swelling and fission gas release are thus complementary.

The experimental data or studies of fission gas release in thorium-based fuels in the literature are limited. As a guideline for further research, data from uranium might be used as a first approximation, since thorium and uranium dioxides crystallise in the same structure, cubic fluorite, [93] displayed in Figure 4. However, the higher melting point of thoria and urania and the lower self-diffusivity of Th^{4+} than U^{4+} in the respective oxide lattices [94] may undergo a lower release rate of fission gases. Another additional and important difference between thoria and urania is the electronic configuration. The electronic configuration of thorium is [Rn]($6d^2$)($7s^2$) having two of the last 4f electrons electrons in orbital 6d and the other two in orbital 7s that result in a strict oxidation state of +4. In contrast, the electronic configuration of uranium is [Rn]($5f^3$)($6d^1$)($7s^2$) [8] having two unpaired 5f electrons [93] that make uranium to have +4, +5 and +6 oxidation states. These oxidation states contribute to the appearance of the non-stoichiometry ($UO_{2\pm x}$) in this solid crystalline compound. The non-stoichiometry of uranium causes the point defects in its structure like oxygen vacancies or interstitials (Frenkel pairs Figures 34a and 34b) that enhances the diffusion of fission gases like Xe through the lattice and finally its release to the free volume [93].

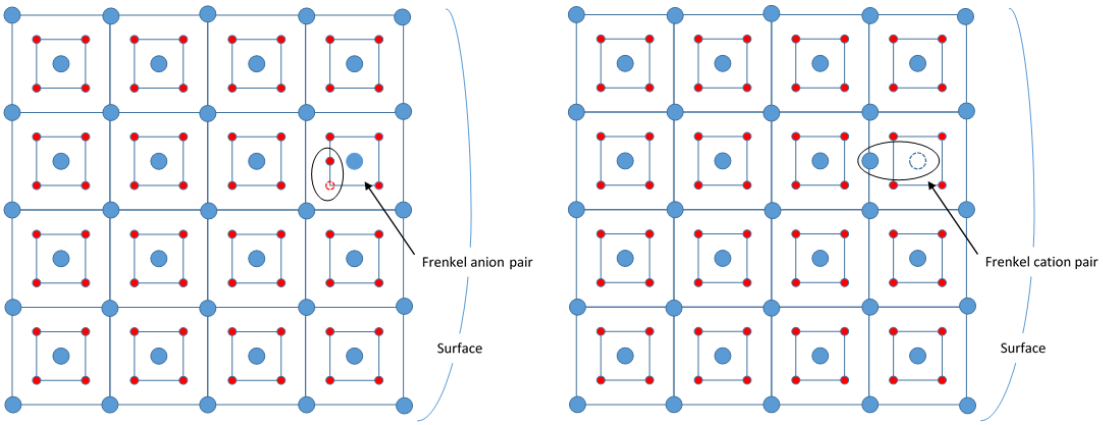

(a) Anion Frenkel pair (b) Cation Frenkel pair

Figure 34 Cation-vacancy and anion-vacancy Frenkel disorder in a CaF_2 lattice

Furthermore, the higher vacancy migration energy and anion interstitial migration energy in thorium (2.8 and 3.27 eV) than in uranium (2.6 and 2.6 eV) [34] might also justify the lower diffusion of gaseous and volatiles fission products in the thoria lattice, especially at low burn-ups when the diffusion of the fission gases through the point defects is the main

mechanism. Other minor differences based on the different electronic configuration are the colour, electronic conductivity, magnetism [8] and corrosion with oxygenated water [93].

5.1. Mechanisms of fission gas release

5.1.1. Recoil and knock-out

When a fission event occurs, two fission products are born and driven apart with high kinetic energy [92]. These two fission fragments electronically interact with the lattice and lose their kinetic energy as they diffuse through the lattice, for example through atomic displacements [34]. If a fission event happens close enough to the surface (6-7 μm), the fission fragments may be released before losing all its kinetic energy. This release mechanism is called direct recoil. In case that the fission fragment loses all its kinetic energy before being released, it stays in the lattice and becomes a fission product [3]. In some cases the fission fragments can produce elastic collisions with the atoms of the lattice, acquiring the later a kinetic energy of about 100 keV [3]. An atom struck by the fission fragment is called a primary knock-on. The primary knock-on created near the surface (200 Å [3]) may be released before it comes to rest. Otherwise, this primary knock-on atom can transfer its energy by elastic collision to another atom which is called a secondary knock-on. If these strikes repeatedly happen, it may have trigger a higher order knock-on called a cascade. The mean energy and its range of these higher order knock-ons are less than those primary knock-ons.

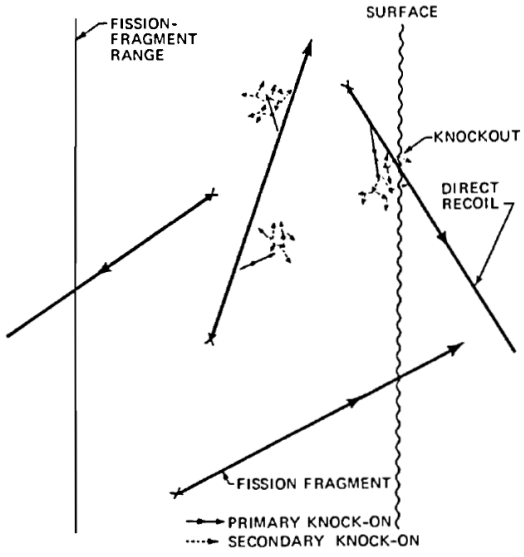

Figure 35 Fission gas release by direct recoil and knock-out [3]

Figure 35 illustrates both the direct recoil and the knock-out mechanisms as they happen within the range of a fission fragment. Direct recoil and knock-out release are mechanisms that dominate at low temperatures ($<$ 900 K) and are also temperature-independent. The contribution of this athermal mechanisms to the overall fission gas release rate is very low (around 1%) and it happens at burn-ups below 60 MWd/kg HM [34].

5.1.2. Lattice diffusion of single gas atom

The motion of a single gas atom in the lattice is driven by either vacancies, interstitiasl or vacancies-interstitials diffusion. However, Olander [3] and Das [34] stated that the diffusion of a single gas atom of, for example, Xe can occur by means of the vacancy of one uranium atom and two oxygen atoms (Schottky trios Figure36), since the xenon atoms are too large to have any mobility into any single vacancy or interstitial position. The atomic radius of xenon is 0.216 nm, twice larger than U^{+4} and Th^{+4} ionic radii which are 0.101 and 0.107 nm respectively [93].

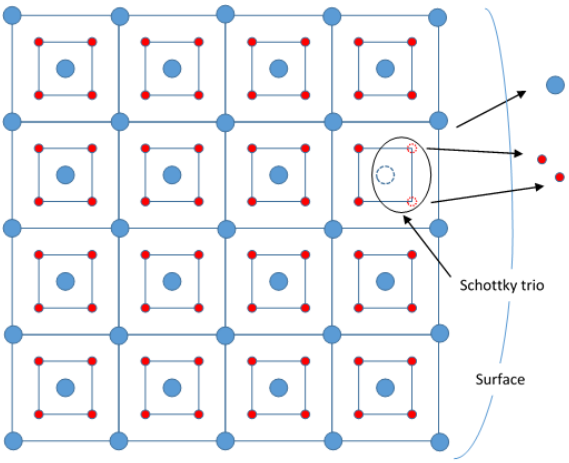

Figure 36 Schottky trio vacancy, MO_2, in a fluorite lattice

The random-walk accurately explains the diffusion mechanism [3]. The Einstein's formula relates the macroscopic quantity, D, which is known as diffusion constant to the atomic properties jump distance λ and the total jump frequency, Γ. The total jump frequency can be further developed as a function of the single jump frequency ν, the entropy and the energy of motion [3]. The exponential term that accounts for the excess of entropy is generally simplified to one. The expression of the diffusion constant for a single gas atom has Arrhenius law form (Equation 5.1) whose exponential term therefore depends on the enthalpy only:

$$D = \lambda^2 \nu e^{-\frac{\Delta H}{RT}} = D_0 e^{-\frac{\Delta H}{RT}} \tag{5.1}$$

D_0 is the pre-exponential term that depends on the jump frequency λ and the vibration frequency ν whereas ΔH is the activation enthalpy, R the universal gas constant and T is the temperature expressed in Kelvin.

The diffusion lattice constant may depend on several factors: (a) stoichiometry; (b) additives such as Nb to increase the grain size and, consequently, the diffusion constant, releasing less gas to the free volume; (c) burn-up, when changes in the structure occur, stoichiometry and composition of the fuel due to fission events may produce some of the above mentioned defects; (d) phase changes; and (e) radiation-induced enhanced diffusion where vacancies

and interstitials are created when a fission fragment strikes an atom in the crystalline structure. The later is therefore knocked far from its original site and will not return immediately to it[95].

5.1.3. Trapping

When the fission gas atoms do not have enough kinetic energy to overcome the natural (grain boundaries, dislocation lines, closed pores and impurities) or irradiation induced defects (fission gas bubbles, vacancy clusters, dislocation loop and solid fission product precipitation) in the lattice, they are trapped permanently and can not escape from their lattice position. Among all these defects, the electronic displacements which are electronic collisions between fission fragments and lattice atoms are the most probable cause for the high concentration of vacancies in a small volume. Consequently, this concentration of vacancies may collapse and form voids or dislocation loops where bubbles of gas atoms can spontaneously nucleate [14]. TEM (Transmission Electron Microscopy) has shown that those bubbles nucleate in lines that correspond with lattice atoms displacements created by fission fragments at temperatures below 1000°C (see Figure 37).

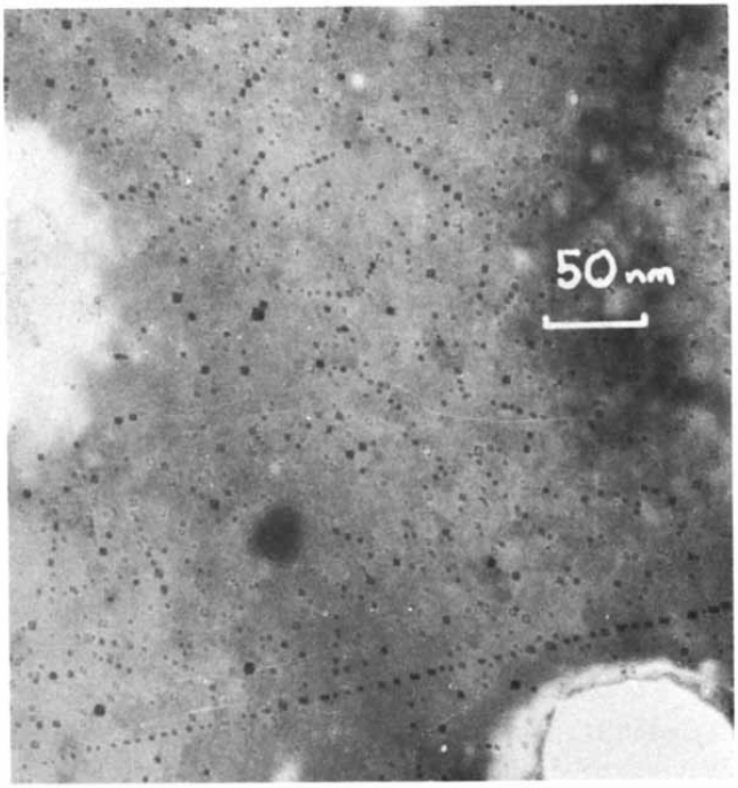

Figure 37 Bubble nucleation in fission-induced dislocations [14]

It must be noted that this fission gas bubble formation occurs within the grains and is different from the inter-granular fission gas bubble formation, which takes place along grain boundaries.

5.1.4. Irradiation induced resolution

The opposite mechanism to the fission gas bubble formation is the irradiation induced resolution. The fission fragments have not only a higher initial kinetic energy (about an average of 80 MeV) than other particles like gamma rays or neutrons, but also a higher cross section for transferring energy either to the lattice or other gas atoms [96]. There are two main theories that explain the resolution of gas atoms into the lattice due to fission fragment impacts. The first theory states that a gas atom or a primary knock-on uranium ion strikes a gas atom within the bubbles with the consequence that the last one is knocked out of the bubble. The second theory assumes the complete destruction of the gas bubble that corresponds to the observations [96, 97].

5.1.5. Grain boundary diffusion

The diffusion in polycrystalline materials through grain boundaries is much faster than within the grain due to a lower energy barrier [34] and an around million times higher jump frequency [95]. The grain boundary diffusion apparently takes place through the vacancy mechanism [34, 95] and, therefore, can only be considered at low temperatures ($T \leq 2/3 T_m$; T_m melting temperature), because the higher the temperatures are, the higher the jump frequency in the lattice [95]. Moreover, at higher burn-ups the grain boundary diffusion contributes to the precipitation of gas atoms in the form of inter-granular bubbles, that will then interconnect to create tunnels through which the gases are released to the free surface [98].

5.1.6. Grain boundary sweeping or grain growth

At temperatures between 1900 and 2100 K, equi-axed grains ($\approx \frac{R_{pellet}}{2}$ region) spontaneously grow in size at the expense of the adjacent smaller grains. The process involves movement of matrix atoms from the convex to the concave side of curved grain boundary, the grain boundary thus moves in the opposite direction of the net flow of atoms. The reason of this movement is that the concave side is surrounded by larger amount of atoms [3]. The grain growth phenomenon affects the fission gas release in three ways [99]. First of all, grain boundary sweeping provides another mechanism for the collection of the fission gas at these internal surfaces from which release can occur [100]. The collection results from the fact that the fission gas is almost insoluble in the fuel matrix, hence the sweeping grain boundary does not redeposit any gas in the newly-formed crystal behind it. The moving grain boundary acts as a fission gas filter [95]. Secondly, the diffusion distance for the fission gas atoms created in the grains increases. Unlike the first consequence, this tends to reduce the release rate [95]. Thirdly, the grain growth also reduces the capacity of the grain boundaries for storing fission gas, as their total surface-to-volume ratio decreases [99].

5.1.7. Bubble migration

The intra-granular bubble migration mechanism is a complementary phenomenon to the sequence ”bubble formation-resolution gas atom diffusion” [43]. The bubbles within the grain subjected to a temperature or stress gradient would migrate in the direction of the gradient by volume diffusion in the matrix [14, 101, 102]. On the other hand, in case the bubble is

not subjected to any gradient it is subjected to a Brownian motion. Cornell [103] stated that Brownian motion is unlikely to happen and the bubble will move due to a gradient. Matzke [43] states that the bubbles are small due to fission-induced resolution and they are pinned in the lattice by crystal defects. Only when the bubble size is large enough (5000-10000 Å) [3] and the temperature is at 2073 K [43], the mobility of bubbles happens due to the thermal gradient. Bubble migration is an important phenomenon because it entails bubble coalescence, i.e. larger bubbles created by the merging of smaller bubbles, which causes fuel swelling and pore migration enhances the columnar grain growth resulting in a central void formation [15].

5.1.8. Bubble interconnection

Gas atoms may migrate out of the lattice and accumulate as bubbles in the grain faces and edges at a certain burn-up, and as the burn-up increases these bubbles grow in numbers and size and undergo interconnection [104]. The interconnection is a reversible process since the tunnel network created can be closed again under the influence of the surface tensions [95]. By the onset of bubble interconnection the release of fission gases remains small, since only athermal release is accounted for. This incubation period is reflected in the Vitanza threshold for fission gas release [95, 98]. Once the grain face bubble interconnects and forms a tunnel network (see Figure 38), a sudden release of the gas accumulated in these bubbles happens, referred to as a burst release [43].

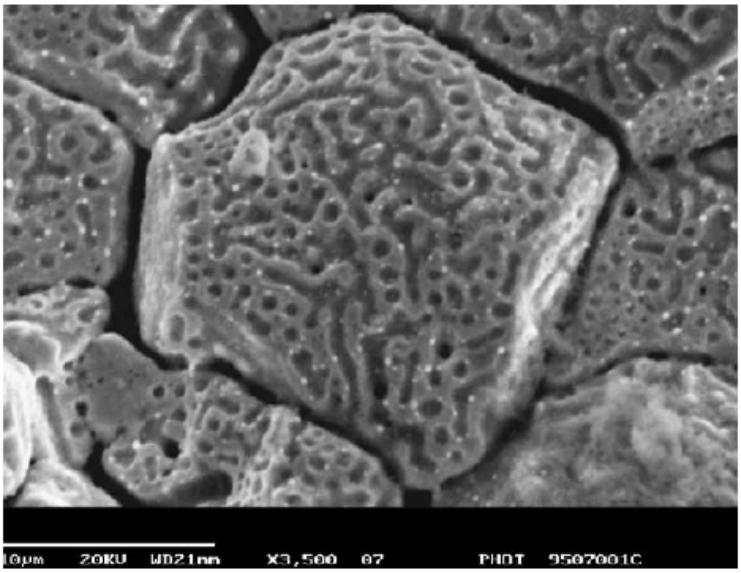

Figure 38 Grain bubble porosity published by White [15]

5.1.9. High Burn-up Structure

As was described in the Subsection 4.2.1, the strong neutron absorption in the epi-thermal range of thorium results in the depletion of this element at the periphery of the fuel pellet. Consequently, the concentration of uranium produced through this reaction at the outer part of the

pellet is higher and it then decreases exponentially along the pellet radius. This effect is also observed in UO_2 and MOX, but, in this case, with the breeding of plutonium from uranium via neptunium. This redistribution of the elements yields an increment of the burn-up at the rim (around 2-3 times the average burn-up), knowing this region as high burn-up structure HBS. This region is characterised by the appearance of large pores (between 20-30% [92]) where the noble fission gases are depleted, producing eventually an enhancement of swelling. Blair [92] points out that HBS only occurs when the local burn-up exceeds approximately 55-82 MWd/kg HM and temperatures remaining below 1100 K [92] (see Figure 39).

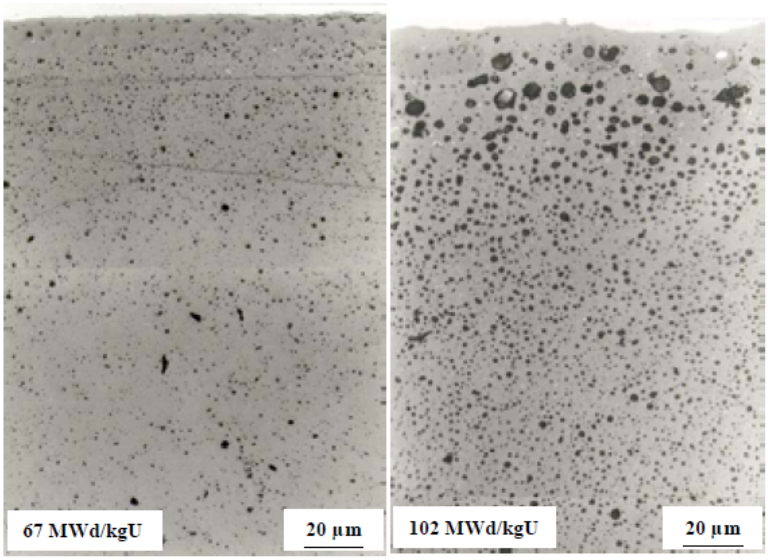

Figure 39 Comparison of the HBS porosity at 102 MWd/kg HM with a non-HBS of 67 MWd/kg HM in the same fuel region [16]

Figure 40 helps to sum up all the phenomena that happen until the fission gas are released:

1. Production of fission noble gases Xe and Kr. In case that these fission fragments are close enough to an outer surface, they will be release immediately, calling the phenomenon direct recoil or knock-out.
2. Nucleation of gas bubbles when two or more gas atoms are trapped in a defect such as a pore.
3. Growth of gas bubbles by atomic migration of fission gas atoms to the existing bubbles.
4. Irradiation induced re-solution of the gas atoms within the bubbles to the bulk.
5. Migration of bubbles driven by temperature gradients, for example.
6. Interaction of the bubbles with crystal defects like dislocation or grain boundaries. This process can be facilitated by the grain boundary sweeping as the grain grows.
7. Boundary or edge bubbles interconnection, creating a tunnel network through which a fraction of the gases is released to the fuel rod free volume.

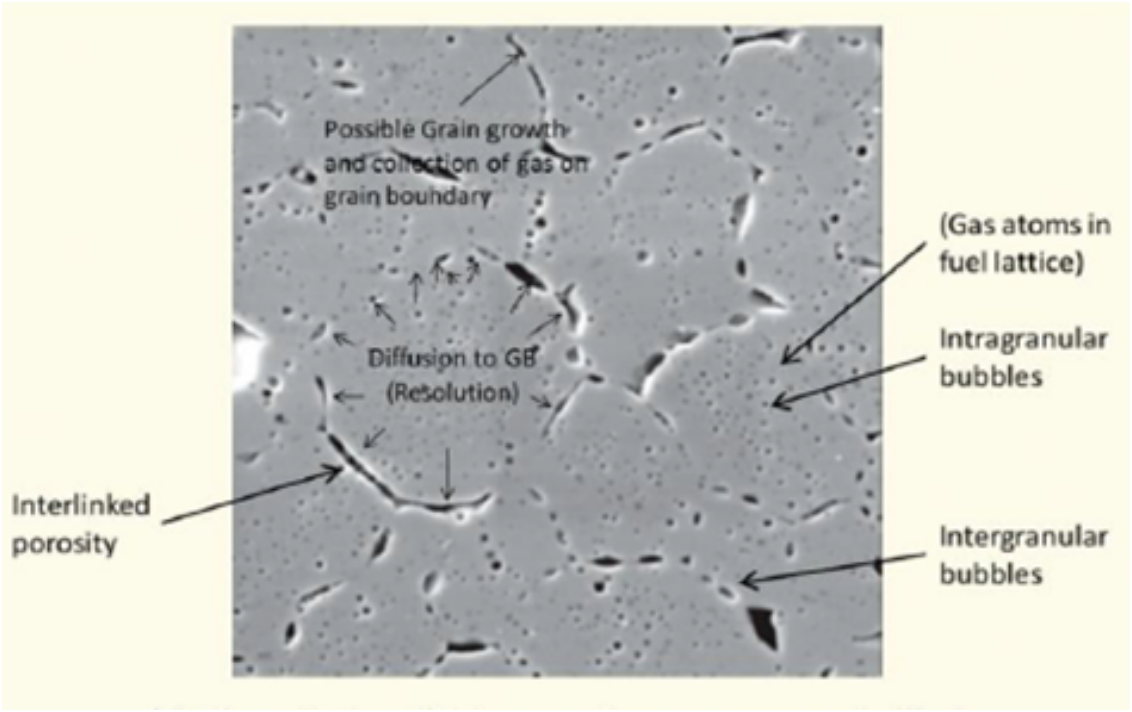

Figure 40 Micrography in which the different processes can be observed [17]

5.2. TRANSURANUS fission gas release for thorium fuels

The release of fission gases in TRANSURANUS is treated by embedding the mechanisms previously mentioned into the process: athermal release, intra-granular diffusion, inter-granular diffusion, grain boundary sweeping and HBS. For a TRANSURANUS thorium fission gas release version, only the first three are going to be accounted for, since the research work for grain boundary sweeping and HBS has not been performed yet.

Unfortunately, in the open literature there are fewer data about fission gas experiments in thorium fuels. The earliest measurements of fission gas release on irradiated ThO_2 and $(Th,U)O_2$ fuel rods from Shippingport Power Station were done at the BAPL (Bettis Atomic Power Laboratory) [105, 106] and INEEL (Idaho National Engineering and Environmental Laboratory) [21]. In Japan, the JAERI (Japan Atomic Energy Research Institute) carried out experiments on irradiated fuel for cesium release [94, 107] and for iodine and tellurium [108]. Other experiments based on the SIMFUEL (Simulated Fuel) technique were carried out to simulate the diffusion of fission gas fragments through the fuel. The SIMFUEL technique consists basically in doping with fission products which a certain concentration which was previously simulated in a fuel pellet and then heat it up with an annealing history [34, 109, 110]. Then, these samples are punctured in a facility and the gas is then collected. With these gas concentrations obtained from different pellets annealed with different histories, the fission gas rate (Equation 5.5) can be inferred. Most recently, fission gas release rates were analysed from two different $(Th,Pu)O_2$ rodlets irradiated at KWO for the Thorium Cycle [2]

and SCK•CEN for OMICO project [32, 31] respectively.

5.2.1. Athermal model in TRANSURANUS

Although the a-thermal contribution to the overall release rate is around 1%, TRANSURANUS accounts this mechanism by employing Turnbull's empirical model [111]:

$$f_{ath} = a \cdot bu \tag{5.2}$$

where f_{ath} is the fractional fission gas release rate, bu is the burn-up expressed in MWd/kg HM and a is a fitting constant that has the value of 6.1705 $\times$ 10^{-5} kg HM/MWd. The extension of this model lays on the modification of a by inserting an if-statement. For thorium-based fuels, this parameter takes the value of 2.2733 $\times$ 10^{-8}.

5.2.2. The Speight model and its extension for intra-granular processes

An early intra-granular model was developed by Booth [112] in which the diffusion equation for a single gas is solved in a spherical-form grain with a null concentration in the grain boundary as boundary condition. Das [34] pointed out that the limitations of this model relay on the calculation of the radius of Booth's sphere and the neglect of the mechanisms trapping and irradiation-induced resolution. Those mechanisms strongly influence on the release of fission gases to the free volume by delaying or enhancing the diffusion of gas atoms from the grain to the grain boundary. The Speight model [113] (Equation 5.3) improves the Booth's intra-granular diffusion of fission gas model during irradiation by stating a single diffusion equation with an effective single atom diffusion coefficient that accounts for the trapping and irradiation induced re-solution (Equation 5.4), rather than solving another equation for these phenomena separately. This model omits the mobility of gas bubbles. Therefore, this model underpredicts fission gas release at high temperatures or power transition conditions [114, 113, 115]. A mechanistic extension proposed by Van Uffelen [114] and Pastore [99] consider the mobility of gas bubbles to the grain boundaries by volume diffusion (see Appendix B).

$$\frac{\partial C_t(r,t)}{\partial t} = lap\left[D_{eff}(t) C_t(r,t)\right] + \beta(t) \tag{5.3}$$

$$D_{eff}(t) = \left[D_s(t)\frac{b(t)}{b(t)+g(t)} + D_b(t)\frac{g(t)}{b(t)+g(t)}\right] \tag{5.4}$$

$C_t(r,t)$ defines the total concentration in the grain as the sum of the gas concentration solved in the material, $C_s(r,t)$ and trapped in bubbles within the grain $C_b(r,t)$. β is the source term and represents the gas atom generation. $g(t)$ is the probability per unit time of gas atoms in solution being captured by a bubble while $b(t)$ is the probability per unit time when a gas atom in a bubble is re-dissolved. D_s and D_b are the single diffusion atom and bubble diffusion coefficient respectively. The variables r and t are the co-ordinate of the spherical grain and the time respectively.

Under reactor conditions D_{eff} and β are functions that depend on the time due to different

power histories. This makes the solution of Equation 5.3 more difficult. The set of algorithms developed to solve that equation is considerable, from the ANS-5.4 algorithm [116], which gives an accurate solution, but with a great time computer consumption, to the algorithm of Väth, or the direct solution proposed in the FEMAXI [18] code, or the recent method developed by Lösönen [117]. The most used algorithms in TRANSURANUS are FORMAS [118, 119], URGAS [115, 120] and the recent PolyPole-1 [121]. Finally, the fission gas release rate is defined as:

$$f(t) = 1 - \frac{\overline{c}_t(t)}{\overline{c}_{created}(t)} \tag{5.5}$$

where $\overline{c}_{created}(t)$ is spherical averaged concentration of gases created by fission and $\overline{c}_t(t)$ is the averaged concentration of gases within the grains once Equation 5.3 is solved and then volume averaged as follows:

$$\overline{c}_t(t) = \frac{\int_0^a C_t(r,t) 4\pi r^2 dr}{\frac{4}{3}\pi a^3} \tag{5.6}$$

being a the radius of the sphere that represents the grain.

Following the expression of the diffusion coefficient in Equation 5.1 the pre-exponential term, D_0 and the barrier energy, ΔH must be determined. To this end, able 14 summarizes the diffusion pre-exponential term and the barrier energy found in the literature. White and Tucker [98] postulated that the largest discrepancies between experiments and the simulations are in the diffusion coefficient. Van Uffelen [114] also points out the single gas diffusion coefficient as the major discrepancy of about one order of magnitude when the improved Speight model was compared to experimental data from a power ramp and a power cycle for UO_2. Pastore [99] summarises the work of several authors who conclude that there are two orders of magnitude of uncertainty for the single gas diffusion.

In Table 14 the effective diffusion coefficients found in the literature are listed as well as their sources and temperature ranges of validity in Figure 41 and their comparison to the experimental data points obtained by Kim [109]. Naik [34] doped pellets of (Th,1%U)O_2 with Xe and irradiated them up to different but low burn-ups. Then the fission gas release was extracted and through Booth's solution (see Equation 5.7), for low burn-up the diffusion constant was calculated. Also Kim [109] used this approach to measure the three data points at three different temperatures in cubes of polycrystalline and SIMFUEL (Th,U)O_2, with an initial porosity of 3% and a grain sizes between 7.5 and 10.0 μm irradiated up to 0.1 MWd/kg HM. The cubes were irradiated between 20 and 30 minutes and then annealed at 1400, 1500 and 1600°C. The correlation derived by Naik was rejected due to the large grain size of the pellets, 35-45 μm, and to the initial porosity of 10% in the experiments, which is uncommon for LWR fuels.

Shiba [94] carried out experiments about the release of Xe from (Th,U)O_2 pellets that were irradiated at low temperature with a very low dose (2.9 $\times$ 10^{19} - 2.2 $\times$ 10^{22} fissions m^{-3}) and then annealed at a temperature of 1000 K for a short period of time. The post-irradiation

release showed that the rate was low.

Shirsat [110] set up some experiments of doped (Th,U)O_2 pellets irradiated up to 2% at burn-up, resulting in a higher release of Xe. The doping of the pellets by Xe and other volatile compounds created more trivacancies that enhanced the diffusion, and finally, the fractional release rate of Xe during annealing:

$$f = \sqrt{\frac{36Dt}{\pi a^2}} \tag{5.7}$$

D_0 (m^2 s^{-1})	ΔH (kJ mol^{-1})	Reference
20×10^{-11}	189	Shirsat [110]
1.4×10^{-12}	239	Naik [122, 34]
4.5×10^{-15}	239	Naik [122, 34]
5.3×10^{-13}	289	Naik [122, 34]
2.6×10^{-5}	478	Shiba [123, 34]
7.1×10^{-11}	344	Shiba [123, 34]
10.57×10^{-17}	79.05	Long [124]
1.5×10^{-10}	189	Shirsat [125, 34]

Table 14 Review of the pre-exponential and the enthalpy terms to calculate the effective diffusion coefficient for the intra-granular model

As can be seen in Figure 41 all the diffusion constants have similar slopes except for Long's recommendation [124]. Although Long's activation energy is the lowest, his diffusion coefficient is the only one that matches the experimental data point of Kim [109] at 1400°C. Long proposed that the diffusion coefficient for Th is ten times lower than U and he validated this statement by comparing the fission gas release rate measured in pellets irradiated up to 65 MWd/kg HM at BPNWL (Batelle Pacific North-West Laboratories) to his results obtained by adapting the diffusion coefficient to the FORMAS algorithm in FRAPCON. Long also suggested a diffusion coefficient for higher temperatures (T$>$1500 K). However, it is not implemented in TRANSURANUS due to the dependence of the pre-exponential term on the porosity [124]. Moreover, normal operation conditions are commonly lower than 1500 K. Shiba [94] and Shirsat [110] correlations were thus rejected due to the low burn-up at which their experiments were performed.

$$D\left[\frac{m^2}{s}\right] = 10.5710^{-17} \times e^{-\frac{9508}{T}} \tag{5.8}$$

T is in Kelvin.

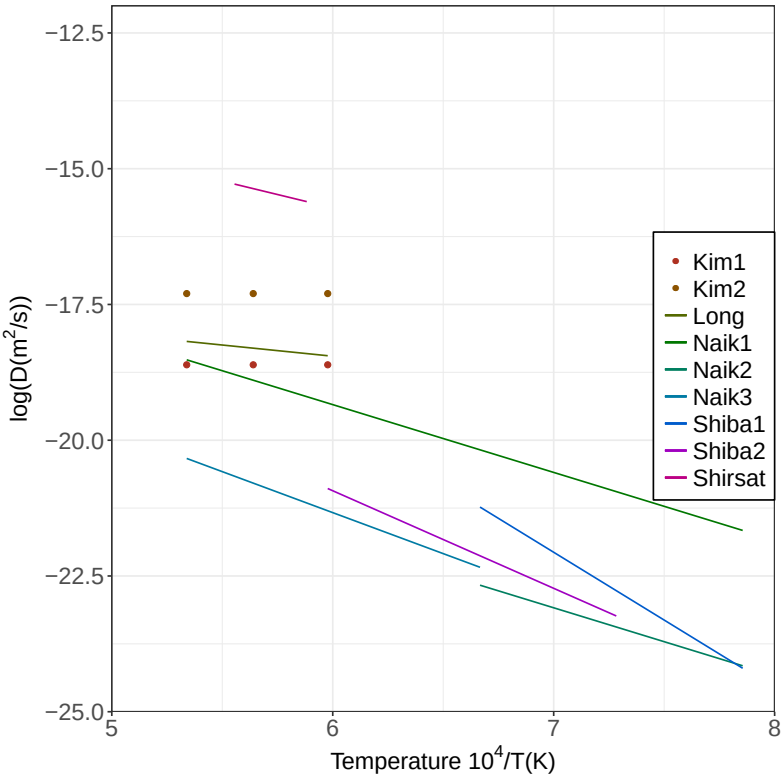

Figure 41 Graphical comparison of the founded effective diffusion coefficients for the intra-granular model

White and Tucker [98] postulated that the largest discrepancies between experiments and the simulations are in the diffusion coefficient. Van Uffelen [114] also points out the single gas diffusion coefficient as the major discrepancy of about one order of magnitude when the improved Speight model was compared to experimental data from a power ramp and a power cycle for UO_2. Pastore [99] summarises the work of several authors who conclude that there are two orders of magnitude of uncertainty for the single gas diffusion. In general, the scatter in these data is extremely large and can probably be partly attributed to differences in sample type (powder, doped samples, etc.) or burnup (i.e. presence of bubbles that operate as trapping centres or not).

5.2.3. The simplified inter-granular model

For the inter-granular process two models can be chosen in TRANSURANUS: a simplified model proposed by Dowling [126] and a mechanistic or physic-based described by Pastore [99] in the frame of his Ph.D. The simplified model assumes, through observations performed by Dowling [126], that the grain boundary area is occupied by a fraction of 50-60% of fission gas grain boundary bubbles. It is thus reasonable to say that the boundaries are saturated by gas atoms and, when the concentration of fission gas at grain boundaries reaches this saturated concentration, the gas is immediately released.

The mechanistic model takes into account the growth of the bubbles by collecting fission gases and vacancies. The coalescence, among them, produces larger but fewer bubbles through their interconnection at the grain boundaries or edges until the release of fission gas to the free surface eventually occurs. This model was not assessed for thorium-based fuels due to the limited information available for this type of fuels concerning grain growth and other phenomena considered in Pastore's model during irradiation.

Dowling [126] and White [98] introduced the concept of grain boundary saturation. When gas atoms born in the bulk move to the grain boundaries, either in the form of gas bubbles or dissolved in the matrix, two main processes can happen. In first place, the possibility of the transport of these gas atoms back to the grain is due to re-solution. Secondly, the accumulation of these gas atoms as grain boundary bubbles, that can entail the coalescence and form a tunnel network where the gases are release to cracks, and finally to the free volume. The simulation of the formation of these tunnels implies the calculation of a certain concentration of gas atom in the grain boundary from which the gases are diffused out.

The volume of a lenticular bubble that is trapped in the grain boundary is approximated by a sphere:

$$V_{bubble} = \frac{4}{3}\pi r_f^3 f_f(\vartheta) \tag{5.9}$$

$$f_f(\vartheta) = 1 - \frac{3}{2}\cos(\vartheta) + \frac{1}{2}\cos^3(\vartheta) \tag{5.10}$$

where r_f is the radius of curvature of the capillary surface of the bubble, $f_f(\vartheta)$ relates the volume of the lens to that of the complete sphere. 2ϑ is the dihedral angle between bubble surface and grain boundary, and it is calculated according to [98] as follows:

$$2\vartheta = \arccos\left(\frac{\gamma_{gb}}{2\gamma_{fs}}\right) \tag{5.11}$$

γ_{gb} and γ_{fs} stand for the grain boundary and the free surface energies respectively.

The internal pressure of a bubble under hydrostatic forces is calculated by solving the balance of these mentioned pressures with the surface tension, (for further details of this approach, see [127])

$$P_{gas} - P_{ext} = \frac{2\gamma}{r_f} \tag{5.12}$$

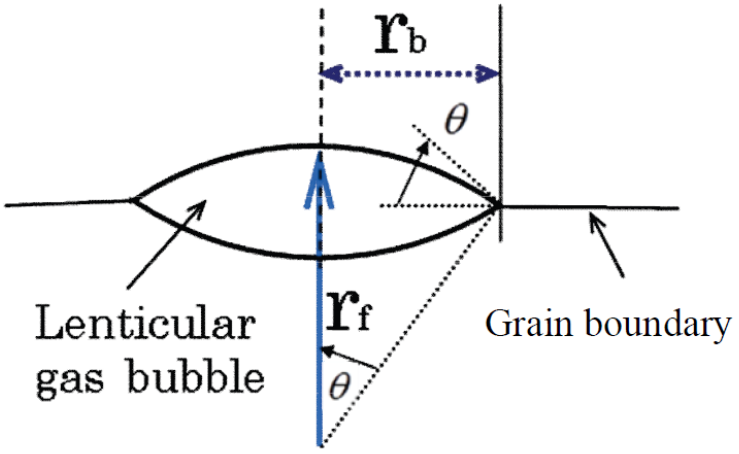

Figure 42 Representation of a lenticular bubble [18]

The gas atom density is defined by the number of gas atoms in the bubble, m, divided by the area which the bubble occupies in the boundary $r_f \sin(\vartheta)$ [18]

$$N_f = \frac{m}{\pi(r_f \sin(\vartheta))^2} \tag{5.13}$$

If the gases within the bubble behave as ideal gases, m may be further developed:

$$N_f = \frac{m}{\pi(r_f \sin(\vartheta))^2} = \frac{V_{bubble} P_{gas}}{kT\pi(r_f \sin(\vartheta))^2} \tag{5.14}$$

Now, introducing Equation 5.12 and Equation 5.9 into Equation 5.14, the following form is obtained:

$$N_f = \frac{4 r_f f_f(\vartheta)}{3kT \sin^2(\vartheta)} \left(P_{ext} + \frac{2\gamma}{r_f} \right) \tag{5.15}$$

Assuming that f_b is the covering fraction of lenticular bubbles on the grain boundary surface, the threshold, or upper limit, N_f^{sat} considered as an estimate for the total grain boundary area is

$$N_f^{sat} = N_f f_b = \frac{4 r_f f_f(\vartheta)}{3kT \sin^2(\vartheta)} f_b \left(P_{ext} + \frac{2\gamma}{r_f} \right) \tag{5.16}$$

The units of the saturated concentration are atoms/cm^2, f_b according to [126] takes the value of 0.5 and the surface tension 0.5 J/m^2. Equation 5.16 can be simplified by setting P_{ext} equal to zero. The assumption of ideal behaviour of the fission gases within the bubbles is oversimplified according to Das [34], and the application of the Van der Waals equation for the gases is more reasonable, due to the high pressures to which the the gas atoms inside the bubbles are subjected.

	ThO_2	UO_2
γ_{gb} (J/m^2)	0.3	0.3
γ_{fs} (J/m^2)	0.81	1.03
ϑ	40.68°	39.66°

Table 15 Comparison of γ_{gb}, γ_{fs} and ϑ between ThO_2 and UO_2

Table 15 lists the values of the parameters γ_{gb} and γ_{fs} found in the literature, which are needed to calculate the dihedral angle, ϑ according to Equation 5.11.

Benson [128] derived the surface energy (γ_{fs}) for ThO_2 and UO_2 through two theoretical methods. He employed the Watchman's quadratic relation, instead of Born-Haber cycle due to its inaccuracy in the data. The value derived for ThO_2 was 0.81 J/m^2. Blair [92] proposed the value of 1 J/m^2 for UO_2, which matches the value derived by Benson (1.03 J/m^2) by using the Born-Haber cycle. This value also coincides with the values proposed by Maiya [129] and Koo [130].

Olander [3] estimated the value of 0.3 J/m^2 of the grain boundary energy for UO_2. This value is also similar to that calculated by Maiya [129]. Unfortunately there is no value for ThO_2, so as a first approximation the UO_2 value was taken.

The values of the dihedral angle calculated with Equation 5.11 are 40.68° and 39.66° for ThO_2 and UO_2 respectively. However, the value used in TRANSURANUS for UO_2 is approximated to 50°. Taking into account the large uncertainty in the data and the similar values obtained for ThO_2 and UO_2, it is reasonable to adopt the value of 50° for the dihedral angle in ThO_2 as well. As a consequence, no modification was introduced for the the saturation concentration for grain boundary in TRANSURANUS for thorium-based fuels.

6

Thorium Cycle

The 5^{th} EC Framework Programme funded the project Thorium Cycle that consisted on the irradiation of a (Th,Pu)O_2 test fuel rod [19] in a PWR. The KWO was a a 2 loop PWR located near the town of Obrigheim in the southwest of Germany that begun its operation in April 1, 1969, generating a 357 MW gross electrical output for a reactor thermal power of 1050 MW [2]. The 97 fuel assemblies in the core were cooled by a coolant volume flow of 9.0458 m^3/s with an average coolant temperature of $297°$C.

The test fuel rod was manufactured at JRC-ITU in September 1986 through a sol-gel technique [2] with the initial plutonium isotopic vector shown in Table 16. In mid 2001, in cycle 32 of the reactor, the rodlet was inserted for irradiation, which lasted a total of four cycles until 2005.

^{238}**Pu**	^{239}**Pu**	^{240}**Pu**	^{241}**Pu**	^{242}**Pu**	^{241}**Am**
0.02	91.36	8.28	0.30	0.04	0.51

Table 16 Plutonium and Americium composition (% w/o) of the rodlet in 1986 [19]

The plutonium isotopic content varied from when the rodlet was fabricated in 1986 until it was loaded in the core in 2001 because the half life of ^{241}Pu, which is 14.33 years. Hence, the concentration of this nuclide was reduced. The updated initial content of the homogeneous ThO_2-PuO_2 segment, having considered this issue, is listed in Table 17.

^{232}**Th**	^{238}**Pu**	^{239}**Pu**	^{240}**Pu**	^{241}**Pu**	^{242}**Pu**	^{241}**Am**
96.705	0.001	2.995	0.271	0.005	0.001	0.022

Table 17 Updated initial isotopic concentration (% w/o) of the rodlet before being inserted in the reactor in 2001 [19]

The initial specifications of the (Th,Pu)O_2 segment are shown in Table 18. The rodlet consisted of 17 pellets with an average pellet length of 8.6 mm. The stack of pellets was introduced in a Zircaloy duplex cladding tube [2] with an active total length of 206 mm [19]. On the upper part of the segment there was a chamber that contained a spring of nominal length of 47 mm to mitigate the axial rod deformation.

Number of pellets	17
Active Length	146.5 mm
Pellet diameter	8.05 mm
Cladding inner diameter	8.22 mm
Cladding outer diameter	9.5 mm
Sintering porosity	5%
Average density	10.05 g/cm^3
Fuel rod pitch	12.6 mm
MOX rod active length	3650 mm

Table 18 Initial specification of the rodlet [19, 27, 28, 26]

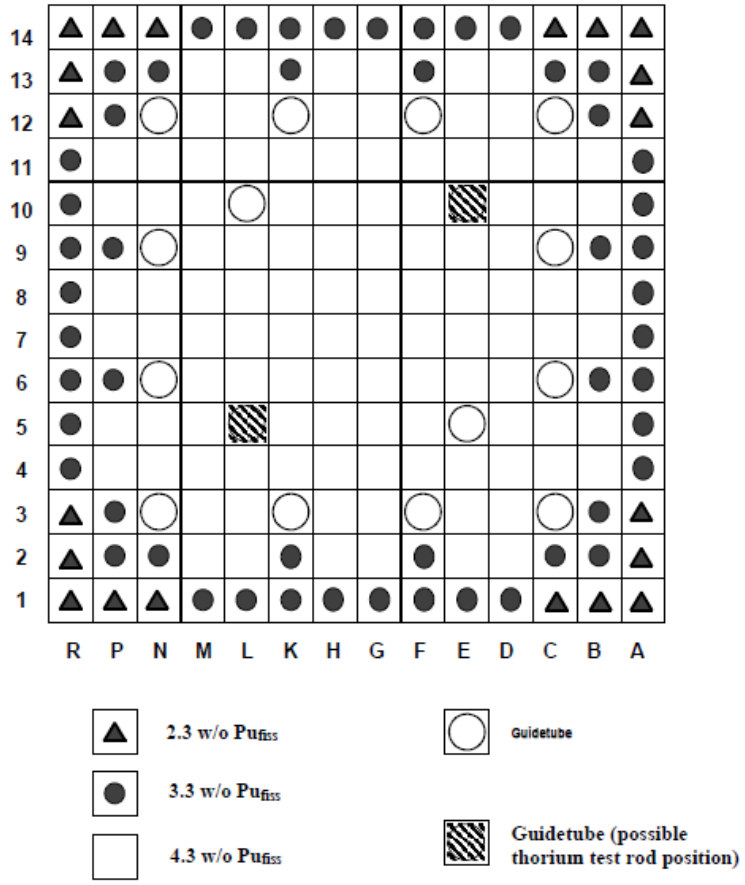

Figure 43 Representation of the carrier assemblies MOX2310-12 where the (Th,Pu)O_2 test fuel rod was placed [19]

The non-occupied volume of this chamber, known as upper plenum volume where the fission gases are collected, was 1.5 cm^3, while in the lower part of the segment there was no lower plenum volume. The rodlet was filled with helium to have an internal pressure of 22 bar at 25°C. Finally, the average external roughness of the pellets was 0.906 μm and the porosity 5%.

The position of the segment within the assembly was intentionally selected in one of the four central positions of the guide tube in order to mitigate the possible impact of this thorium probe on the neutron flux in adjacent assemblies.

The depth of the insertion was 858 mm from the top of the active MOX fuel length to the middle of the active part of the thorium rod. At this length a flat linear power rate in the whole thorium segment was achieved, thus, avoiding possible power gradients (Figure 44).

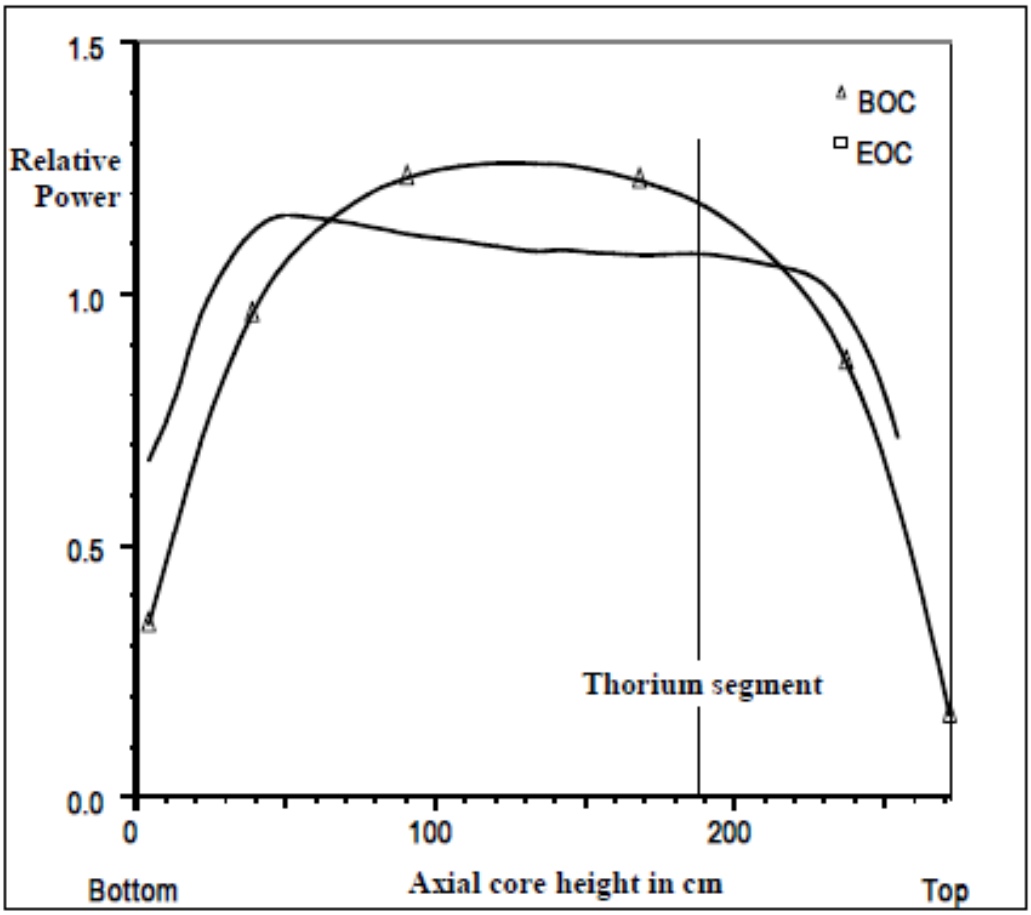

Figure 44 Axial position of the thorium probe in the reactor [19]

In the first cycle of the test rodlet, that corresponded to the cycle 32 of the reactor, the thorium

rodlet was placed in the 14x14 central MOX carrier assembly MOX23-10 in the position (E10) of a non-instrumented guide tube as displayed in Figure 43. This first cycle had a length of 340 efpds (effective full power days) in which the local linear heat generation in the rodlet was 194 W/cm [19, 2], with final burn-up attained of 12.4 MWd/kg HM. In the second cycle, that corresponded to KWO cycle number 33, the local linear heat rate was 143 W/cm with a burn-up of 9.2 MWd/kg HM. The cycle was programmed to last 326 efpds but due to shut-down reparation and revisions was stretched out to 340 efpds.

In the third cycle (34 KWO cycle) the rodlet was transferred to MOX carrier assembly MOX23-12 in the guide tube position L05 achieving during this cycle a burn-up of 9.9 MWd/kg HM with a local linear heat generation of 155 W/cm. The length of this cycle was in total 387 efpds after a 58 stretch-out due to power reductions. The fourth and last cycle of the test rod, corresponding to the last cycle of KWO, was characterised by the burn fuel assembly reloaded in the reactor [2, 19]. This last cycle lasted 106 efpds followed by a stretch-out operation of 68 days with an accumulated burn-up attained in the Th-MOX test rod of 7.3 MWd/kg HM and the lowest local linear heat rate of 155 W/cm. The final average burn-up achieved in the rodlet was 37.7 MWd/kg HM, fulfilling the planned targets.

6.1. Assessment of the Thorium Cycle pin

Two 2-D parallel Serpent simulations were performed that represented the full assembly where the thorium rodlet was placed. In one simulation the pellet was divided into ten equi-volume rings whereas, in the second simulation the pellet was not divided. The reason behind this approach was the derivation of the radial power functions for the nuclides ^{232}Th and ^{240}Pu 4.2.1 and their volume normalisation with the non-divided pellet outputs. As can be appreciated in the output Figure 45 generated by Serpent, the two input files were simplified from the original experiment [28, 26] in these three main features:

1. The transfer of the segment from the carrier assembly MOX23-10 to MOX23-12 between the cycles 33 and 34 as well as its intermediate shut down, were both neglected
2. The total Pu concentrations in the adjacent MOX rods (2.3, 3.3 and 4.3 wt.%) were assumed to be the same as in the thorium-based rodlet (Table 17)
3. The guide tube containing the thorium rod was not included as its influence on the neutron flux could also be dismissed

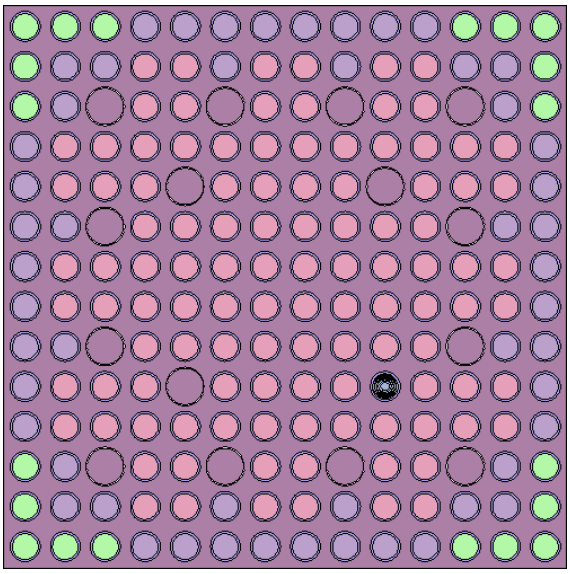

Figure 45 Representation of the input geometry of the carrier assembly and thorium rodlet in Serpent

6.1.1. Normalised radial power generation profile

Figures 46a and 46b compare the normalised power densities for a low burn-up of 1 MWd/kg HM and a final burn-up of 38.8 MWd/kg HM, at which the sample from the rodlet was irradiated, to the simulations of Serpent and TUBRNP. In the low burn-up Figure 46a a simulation carried out as part of the Thorium Cycle was also added [19] to extend the comparison. In both figures, the good agreements between Serpent, the simulation from Thorium Cycle and the TUBRNP version for (Th,Pu)O_2 are depicted.

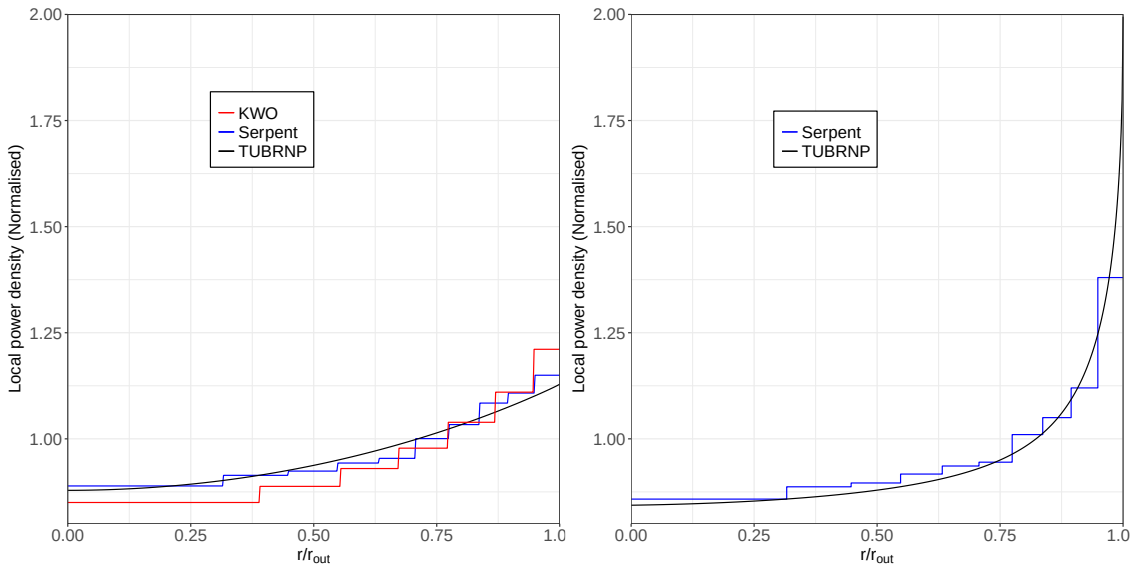

(a) Low Burn-up

(b) Final Burn-up

Figure 46 Simulated local power density

6.1.2. Radial profile concentrations comparison

The first step for the validation of the TUBRNP version for thorium-based fuels relies on the comparison to experimental data of the calculated concentrations as a function of the pellet radius of the most relevant nuclides involved in the thorium fuel cycle as well as the main fission products. For (Th,Pu)O_2 fuels the validation was done in two parts. Normalised radial concentrations of the elements Th, Pu, U, Nd, Xe and Cs predicted with TUBRNP and Serpent were compared to the experimental data points measured on a sample irradiated in KWO by EPMA (for further details about this method see [131]). EPMA measurements on a 7 mm thick sample, KWO-Th-Pu-14, between pellets 11 and 12 with a local burn-up of 38.8 MWd/kg HM were carried out as part of the LWR Deputy programme, which is a continuation of the Thorium Cycle project [44], and offered for assessment in the context of an international benchmark. The higher burn-up located in this area is attributed to the fact that at both extremes of the 146 mm length segment, the rodlet was more cooled and therefore more fissions may have occurred at both positions, with the resulted in an increment of the burn-up.

Figures 47 to 52 show the agreement between TUBRNP, Serpent and EPMA data regarding the distribution of those elements along the pellet radius. These figures enable an assessment on the analytical derivation of the radial shape functions described in 4.2.1, especially in the cases of U (Figure 48) and Nd (Figure 50) where the agreement is even better due to the low scatter of the EPMA points.

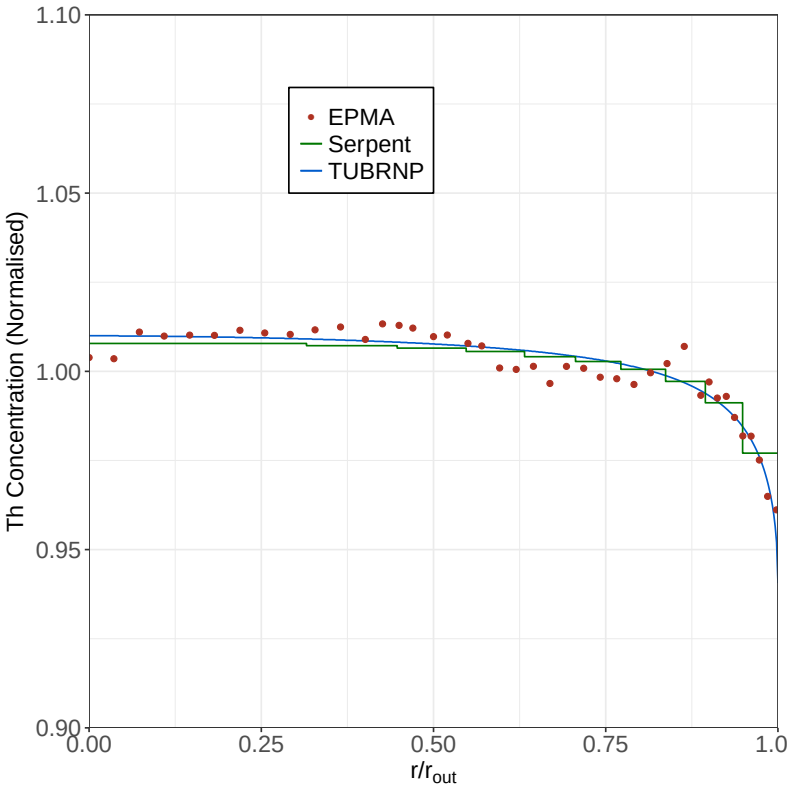

Figure 47 Comparison between measured (EPMA) and simulated Transuranus and Serpent normalised radial distribution of Th

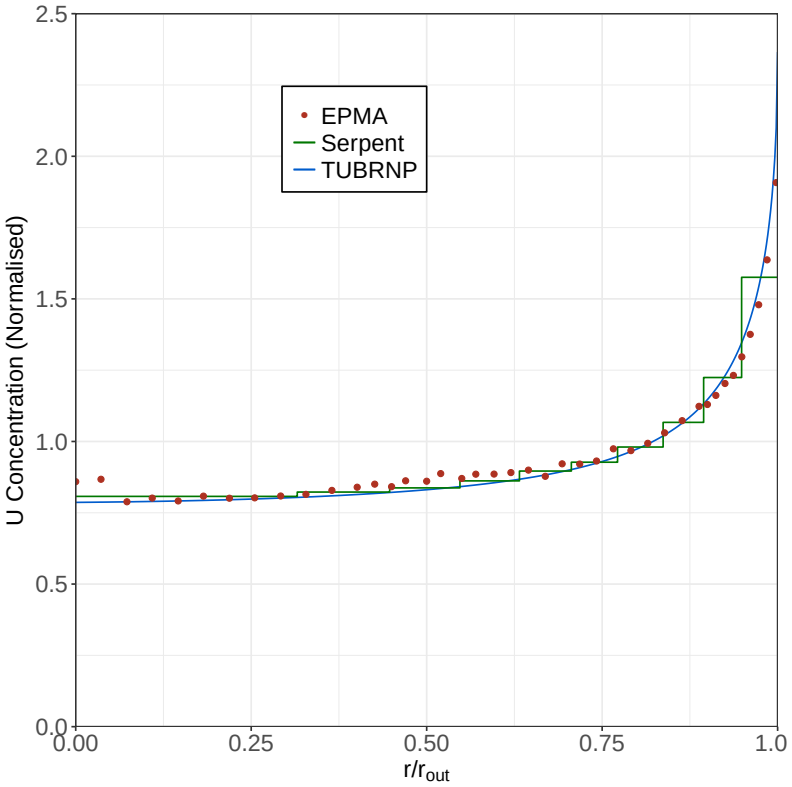

Figure 48 Comparison between measured (EPMA) and simulated Transuranus and Serpent normalised radial distribution of U

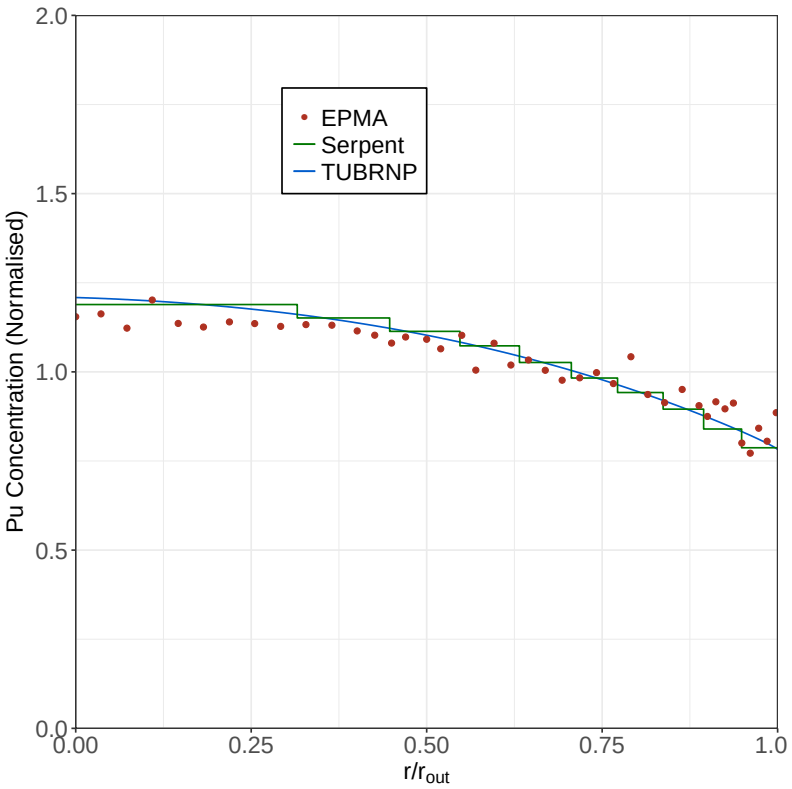

Figure 49 Comparison between measured (EPMA) and simulated Transuranus and Serpent normalised radial distribution of Pu

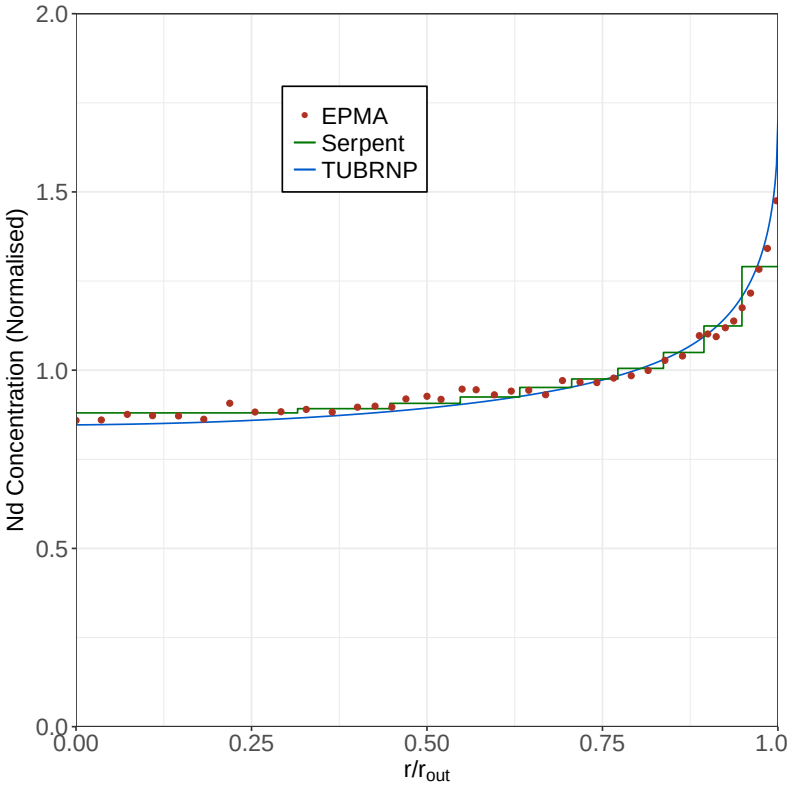

Figure 50 Comparison between measured (EPMA) and simulated Transuranus and Serpent normalised radial distribution of Nd

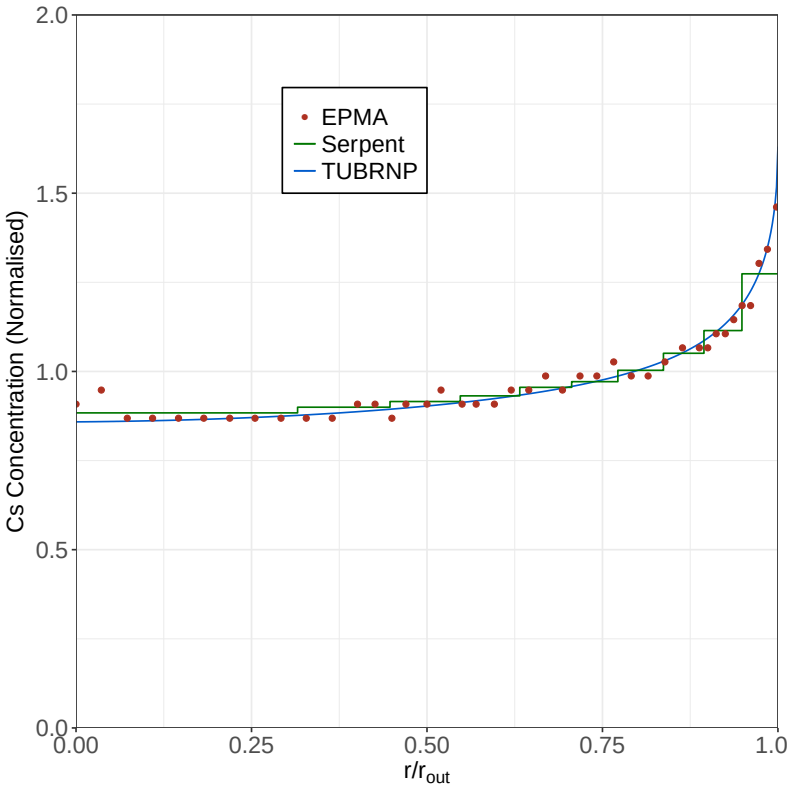

Figure 51 Comparison between measured (EPMA) and simulated Transuranus and Serpent normalised radial distribution of Cs

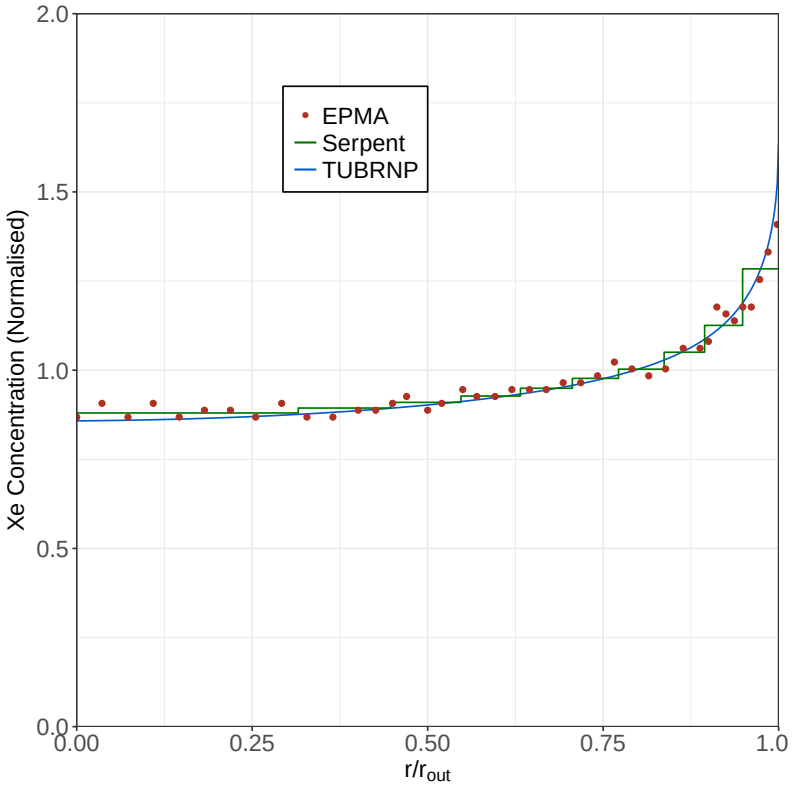

Figure 52 Comparison between measured (EPMA) and simulated Transuranus and Serpent normalised radial distribution of Xe

The second part of the validation is done by comparing the radial averaged concentrations of the previously mentioned elements of TUBRNP and Serpent to EPMA observations performed on the sample KWO-Th-Pu-14.

The analysis is completed by taking the results of a benchmark as part of the Thorium Cycle project [27] into account. The codes used in this benchmark were:

1. the interface MCBurns that coupled MCNP 5.15 with the depletion burn-up code ORIGEN 2.2,
2. the neutron trasnport code Helios-1.10 [132],
3. the 2D lattice physics code Casmo-5,
4. the interface EET that couples the multi-group cell code ECCO/ERANOS with the burn-up code TRAIN

There are two important issues that made this benchmark different from the Serpent and TUBRNP simulations. Firstly, the guide tube and the intermediate programmed shutdown of the reactor were both included in the benchmark. Secondly, the final burn-ups of the four codes were calibrated to the concentration of ^{137}Cs measured in another sample of the probe [27]. The final burn-ups of the four codes ranged between 36 and 39 MWd/kg HM [27].

The utilization of the ^{137}Cs concentration as burn-up monitor is questionable, as ^{137}Cs is a volatile element that can be released [133] and its half-life is 30.17 years. The concentration of ^{137}Cs dissolved in the fuel matrix as consequence of the fission events may therefore be underestimated. Nowadays Nd is normally used a so-called burn-up indicator [39].

	Th	U	Pu	Nd	Cs	Xe
EPMA [44]	79.77	1.35	0.71	0.38	0.25	0.52
TUBRNP [28, 26]	81.96	1.77	0.66	0.36	0.27	0.56
Serpent [28, 26]	81.84	1.75	0.68	0.34	0.13	0.51
MCBurns [27]	81.66	1.91	0.89	0.32		
Helios [27]	82.05	1.65	0.85	0.31		
Casmo [27]	82.02	1.54	0.79	0.33		
EET [27]	81.80	1.79	0.84	0.33		

Table 19 Measured and calculated total (radially averaged) element concentrations (in wt.% Fuel)

Tab. 19 compares the code predictions to the EPMA measurements. For Th, all the applied codes present a slight overestimation that does not exceed 3% relative difference, which is within the limits of approximately 10% uncertainty of the EPMA technique [40, 131]. For U, the results present the largest relative differences between 13% (Casmo) and 40% (MCBurns). A possible explanation may be the uncertainty in the radiative capture reaction in ^{232}Th. Moreover, as Th is the most abundant element in the sample, its concentrations predicted by the six codes are subject to the largest absolute scatter. This could affect the breeding of U. Another reason of this deviation may be attributed to the fission rate, but this can not be proven as most of the fission products may come from the fission in Pu. The presence of this element in the fuel has considerably been reduced from its initial concentration during the irradiation. In this case, TUBRNP shows for Pu a disagreement of 8% that is below the uncertainty level of EPMA. This proves the accuracy of implementing burn-up-dependent cross sections in ^{239}Pu, ^{240}Pu and ^{241}Pu.

Despite the difference in U, the agreement of the simulated actinide concentrations is acceptable, as the above irradiation experiment is the only available so far for the validation of this first version of TUBRNP for (Th,Pu)O_2.

Regarding the simulated fission products, the Nd results show good agreement for all six codes. The prediction of Cs obtained with Serpent displays the largest discrepancy (50%) among all the values studied, whereas TUBRNP shows satisfactory results for Cs. On the other hand, the estimation of Xe is more accurate in Serpent than in TUBRNP. Unfortunately, no analysis of Cs and Xe was made for the other codes in the benchmark [27].

It is also important to note that TUBRNP solves the Bateman equations by transforming the derivatives into increments while the other codes described in this section apply more complex numerical methods. For example, Serpent makes use of the CRAM (Chebyshev rational approximation method) in order to compute the exponential matrix in the analytical solution of the depletion equations, with the disadvantage of longer computation times [134, 135].

7

Oxide Fuels: Microstructure and Composition Variations

The 5^{th} Framework Oxide Fuels Microstructure and Composition Variations or OMICO project was a programme sponsored by the European Union that consisted in the preparation of samples of UO_2 (U,Pu)O_2 and (Th,Pu)O_2 and their irradiation at the beryllium-moderated experimental reactor BR-2 at the SCK•CEN in Mol, Belgium. The 6^{th} LWR Deputy programme was an extension of the previous programme and consisted in the performance of post-irradiation experiments carried out not only on OMICO samples, but also on the rodlet from the Thorium Cycle at several research centers like JRC-ITU in Karlsruhe, Germany or PSI (Paul Scherr Institute) in Switzerland [32].

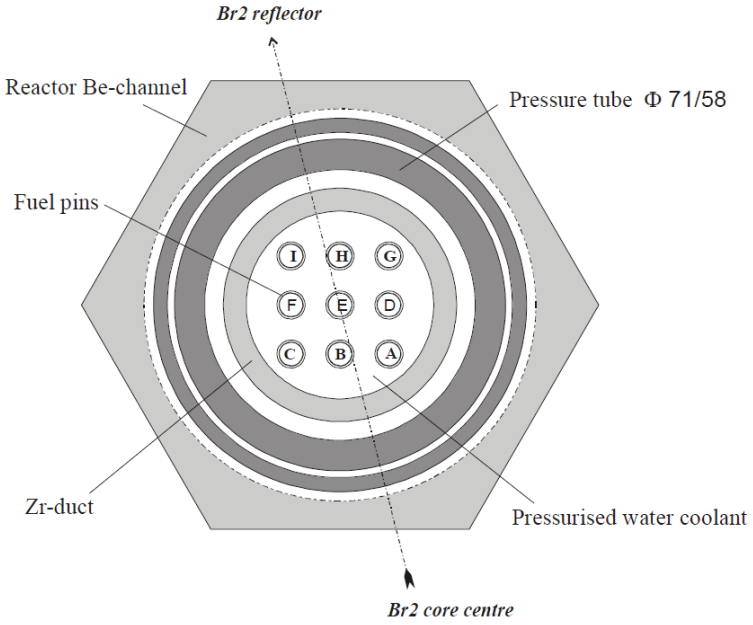

Figure 53 Radial distribution within the assembly of the OMICO rods. The (Th,Pu)O_2 rods were places in batches B and H [20]

The objective of the programme was the analysis and the comparison of the performance of similar fuel but with different microstructures. Three homogeneous fuel rods of UO_2, (Th,Pu)O_2 and (U,Pu)O_2 were manufactured by means of sol-gel technique [2]. These rods occupied the positions A, B and G (see Figure 53) in the test assembly. By using the MIMAS process [32], heterogeneous fuel rods set in positions C and I were fabricated for the fuel types UO_2 and (U,Pu)O_2 respectively. The heterogeneous (Th,Pu)O_2 fuel rod placed in lo-

cation H was prepared through the sol-mas technique. The sol-mas process differs from the sol-gel technique in the utilization in first place, of (Th,Pu)O_2 particles that were then blended with ThO_2 before being pelletised and sintered [31, 32]. Two rods of each type of fuel and microstructured were produced. In the instrumented rods (with subscript i) part of the probe was formed with annular pellets in order to incorporate a thermocouple to measure the centre temperature on-line while in the non-instrumented rods (with subscript n) the stack was composed of full pellets.

The test assembly was loaded in the reactor in 2004 in the pressurized water loop CALLISTO in order to start its irradiation until 2006 (2004/5, 2005/1, 2005/2a, 2005/2b, 2005/3, 2005/4b, 2006/3 and 2006/4)) completing 8 cycles in total. During the first cycle (2004/5), a driver fuel element was inserted in the adjacent position to the OMICO rod, whereas for the rest of the cycles no rod driver was positioned, except during the last cycle in which another two driver assemblies were positioned next to the test IPS assembly. After the fourth cycle (2005/2b) the heterogeneous UO_2 rod C was substituted by a dummy zircaloy bar of same dimensions due to rod failure. The instrumented rods were only irradiated until cycle 6 (2005/4b) since another clad failure occurred in one of the remaining probes during cycle 6. Consequently all the rods were removed from reactor. The reactor was operated at nominal power (60 MW_{th}) for all the cycles. However, the reactor was constrained to 82 % and 92 % of its nominal power during cycle 2004/5 for several days [32].

During the irradiation the central temperature in the instrumented rod was recorded. After the irradiation, PIE were carried out to measure the gap size between the cladding and the fuel pellet. The (U,Pu)O_2 and (Th,Pu)O_2 non-instrumented rods were further irradiated as part of the extension of OMICO programme, THOMOX in order to attain higher burn-up (around 37 MWd/kg HM) and perform a fission gas release analysis on them [31].

7.1. Simulation of the OMICO programme in TRANSURANUS

The validation of the full TRANSURANUS version for (Th,Pu)O_2 was done by comparing the on-line centre temperature recorded in the instrumented rods B_i and H_i to the simulated results. In order to contrast the performance of TRANSURANUS, the homogeneous instrumented MOX rod G_i was analysed in parallel [136]. The validation of TRANSURANUS is completed with the analysis of the gap size in (Th,Pu)O_2 rod B_i and MOX rod G_i.

The initial content of the three rods is listed in Table 20. The Pu-content in rod H_i is significantly higher compared to the other two rods due to the sol-mas fabrication process.

Rod	B_i	G_i	H_i
Type of rod	(Th,Pu)O_2	(U,Pu)O_2	(Th,Pu)O_2
^{235}U		0.3	
^{238}U		99.7	
% PuO_2	7.98	9.07	12.84
^{238}Pu	0.015	0.015	0.015
^{239}Pu	91.47	91.47	91.47
^{240}Pu	8.29	8.29	8.29
^{241}Pu	0.18	0.18	0.18
^{242}Pu	0.045	0.045	0.045
^{241}Am	0.67	0.67	0.67

Table 20 Initial composition of the OMICO pins [29]

The fuel fabrication data of the three rods are listed in Table 21. The fuel stack of all the rods was 243 mm, containing 34 pellets of 7.14 mm height from which 6 of them were annular to host the thermo-couple. The total 'annular pellet stack length' was 46 mm approximately [31]. In the TRANSURANUS input files, the fuel active length was simplified by dividing the rod into twelve slices, from which three of them formed the annular stack.

The fuel centerline temperature during irradiation was measured 1 cm from the interface between the annular and solid pellets, which corresponds to the slice number 3 in the TRANSURANUS simulations. Prior ceramographic observations carried out on the samples showed semi-spherical pores in rod H_i produced in the sintering process [31]. This could produce less dense pellets, nonetheless, this was not the case. Fuel rod G_i had a density typical for a nuclear fuel whereas rod B_i was actually denser. The upper spring chamber, plus the internal hole of the annular pellets, plus the pellet-clading gap volume were accounted for as upper plenum volume as shown in Table 21. In addition, a virtual lower volume plenum of 0.15 cm^3 was also included in all the rods to perform correctly the simulations. A fully recrystallized zircaloy material was chosen instead the general Zircaloy-4 SRA to mitigate the uncertainty in the temperature measurement produced by cladding creep-down during irradiation [31]. The 4 mm height YSH (Yttrium Stabilized Hafnia) pellet positioned at stack-end of each rod that aimed the reduction of power peaking effects was neglected in TRANSURANUS simulations.

Rod	B_i	G_i	H_i
Fuel type	(Th,Pu)O_2	(U,Pu)O_2	(Th,Pu)O_2
Technology	sol-gel	sol-gel	sol-mas
Theoretical Density (%)	98	96.1	96.6
Density (kg/m^3)	9699	10563	9658
Grain size (μm)	5	12	5
Pellet diameter (mm)	5.905	5.904	5.903
Pellet inner hole diameter (mm)	1.6	1.6	1.6
Clad outer diameter (mm)	7.08	7.08	7.08
Clad inner diameter (mm)	6.07	6.07	6.07
Clad roughness (μm)	0.5	0.5	0.5
Active segment length (mm)	244	244	244
Upper plenum volume (cm^3)	2.41	2.51	2.45
Lower plenum volume (cm^3)	0.15	0.15	0.15
Initial filling gas	He	He	He
Filling gas pressure (T=25°C) (bar)	5	5	5

Table 21 Initial specifications for the instrumented rods [29, 30, 31]

The position of the instrumented and non-instrumented segments relative to the axial neutron flux is depicted in Figure 54. At the shown depth, the application of axial factors that accounted for the power gradient at which the rods were subjected was required. A gamma-spectrometry analysis showed a mismatch with respect to the estimated thermal balance. The linear power heating was thus multiplied by a correction factor that accounted for this difference between the gamma-spectrometry and thermal balance.

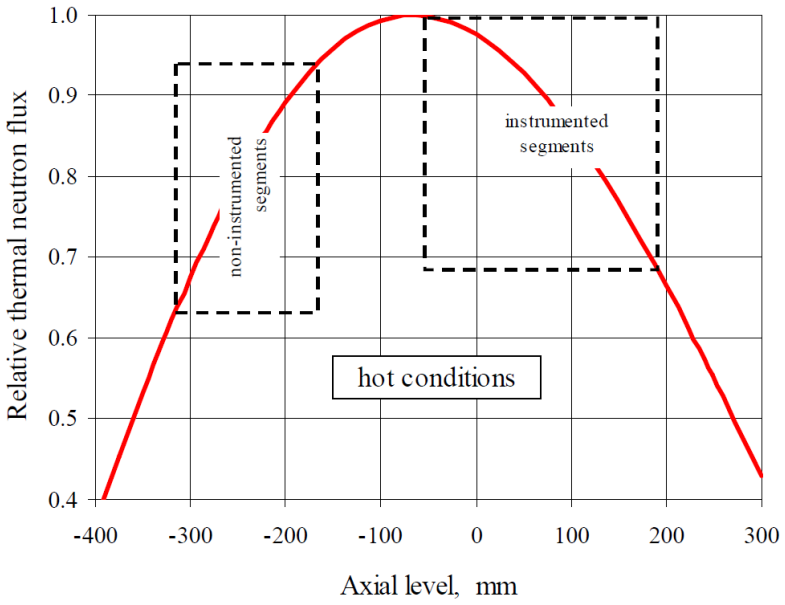

Figure 54 Axial position of the instrumented and non-instrumented segments referred to the axial neutron flux [20]

Table 22 presents these correction factors as the ratios between the gamma-spectrometry and thermal balance for rod average burn-up used in the TRANSURANUS simulations. The final burn-up attained with the gamma spectrometry balance was 10.5, 8 and 8.5 MWd/kg HM for the rods B_i, G_i and H_i respectively [32].

Rod	B	G	H
Correction factor	1.02	1.07	1.06

Table 22 Correction factor for the irradiation history as ratio between gamma-spectrometry and thermal balance performed in the rod average burn-up [32]

7.1.1. Analysis of the TRANSURANUS simulations

Figure 55 compares the linear power history of slice 3 where the centerline temperatures at full power were measured between the three rods. Rod B_i was subjected to the highest linear power while rod H_i to the lower and rod G_i was irradiated at an intermediate power.

The calculation of the centerline temperature in a solid cylindrical pellet in TRANSURANUS is based on a quasi steady-state approximate function within a small cylindrical ring 'j' with radius outer of r_o next to the center of the cylinder:

$$T(r=0,t) = T_o^j + \frac{q'''_{fik}}{4\lambda^j}(r_o^j)^2 \tag{7.1}$$

where q'''_{fik} is

$$q'''_{fik} = q''' - C_p\rho\frac{d\bar{T}}{dt} \tag{7.2}$$

q''' is defined according to Equation 4.1 and C_p, ρ, and λ^j are the heat at constant pressure, the density and the thermal conductivity respectively assumed as constant in each time step and ring 'j'. $\bar{T}$ is the radially averaged temperature and T_o^j is the outer temperature of the described ring. Equation 7.1 is a simplification of the general numerical solution of the temperature diffusion described in TRANSURANUS for center temperature.

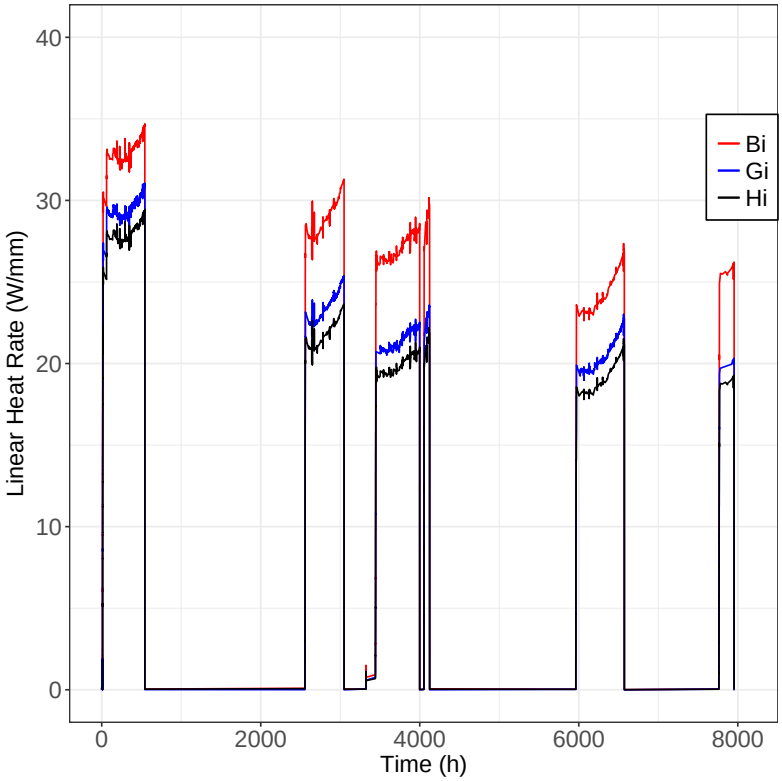

Figure 55 Linear heat rate history in section 3 for rods B_i, G_i and H_i

7.1.1.1 Rod B_i

Figures 56a to 56f compares the fuel centre temperature measured on-line to the results from TRANSURANUS during the six cycles to which the rod B_i was irradiated. The first case studied was named as 'Basic' and was used as reference because no modifications were applied to it. This case showed not only a disagreement in the values particularly in the first cycle (see Figure 57a), but also a different evolution of the shape of the predicted temperature along the time (see Figures 56b and 56e). In the rest of the cycles the predicted results from TRANSURANUS showed really good agreements to the on-line recorded centre temperatures, highlighting the results in the cycles 3 and 4 (Figures 56c and 56d), where TRANSURANUS values matched the experimental data points. A sensitivity analysis was performed in both thorium probes to study and analyse in further detail the election of the material properties summarised in Chapter 3.

The disagreement between the on-line recorded centerline temperature and the TRANSURA-

NUS results can be attributed to the thermal conductivity due to its importance in the calculation of the temperature profile in the pellet (see Equation 7.1). The model of the thermal conductivity employed for thorium-based fuels in TRANSURANUS is the Lucuta's model (Equation 3.15) [61]. While Lucuta factorizes the degradation of the thermal conductivity due to the dissolution and precipitation in the fuel matrix of the fission products, the correlation in TRANSURANUS for UO_2 and MOX fuels accounts for this effect by modifying the terms A and B (see Equation 3.14) in the general expression of the thermal conductivity. Nevertheless, at low burn-ups the degradation of the thermal conductivity due to fission products can be neglected, leaving the porosity as the main property that might vary the thermal conductivity. To this end, initial porosity was set to 6% as reported in the OMICO report [32]. The results obtained from this simulation are not only worse but also the shape of the temperature evolution does not change either. In contrast, the centreline results when the porosity was switched to 6% show in cycles 5 56e and 6 56e a good agreement. This is can be attributed to the larger porosity in the sample observed after irradiation. Nevertheless, the largest disagreement among the sensitivity cases was the case in which the relocation was switched off.

Examinations of rod cross sections at low burn-ups show that fuel pellet cracks promote a relocation of pellet fragments causing an additional gap closure [9]. The relocation is a phenomenon at low burn-up that mainly happens in radial direction. Therefore, cracking and relocation increases the thermal resistance in the pellet while reducing the thermal resistance of the pellet-cladding gap by reducing its effective size [9]. This can yield a disagreement between simulated and measured centre temperatures. In the The TRANSURANUS relocation model is adopted from FRAPCON code [9] in which the relocation is the driver mechanism of almost 50% of the fuel-cladding gap before any strain/stress:

$$\begin{aligned} \frac{\Delta G}{G} &= 30 + 10fbu; lhgr < 20kW/m \\ &= 28 + Pfactor + fbu \times (12 + Pfactor); lhgr < 40kW/m \\ &= 32 + 18fbu; lhgr > 40kW/m \end{aligned} \tag{7.3}$$

In Equation 7.3, $\frac{\Delta G}{G}$ is the change of gap size and fbu represents the burn-up that is divided by 5 if the burn-up is lower than 5 MWd/kg and takes the value of 1 if it is larger than 5 MWd/kg HM [9]. Finally $Pfactor$ depends on the $lhgr$ linear heat rate in kW/m as $\frac{(lhgr-20)5}{20}$. This process begins at BOL (Beginning of Cycle) and quickly reaches equilibrium [9]. As can be observed in Figures 56a to 56f, the centreline temperatures are even larger and show the largest deviation among all the sensitivity cases. This was not expected since the cancellation of the relocation would produce a larger gap size, and therefore, the centreline temperatures should have been lower. Furthermore, the predicted slope of the centerline temperature as a function of time is more significant in comparison to the flat temperature evolution measured.

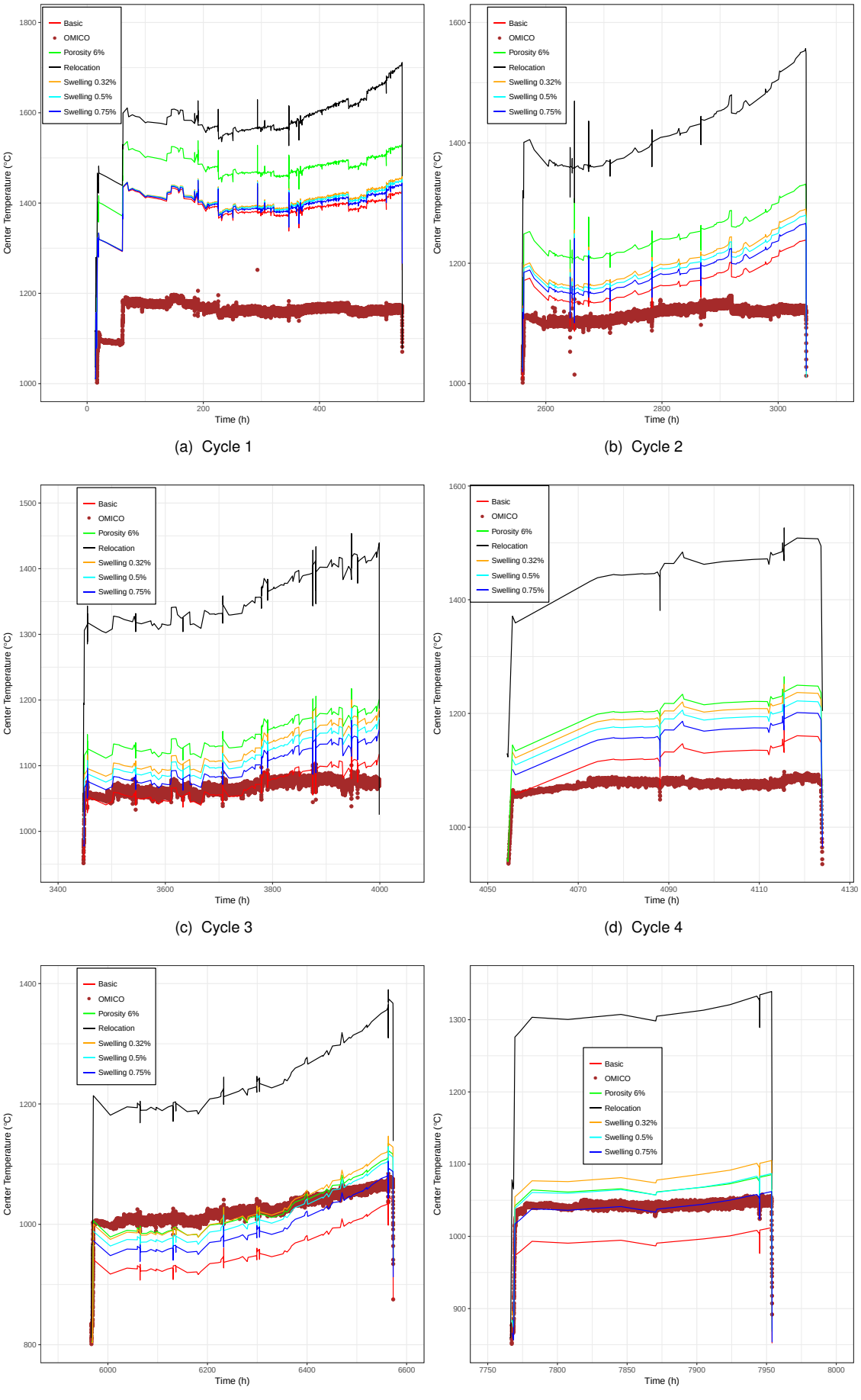

(a) Cycle 1

(b) Cycle 2

(c) Cycle 3

(d) Cycle 4

(e) Cycle 5

(f) Cycle 6

Figure 56 Sensitivity analysis on Rod B_i

Since the cladding creep down is well validated in TRANSURANUS for the type of material used in OMICO, the third thermo-mechanical property studied was the swelling due to fission products named as 'Swelling' in the Figures 56a to 56f. As previously mentioned, the gap size modification during irradiation has an impact on the centerline temperature. A small gap width reduces the gap conductance and increases the pellet temperatures profile due to lower conduction. In principle, the value of 1.25% per 10 MWd/kg HM given by S.A. Rabin and proposed in the OMICO project [10] is believed to be slightly large in comparison to the studies carried out by Spino [58]. He claimed that swelling due to solid fission product accumulation is between 0.15 and 0.45% per 10 GWd/t HM and swelling due to fission gas production is approximately 0.56% per 10 GWd/t HM, having in total swelling percentage approximately between 0.7% and 1% per 10 MWd/kg HM (for further information see Section 3.3). Therefore, a reduction of this parameter to 0.32, 0.5 and 0.75% per 10 GWd/t HM for the sensitivity analysis was performed, following Spino's publication. Figures 56a to 56f show, in general, similar results from the modifications of the swelling rate to the 'Basic' case, except in the last cycle (Figure 56f) where the 0.75% swelling profile matches perfectly the measurements. This is reasonable because at low burn-up this property is negligible.

A numerical assessment of the 6 cases was carried out by calculating the total relative difference at full power or high temperature. The relative differences between measurements and simulated values are calculated with the following formula:

$$S = \sqrt{\frac{1}{N}\sum_{i}^{N}\left(\frac{M_i - C_i}{M_i}\right)^2} \tag{7.4}$$

where S is the total relative difference and M_i and C_i are the measured and the calculated temperature at the same time respectively. N is the total number of points that corresponds to the total number of points used in the calculations because there was a smaller number of time point steps in TRANSURANUS than in measurements in order to speed up the execution of the program. Generally this number, N takes the value of 800 points approximately, while in OMICO there were around 120.000 temperature point measurements. Since the time points between TRANSURANUS and OMICO did not match, a simple linear interpolation was done for the recorded values in most cases.

Table 23 compares the relative difference values calculated through Equation 7.4 for the six sensitivity cases. As was previously foreseen, the two best cases are the 'Basic' and the correction of the swelling to 0.75% with a total relative difference of 14.7% and 15.45% respectively. The other two cases, in which the swelling due to fission gases was modified i.e. 'Swelling 0.32%' and 'Swelling 0.5%', also present similar values with a relative difference of 16.27% and 15.92% respectively. The relative difference of the cases 'Relocation' and 'Porosity 6%' present the largest deviation with the values 33.08% and 21.20% as expected.

A graphical comparison of the scatter of these values can also be appreciated in Figures

57a to 57f. As can be seen the largest scatter among the six cases is found at temperatures around 1200°C that coincide with the first two cycles. It must be noted that the largest measurements of the centre temperature were performed during the first two cycles. This influences in the calculation of the relative difference as the values listed in Table 23 are due to the deviations in the first two cycles of the TRANSURANUS simulations.

	RodB_i
Basic	14.7
Relocation off	33.08
Porosity 6%	21.20
Swelling 0.32%	16.27
Swelling 0.5%	15.92
Swelling 0.75%	15.47

Table 23 Comparison of the relative differences (in %) of each sensitivity analysis case to the recorded centerline temperatures in rod B_i

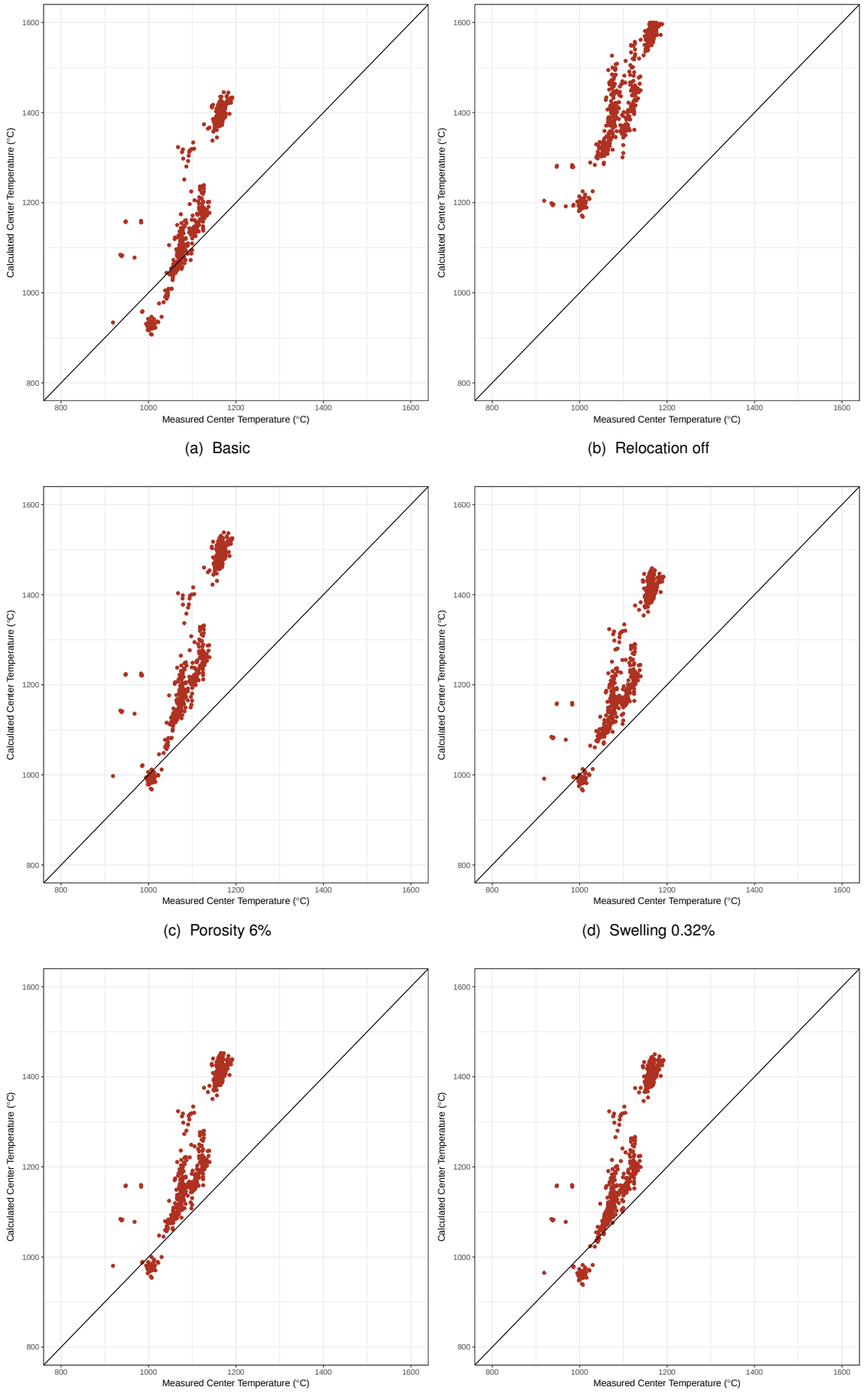

(a) Basic

(b) Relocation off

(c) Porosity 6%

(d) Swelling 0.32%

(e) Swelling 0.5%

(f) Swelling 0.75%

Figure 57 Measured and simulated center temperatures of Rod B_i

A visual measurement of the gap size in rod B_i in an immediate upper stack position to the annular pellet that corresponded to the solid slice 4 in TRANSURANUS simulations was also performed during the extension of the OMICO project, LWR Deputy [36].

Sensitivity cases	Gap size (μm)
Basic	23.72789
Relocation	60.33087
Porosity 6%	23.24319
Swelling 0.32%	34.91688
Swelling 0.5%	32.76801
Swelling 0.75%	29.76966

Table 24 Comparison of the gap size values calculated in the sensitivity analysis rod B_i

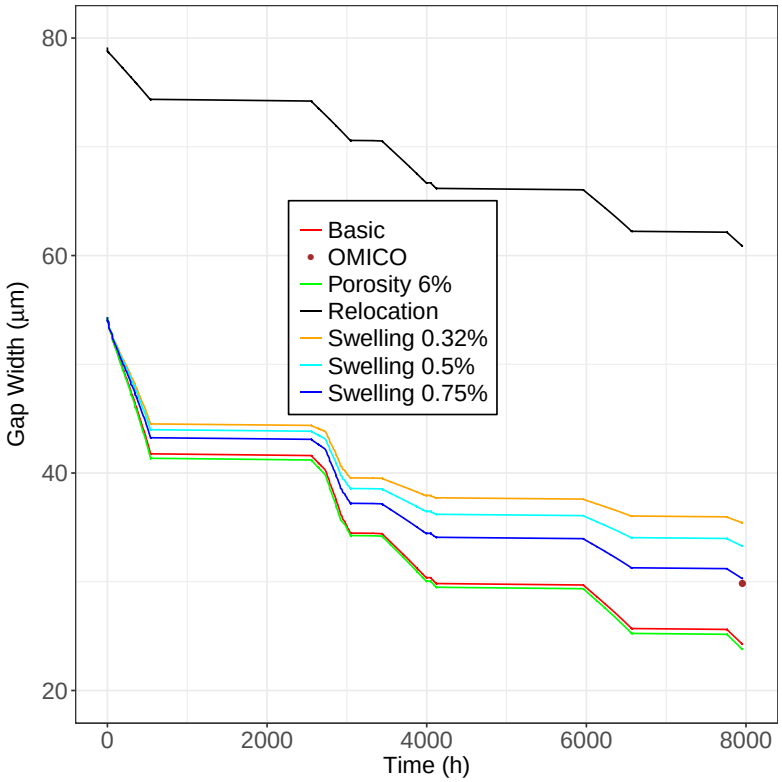

Figure 58 Gap size in rod B_i

The final value of the gap width observed was 29.8458 $\pm$ 3.817 μm, and, as can be seen in Figure 58 and Table 24, the 'Swelling 0.75%' case perfectly matches the measured value, whereas the 'Basic' and 'Porosity 6%' resulted in a good agreement as well, but with lower

values than in the measurements. In general, all the values agreed with the visual measurement except the case 'Relocation' whose value is far larger as was expected and the cancellation of the relocation did not yield better results.

In rod B_i an apparent porosity of 30% at the rim of the pellet was observed with a high concentration of cracks [36] attributed to grain pull-out. The grain dislodgement is an effect that happens at low burn-ups, when thermal gradients may pull out the pellet grains or powders, which they were weakly bonded to each other during the sintering and the polishing stages before being mounted in the rod. Due to the higher melting point of thorium, a higher amount of power supplied in the sintering process is required for the pellet, and, eventually, those bonds among powder grains do not take place. These observations have two main consequences for the simulation of the behaviour of the pellet in TRANSURANUS. First, a larger relocation in the pellet happened, thus the case in which the relocation was disabled in the input file, could have been rejected. Secondly, the case in which the initial porosity was set to 6% has large disagreements in the first two cycles, but in the following four cycles the centerline temperature predictions improve noticeable. As the irradiation is performed and consequently the grains pull-out takes place, the porosity of the pellet increases, and therefore the observations and the TRANSURANUS results agree for this sensitivity case. Another simulation was run, in which a linear porosity increment from the centre of the pellet of about 2% to the outer rim of around 30% was modelled. The results of this simulation are not shown in this thesis since the centreline temperatures calculated were above 2000°C, close to the melting point.

Despite the acceptable results simulated with TRANSURANUS, it is soon to draw definitive conclusions regarding the extension and performance of TRANSURANUS for thorium-based fuels, since the porosity observed at 10.5 MWd/kg HM in this rod is unusual for fuels irradiated under LWR conditions. Therefore, the assessment of rod H_i was carried out.

7.1.1.2 Rod H_i

For the second (Th,Pu)O_2 fuel rod, H_i, assessed in the OMICO project and also studied in TRANSURANUS the same approach previously described was carried out. For this rod, no PIE were performed, therefore no atypical observations were reported. Nevetherless, the same sensitivity cases were carried out to be consistent with the work done. Figures 59a to 59f show the comparison of the 6 predicted values for the 6 sensitivity cases to the on-line recorded measurements of the centre temperature during the 6 cycles of irradiation to which the rod was subjected. An early comparison of the experimental data points between rods B_i and H_i shows that the temperatures obtained in rod B_i were higher due to the larger linear power rate to which this rod was subjected, as can be seen in Figure 55. The shapes of the evolution of the temperatures with time for both tested rods are practically identical.

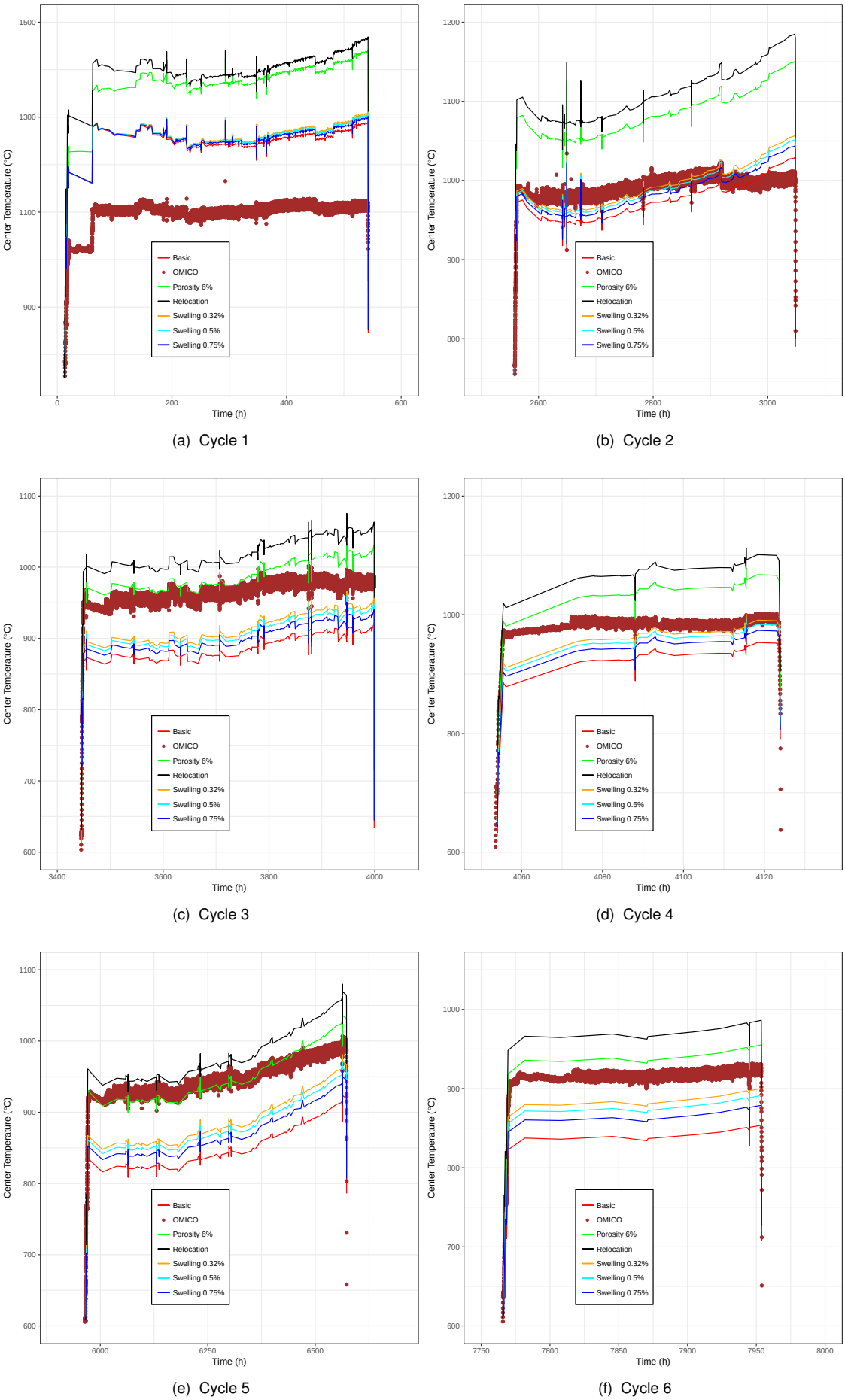

(a) Cycle 1

(b) Cycle 2

(c) Cycle 3

(d) Cycle 4

(e) Cycle 5

(f) Cycle 6

Figure 59 Sensitivity analysis on Rod H_i

In the first cycle (Figure 59a) the largest discrepancies are found, while in the following cycles the agreements between estimated and experimental values are good. As happened before with rod B_i, the cases 'Relocation' and 'Porosity 6%' show the worst estimated values. The largest discrepancies of these two cases are observed in the first two cycles, especially in the second cycle (Figure 59b), where all cases show satisfactory results except 'Relocation' and 'Porosity 6%'. Meanwhile, in the rest of the cycles the differences can be compared to the other study cases. In the cycle 5 59e, the results of 'Relocation' and 'Porosity 6%' are even better than the other sensitivity cases. As was previously stated, the cancellation of the relocation for rod H_i is meaningless since it has the opposite effect, i.e. an increment of the temperature in the first cycle. Regarding the shape of the curves along the time, the curves of the 6 sensitivity analysis calculated in cycle 2 (Figure 59b) show a different evolution with respect to the observations, especially at the end of the cycle. This is also the case in cycle 5 (Figure 59e), where the slopes of the predicted temperatures of the six cases are steeper than the evolution of the measured temperatures. This was also observed in rod B_i. In general, the results predicted with TRANSURANUS for rod H_i are better than for rod B_i. Having measured gap size for rod H_i would also allow to contrast the correlations implemented in TRANSURANUS for thorium fuels that accounts the swelling of the fuel.

A graphical and numerical comparison regarding the scatter of the calculated points and their relative differences at full power was done again, as shown in Figures 60a to 60f and Table 25 respectively. The results listed in the table show that the 'Swelling 0.75%' case presents the lowest deviation (10.8%). The 'Swelling 0.32%', 'Swelling 0.5%' and 'Basic' cases show deviations of 10.86%, 10.82% and 10.88% respectively, pracitally similar to 'Swelling 0.75%'. Among all the sensitivity cases, the largest discrepancies are found again in 'Porosity 6%' and 'Relocation' cases whose relative differences are 18.46 and 20.27% respectively.

	RodH_i
Basic	10.88
Relocation off	20.27
Porosity 6%	18.46
Swelling 0.32%	10.86
Swelling 0.5%	10.82
Swelling 0.75%	10.80

Table 25 Comparison of the sensitivity analysis in % in rod H_i

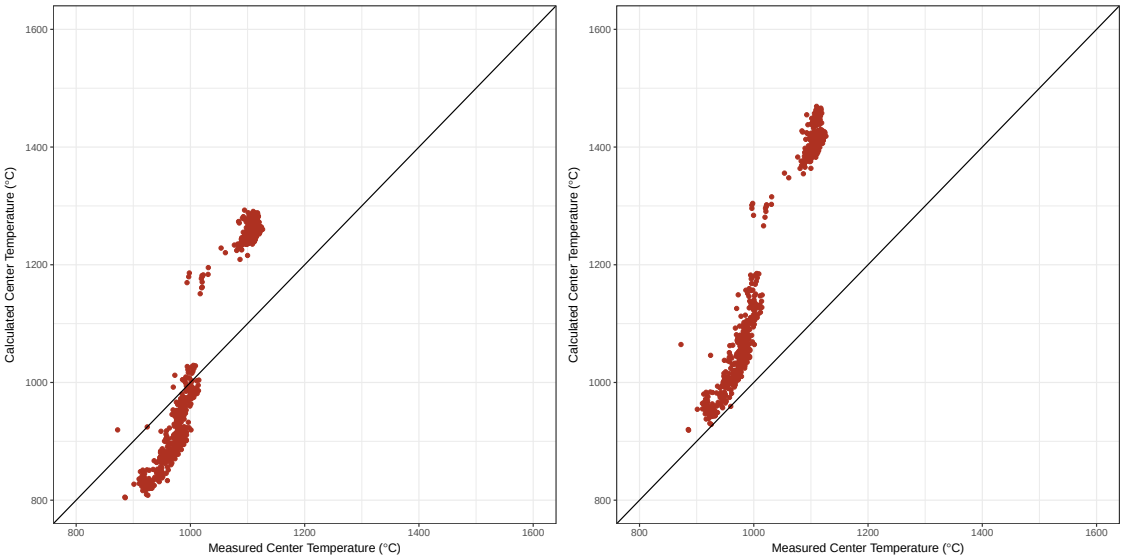

(a) Basic

(b) Relocation off

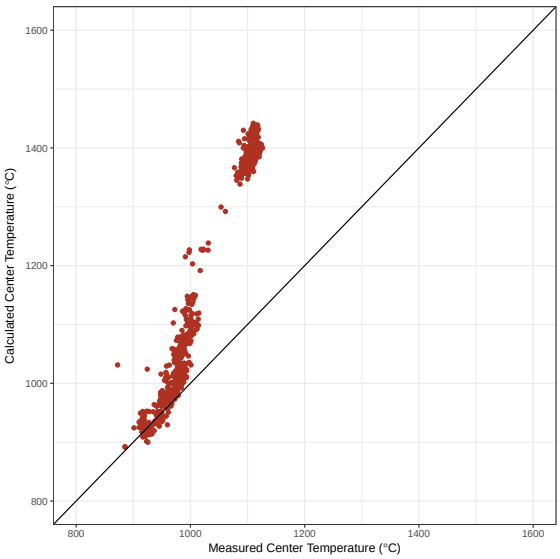

(c) Porosity 6%

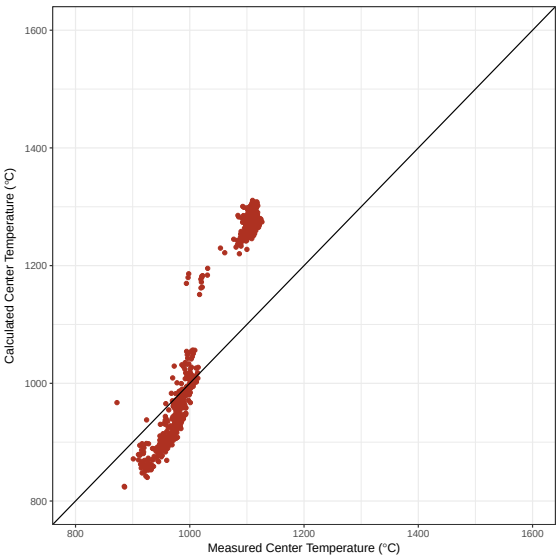

(d) Swelling 0.32%

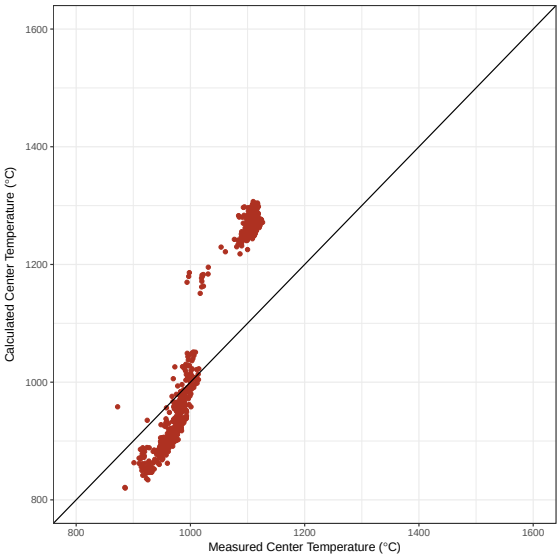

(e) Swelling 0.5%

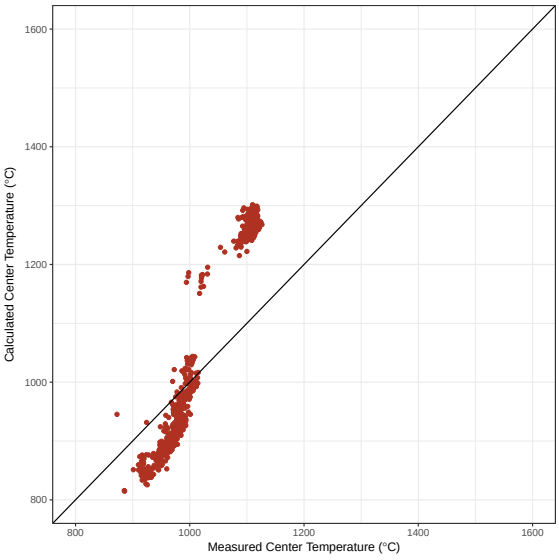

(f) Swelling 0.75%

Figure 60 Measured and simulated center temperatures of Rod H_i

In general, for all the sensitivity cases, the largest differences are found in the first two cycles where the highest temperatures were measured, as happened previously to rod B_i as well. Since the amount of data points obtained in these two cycles are larger than in the following cycles, the values of the relative differences between TRANSURANUS and OMICO observations are mainly due to cycle 1 and 2. An equal amount of data points in each cycle would give the real deviation of the simulations without distinguishing any cycle by the amount of data points measured.

7.1.1.3 Rod G_i

Parallel to the assessment of (Th,Pu)O_2 rods, the MOX G_i rod was analysed to have an overview of the TRANSURANUS performance of thorium-based fuels in comparison to the already validated TRANSURANUS MOX version. In this rod only two sensitivity cases were studied. The first one was the 'Basic' case, as done for the previous rods. In the second case, a modification of the densification was enabled as reported by Schubert [136]. The densification is the process by which as-fabricated porosity is removed on a time scale of hours after the beginning of the irradiation. The increment of the density is also enhanced by the grain growth. Afterward, the porosity of the material begins to decrease due to the solid fission products generation [3]. Olander [3] described a very simple model that was slightly modified and implemented in TRANSURANUS, where the porosity P depends on the burn-up as followed:

$$P(bu) = P_\infty + (P_0 - P_\infty)e^{-\frac{5}{bu_0}bu} \tag{7.5}$$

P_∞ indicates the minimum porosity that is attained at the end of densification while P_0 is the fabricated porosity. bu_0 is the burn-up from which the densification is no longer an important effect in the fuel behaviour and bu is the burn-up expressed in the same units as bu_0. The parameters P_∞ and bu_0 were therefore switched on. In the 'Basic' case those input parameters took the values of the fabricated porosity (3.9%) and 3000 MW/kg HM respectively, while in the sensitivity case 'Densification' the modified values were 2% of porosity and 10000 MWd/kg HM.

The two case studies show in general, in the six cycles, a fair agreement in comparison to the experimental data along the irradiation time. In the first cycle the agreement of the 'Basic' with the OMICO records is complete, whereas in the rest cycles of the 'Densification' case shows a better evolution, especially in cycles 4 (Figure 61d) and 6 (Figure 61f). Nonetheless the difference in the other cycles is not so large. On the other side, the 'Basic' case presents the largest mismatches in cycles 2 (Figure 61b), 3 (Figure 61c) and 5 (Figure 61e). In contrast to the thorium-based rods, the shape of the curves is better in the first cycle, having the biggest discrepancies at the beginning of cycle 4 (Figure 61d) and in the second cycle (Figure 61b). In any case, the evolution of the temperature along the time estimated with TRANSURANUS for rod G_i is comparable to the slopes of the temperatures against the time exhibited for (Th,Pu)O_2 rods (B_i and H_i).

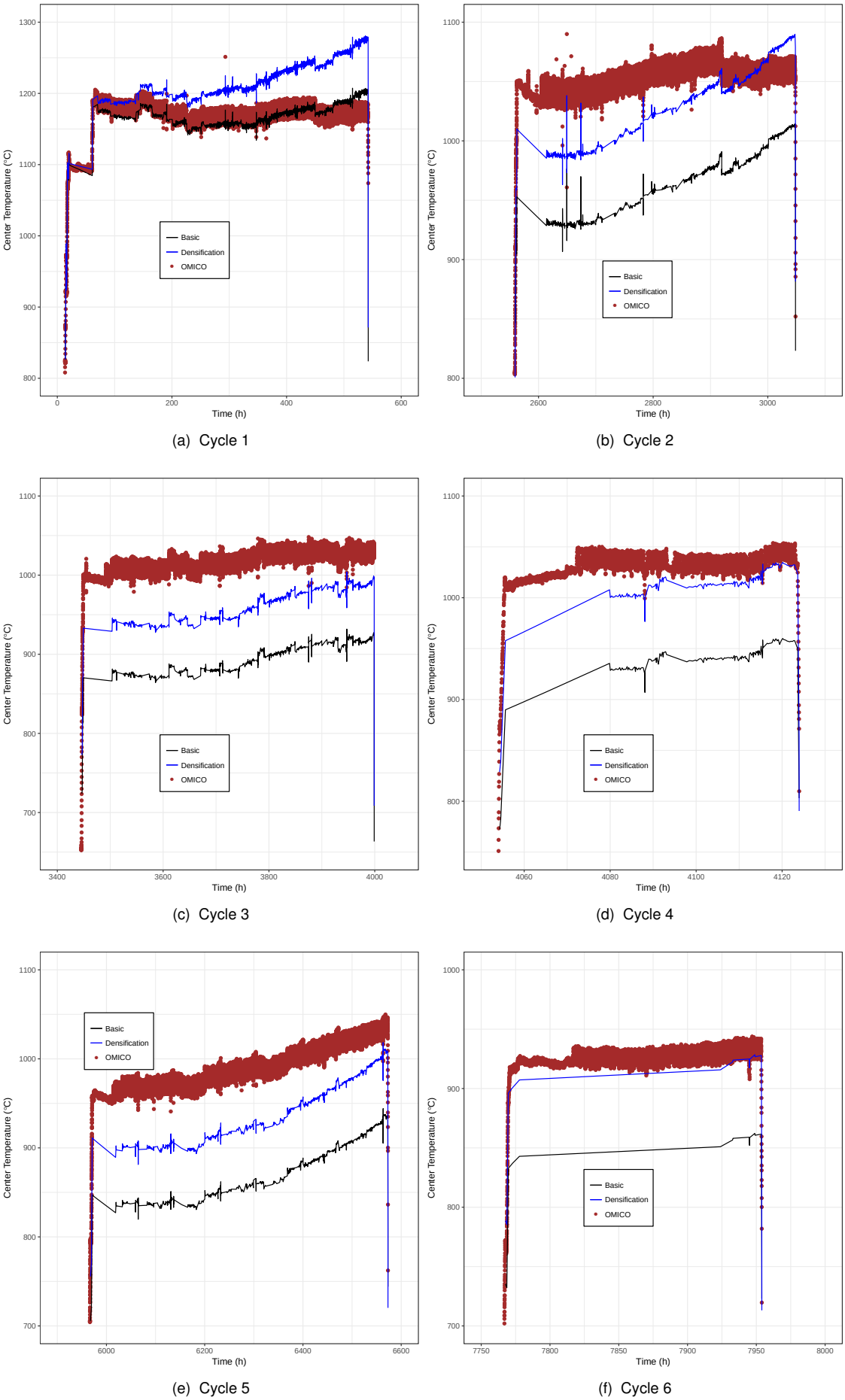

(a) Cycle 1

(b) Cycle 2

(c) Cycle 3

(d) Cycle 4

(e) Cycle 5

(f) Cycle 6

Figure 61 Sensitivity analysis on Rod G_i

As done for (Th,Pu)O_2 rods, an identical numerical analysis according to Equation 7.4 for the two cases was done and reported in Table 26. To complete the quantitative analysis, the two dispersion plots for both cases are displayed in Figures 62a and 62b. The results show that a better performance is reached when the densification is enabled improving considerable the calculated centerline temperatures. Opposite to all the evaluations, it is worth mentioning that the relative difference scattering in rod G_i case 'Basic' is fair at high temperatures, which is clearly reflected in Figure 61a as well.

	RodG_i
Basic	9.56
Densification 98% TD (10000 MWd/kgHM)	5.74

Table 26 Comparison of the sensitivity analysis in % in rod G_i

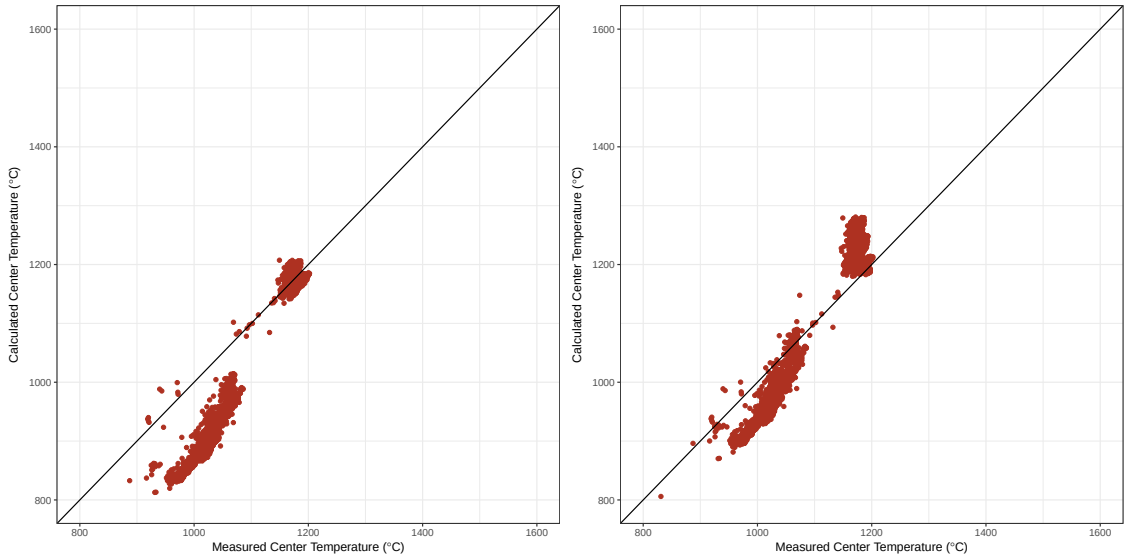

(a) Basic (b) Densification

Figure 62 Measured and simulated center temperatures of Rod G_i

The conclusion of the analysis of rod G_i is done by comparing the gap width observed to the two values obtained from the two sensitivity cases simulated with TRANSURANUS. The gap size reported as part of LWR Deputy [36] showed a larger value, 72.552 $\pm$ 2.9959 μm in contrast to the observation in rod B_i. A lower crack concentration in the pellet reported could also entail this larger value. Also, the lower centerline fuel temperature yields less strain-stress due to thermal gradients and contributes to have a wider gap size. Moreover, the same problem of rod B_i regarding high porosity at the rim of the pellet was reported, but in this rod type this problem was not studied.

The calculation shows larger disagreements than the predicted values for thorium rods with

the 'Basic' case as the worst estimated. A densification would imply the shrinkage of the pellet by porosity removal, and therefore the increment of the gap size in the early irradiation cycles. The shape of the curve, that shows the evolution of the gap size along time is different between rods B_i and G_i. This can be attributed to the power histories of (Th,Pu)O_2 rods which were condensed to speed up the execution of TRANSURANUS. The data points used in rod G_i were almost 4600, having utilized around 800 for rods B_i and H_i instead.

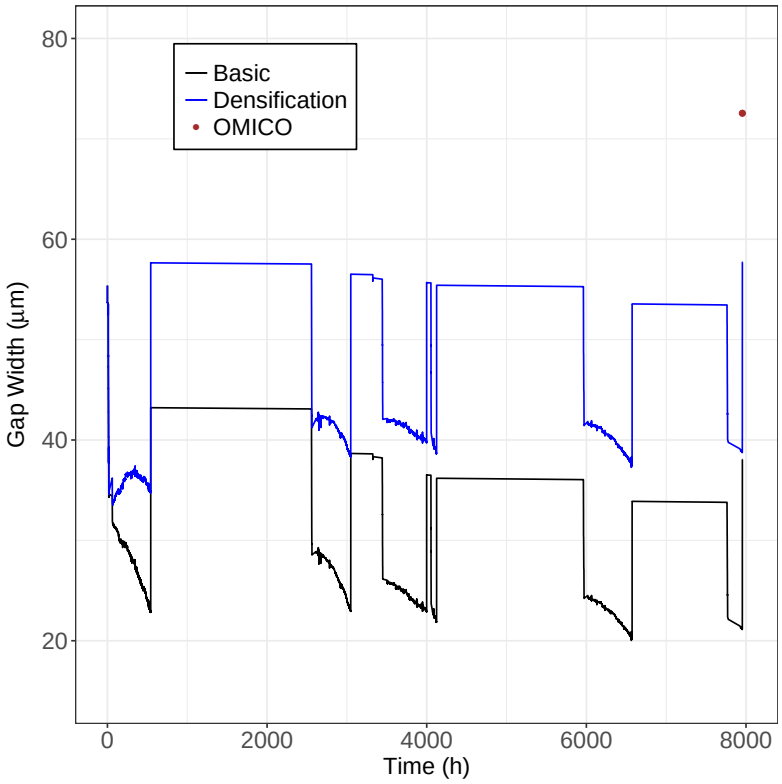

Figure 63 Gap size in rod G_i

	Gap size (μm)
Basic	38.04
Densification 98% TD (10000 MWd/kgHM)	57.71

Table 27 Comparison of the gap size values calculated in the sensitivity analysis rod G_i

It can be concluded that the performance of the first version of TRANSURANUS for (Th,Pu)O_2 is good concerning the centerline temperature. If the 'Basic' cases of rods G_i and H_i are assessed separately to the others, the relative differences between both simulations are almost identical, having 9.545 and 10.875% respectively. This proves that the extensions of the burn-up model and the implementation of the chosen material properties are good. Moreover, this first version is a good starting position from which TRANSURANUS for thorium fuels can be improved for future developments and assessments.

8

Shippingport Ligh Water Breeder Reactor

The SAPS (Shippingport Atomic Power Station) was the first large-scale, nuclear power plant in the United States owned by the DOE (U.S Department of Energy) (formerly Atomic Energy Commission). It was also the first plant in the world which operated only to produce electric power. In 1965 the DOE set up the LWBR programme at the Shippingport Station that aimed to build a breeder reactor that utilized thorium instead of uranium. The main reason of using thorium was that at that time thorium was focalised to power production and pacific use while uranium was employed for military purposes. The design and development of this programme was carried out by the BAPL operated by the Westinghouse Electric Corporation.

The LWBR started operation in 1977 and a year after in 1978 the DOE established another programme called the AWBA (Advanced Water Breeder Applications) to evaluate the concept of the LWBR for a commercial-scale. This programme studied the feasibility of the LWBR technology and the problems that could be faced by the industry as well as its economic viability. In 1982, after 5 years of operation the LWBR was shut down. The reactor was operated for 29,047 efph (effective full power hours) almost twice the power than the designed goal which was 15,000 efph drawing a total success of the programme [21].

After the shutdown, all the modules (assemblies) were shipped to the ECF (Expended Core Facility) at the INEEL. Around 1000 rods were removed from the modules. Some of them were sent to two divisions of the ANL (Argonne National Laboratory) in Idaho and Chicago and the rest was kept at ECF. Destructive and non-destructive examinations were performed in the rods to study the physical, chemical and radiological behaviour during five years of irradiation. After the experiments, all the rods and rodlets that remained were sent to the ECF for dry storage.

8.1. Reactor design

The LWBR was a PWR reactor at the Shippingport Station in Pennsylvania, USA that was modified to host the first ^{232}Th/^{233}U breeder reactor [21, 22], but with the constrains of the previous PWR structures. The main disadvantage was the lack of instrumentation, which brought the difficulties in carrying out simulations of the entire core.

The height of the reactor vessel was 10.05 m and its inner diameter was 2.74 m [21, 22]. Inside the vessel there was another cylinder called core barrel, whose function was to locate

the modules and it was welded to a supported flange that rested on the top of the vessel.

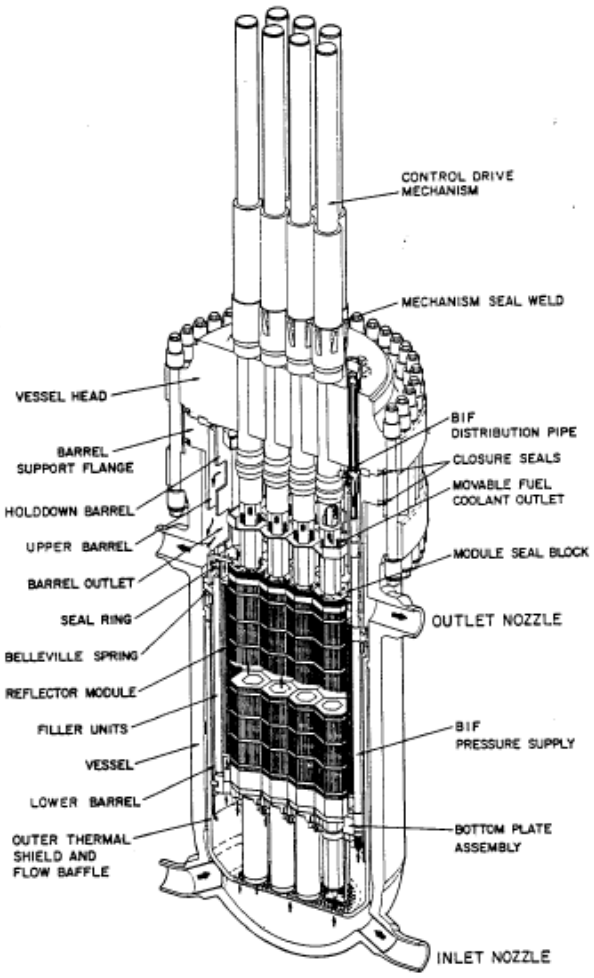

Figure 64 Scheme of the Shippingport reactor [21]

The water entered to the reactor through four inlet nozzles at the bottom. The water was heated when it passed upward through the modules and exited the reactor as steam through the four outlet nozzles Figure 64.

Figure 65 shows the four regions in which the reactor was divided. There were a peripheral radial and axial reflector (lines) that were composed of thorium whose purpose was to reduce the neutron leakage from the core.

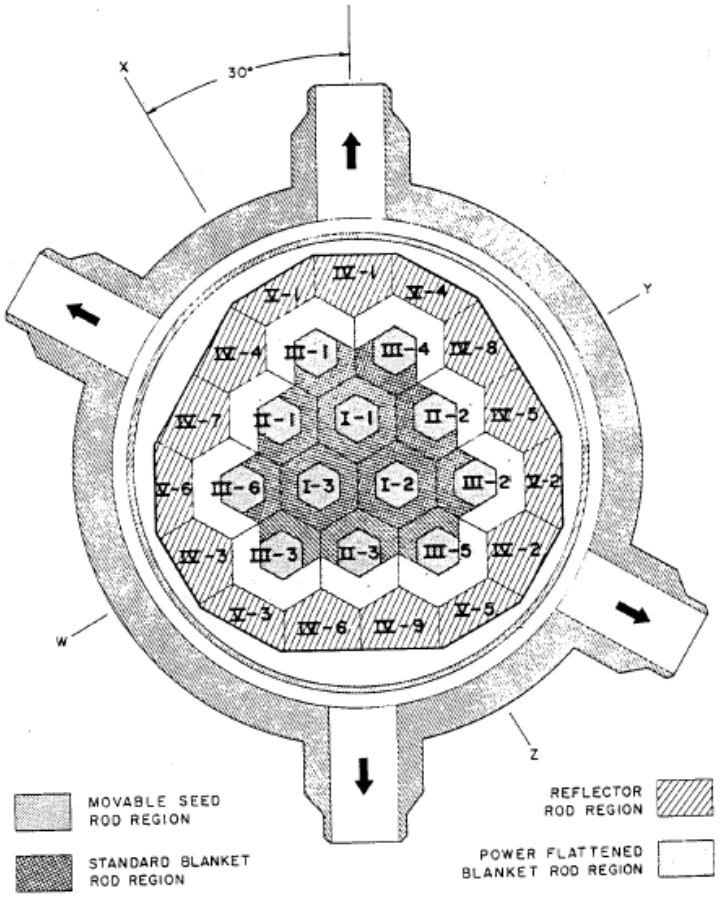

Figure 65 Shippingport vessel cross section [21, 22]

As can be seen in Fig. 65, in the core there were nine power-flattening blankets (white) whose inclusion aimed to produce an uniform power distribution. These nine power-flattening blankets, with the standard blankets (black), formed the asymmetrical hexagon blankets as part of the modules Type II and III in contrast to the Type I modules that were surrounded by an uniquely standard blanket. The power-flattening blankets differed from the standard blankets in the slightly more ^{233}U content and thickness. The last region of the reactor was the movable seeds (gray) where the neutrons were produced through fission reactions in ^{233}U.

Another important and distinctive feature introduced in this reactor was the geometry control. Instead of using conventional poison rods, soluble or burnable poison to control the core reactivity, the movable seed fuels whose most outer rods had heterogeneous axial content of ThO_2 and $(Th,U)O_2$ could change their axial position relative to the blanket. With this axial motion the neutron excess was absorbed when the pure ThO_2 axial content of the seed faced the pure ThO_2 of the surrounded blanket, avoiding thus the wast of neutrons in control rods or burnable absorbers [21].

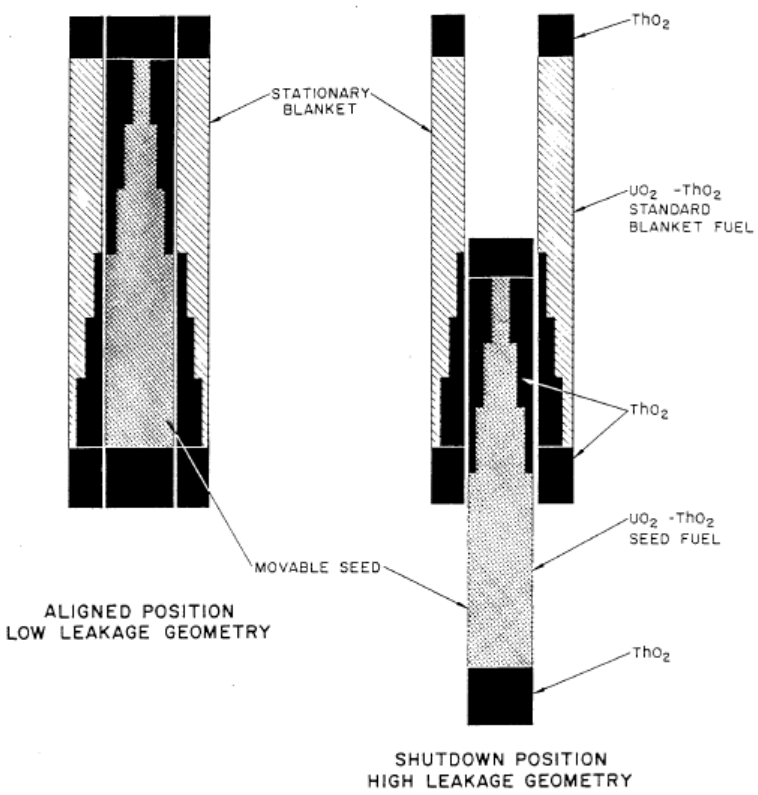

Figure 66 Axial movable seeds [21, 22]

At the beginning of the core life, the seeds were located lower than the stationary blanket, and they were slowly moved upwards until they were at the same level and criticality was attained. During reactor operation, the reactivity was controlled by varying the getaway of neutrons from regions with highly loaded seed into the lower loaded blanket regions, see Figure 66. In order to shut down the reactor, all the seed assemblies were set lower than the stationary blanket to decrease the core reactivity. The usage of this new method did not waste neutrons in control rods or burnable absorbers, because all the neutron excess was captured in the blankets containing fertile thorium dioxide.

8.1.1. Fuel Modules

The modules were formed by two parts. The central part was the seed and has a shape of an hexagon, see Figure 67a. The blanket had an hexagonal-ring shape in order to host the movable seed, see Figure 67b. For the modules Type II and III the blankets were non-concentric hexahedra, distinguishing two different parts: the standard and the power-flattening. All the seeds contained 619 rods in contrast to the blankets, whose number of rods varied depending on the Type. For example, a Type III had 533 rods (446 from power-flattening blanket and 187 standard blanket), while a Type II had 564 (303 from power-flattening blanket and 261 from standard blanket). The enrichment of the rods in the seed changed radially as well as axially. In the center region (yellow) the rods were highly enriched with a 5.2 wt% U fissile content,

while in the outer zones (green, blue and black) the enrichment was a 4.3 wt% U fissile.

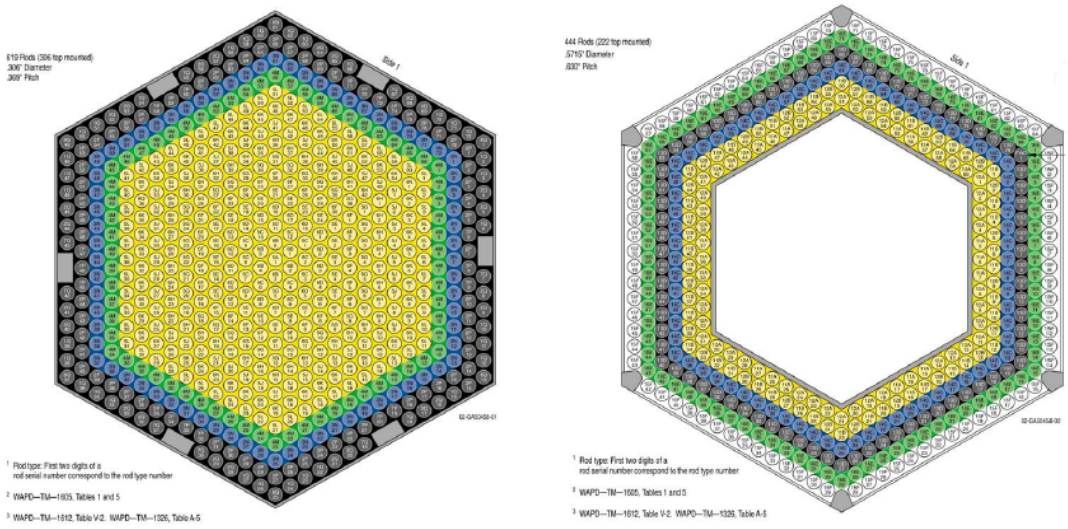

(a) Seed (b) Blanket

Figure 67 Seed and blanket from a Type I module [21]

8.2. Assessment of rod N

The LWBR Shippingport programme was selected to validate the first TRANSURANUS burn-up and the a-thermal release version for (Th,U)O_2 fuels. As was done previously for the (Th,Pu)O_2 version, the Monte Carlo code Serpent was used with the purpose of obtaining the one-group effective cross sections. In this case, the radial profile functions were not derived due to the absence of EPMA radial profiles that may validate them. However, it can be stated that the radial function for ^{232}Th should only be introduced for the (Th,^{233}U/^{235}U)O_2 fuel. The absence of ^{240}Pu and ^{238}U in the cycle of this type of fuel justifies the omission of their radial absorption functions in their depletion equations.

The rod selected for the validation was located with the number 0507057 in the cell position 5c10 in the seed in the central Type I, as highlighted in Figure 68. This rod was then named rod N.

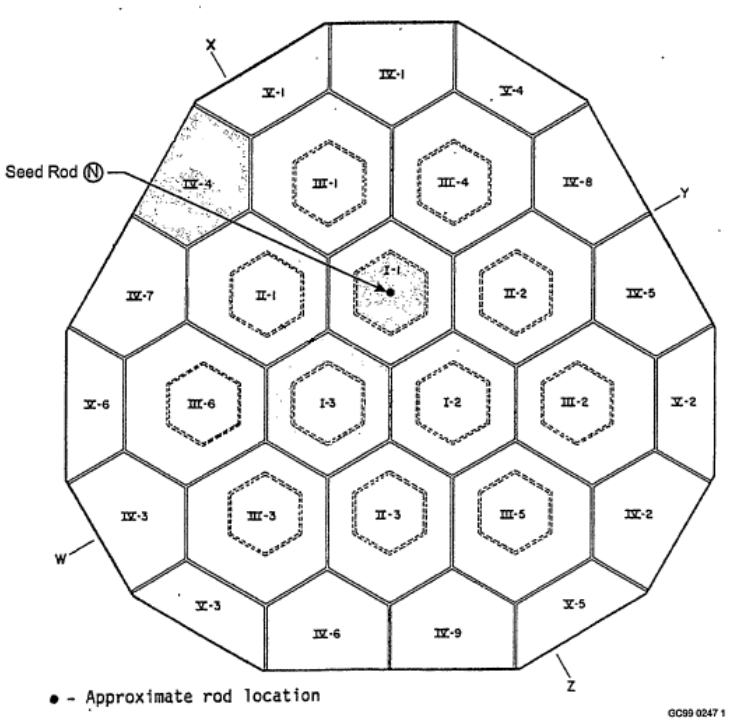

Figure 68 Position of the rod N in the core [23]

The initial composition and geometric characteristics of rod N and module Type I are listed in Tables 28 and 29, respectively.

The LWBR started operation in 1977 and lasted until 1982 when it was shut down after 5 years of operation, supplying a nominal electrical output power of 50 MW_e. After the shutdown, all the modules (assemblies) were shipped to the ECF at the INEEL. Then, rod N was shipped to the ANL, where the cladding rod was punctured with a laser and the released gases were collected in a sample collection tube and later analysed by mass spectrometry [21]. The rod was then sheared into 8 segments with approximately same the lengths. All the segments were dissolved in Thorex (13.6 M HNO_3, 0.06 M HF) followed by a second dissolution in a Thorex-0.06 M Al^{+3} solution followed by a hot rinse and a cold rinse with diluted nitric acid. Finally the segments were subjected to the fluoride-catalyzed nitric acid, and then boiled at high pressure [23]. The samples were analysed with MSID (Mass Spectrometric Isotopic Dilution) that gave the isotopic composition in grams. Among all the rod N sheared segments, the N03 slice, that was located in the middle of the rod, was employed to validate MCNP simulations as part of the Shippingport programme [23].

^{232}**Th**	^{233}**U**	^{234}**U**	^{235}**U**	^{236}**U**
0.94052	0.05844	0.00076	0.00005	0.00001

Table 28 Binary pellets initial isotopic concentration in mol/mol HM

	Rod N
Fuel Length	2.64 m
Rod Diameter	7.6 mm
Lower Plenum	67.1 mm
Binary Pellet Diameter	6.4 mm
Thoria Pellet Diameter	6.5 mm
Cladding outer diameter	7.7 mm
Cladding inner Diameter	6.7 mm
Porosity	2.45%
Coolant Pressure	13.79 MPa
Coolant Temperature	277.72°C
Coolant Flow Rate	615.298 (g/h)
Fillgas Pressure	0.689 MPa
Fillgas Temperature	25°C
Fuel density	10.042 g/cm^3
Triangular fuel rod pitch	9.3726 mm

Table 29 Rod N data input

8.2.1. Radially average concentrations comparison

Figure 69 represents the central module (seed and blanket) Type I, obtained from the 2-D Serpent simulation, where the rod N is highlighted in the cell position 5c10 according to [21, 23]. In the Serpent simulation three simplifications were considered: (a) the structural grid whose aim was to keep the distance between the rods to flow upward the water [137] was neglected, (b) the initial nuclide concentration of the rest of the rods in the central seed was assumed to be the same and (c) the geometry of the rods in the blanket was the same as in the seed. The evaluated nuclear data utilized in the Serpent simulations were OECD/NEA JEFF-3.1.1.

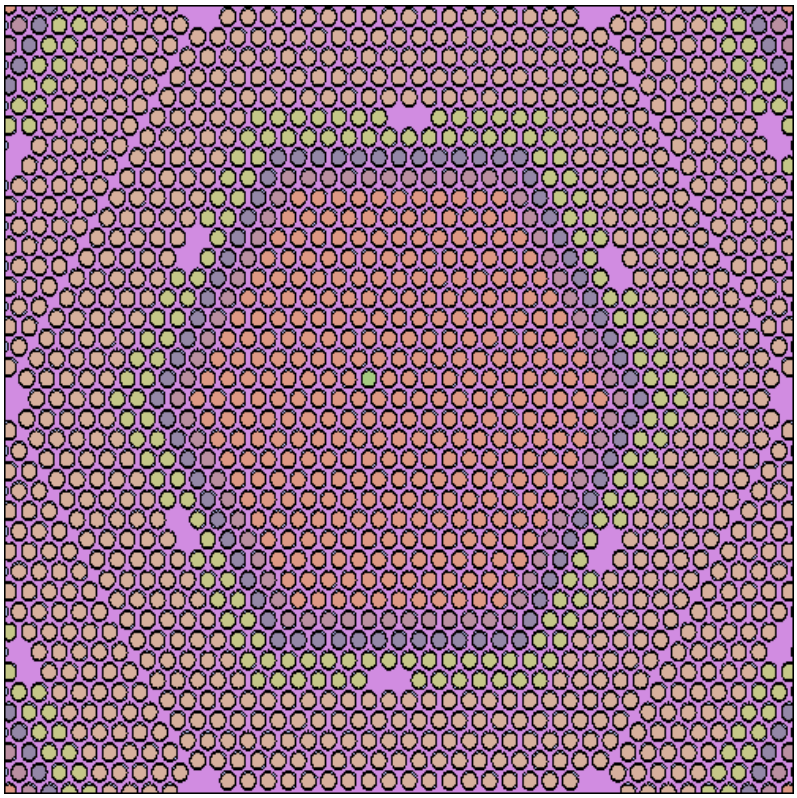

Figure 69 Geometry representation used in the input file of Serpent

For the TRANSURANUS input file the rod was divided in the same slices that corresponded to the segments in which the rod N was chopped. The simulation of the TRANSURANUS input file was more complicated, since the data available for the power history is the output electric power in MW(e). However, the peak and average linear power for the rodlet-N03 estimated and then employed for a MCNP calculation, was reported [23] (see Figure 70) and therefore used as reference for the TRANSURANUS input file. As a first step, from this linear power, the total axial power was derived (see Equation 8.1 [138]).

It must be noted that the cosine shape of this power is a very rough approximation to the real axial distribution. Indeed, it is only valid for homogenous rods. The rod N is not homogenous because on the top and on the bottom of the rod pellets of pure ThO_2 were placed. Equation 8.1 takes the maximum value at the center of the rod (z=0) and a value of zero at both extremes. However, in a homogenous rod this assumption would not be true, but in this case with the inclusion of two pellet stacks of pure ThO_2 in both extremes, a null value of the axial power is fair to assume.

Reactor Operation START (date)	Reactor Operation END (date)	Duration (days)	Single Type I Seed (MW(th))	Single Type I Seed (MWd)	based on segment mass MWd/MTM Cumulative (days)	AVERAGE 4.2046 MWd 27750.00 Seed Type 1 Rod N Segment 3 (MW(th))	MAXIMUM 6.2425 MWd 41200.00 Seed Type 1 Rod N Segment 3 (MW(th))
26-Aug-77	30-Sep-77	35	2.731274	95.5946	35.000	1.1183E-03	1.6603E-03
30-Sep-77	31-Dec-77	92	5.971203	549.3507	127.000	2.4449E-03	3.6298E-03
31-Dec-77	31-Mar-78	90	7.897081	710.7373	217.000	3.2334E-03	4.8006E-03
31-Mar-78	30-Jun-78	91	5.969611	543.2346	308.000	2.4442E-03	3.6289E-03
30-Jun-78	30-Sep-78	92	6.767031	622.5668	400.000	2.7707E-03	4.1136E-03
30-Sep-78	31-Dec-78	92	7.217013	663.9652	492.000	2.9549E-03	4.3871E-03
31-Dec-78	31-Mar-79	90	7.549443	679.4499	582.000	3.0910E-03	4.5892E-03
31-Mar-79	30-Jun-79	91	0.000000	0.0000	673.000	0.0000E+00	0.0000E+00
30-Jun-79	30-Sep-79	92	5.202659	478.6447	765.000	2.1302E-03	3.1626E-03
30-Sep-79	31-Dec-79	92	6.666736	613.3397	857.000	2.7296E-03	4.0526E-03
31-Dec-79	31-Mar-80	91	5.068303	461.2156	948.000	2.0752E-03	3.0810E-03
31-Mar-80	30-Jun-80	91	5.999137	545.9215	1039.000	2.4563E-03	3.6468E-03
30-Jun-80	30-Sep-80	92	6.289765	578.6584	1131.000	2.5753E-03	3.8235E-03
30-Sep-80	31-Dec-80	92	2.911629	267.8699	1223.000	1.1921E-03	1.7699E-03
31-Dec-80	31-Mar-81	90	6.354118	571.8706	1313.000	2.6016E-03	3.8626E-03
31-Mar-81	30-Jun-81	91	3.731881	339.6012	1404.000	1.5280E-03	2.2686E-03
30-Jun-81	30-Sep-81	92	6.338568	583.1482	1496.000	2.5953E-03	3.8531E-03
30-Sep-81	31-Dec-81	92	5.039344	463.6196	1588.000	2.0633E-03	3.0634E-03
31-Dec-81	31-Mar-82	90	5.325345	479.2810	1678.000	2.1804E-03	3.2372E-03
31-Mar-82	30-Jun-82	91	5.670859	516.0482	1769.000	2.3219E-03	3.4473E-03
30-Jun-82	30-Sep-82	92	5.467423	503.0029	1861.000	2.2386E-03	3.3236E-03
30-Sep-82	2-Dec-82	63	0.031986	2.0151	1924.000	1.3096E-05	1.9444E-05
	SUM=	1924	Total MWD=	10269.1357	MWd		
			Total U+Th metal mass*=	370063.1200	gm		
			Burnup=	27749.69	MWd/MTHM		
			Burnup=	6.48E+20	fiss/cc		

* MTHM=U+Th metal mass in UO2+ThO2 binary pellets and ThO2 steps, but not the top and bottom ThO2 reflectors.

Decay START (date)	Decay END (date)	Duration (days)	(MW(th))	(MWd)	Cumulative (days)
2-Dec-82	2-Jul-83	212	0	10269.1357	2136.000
2-Jul-83	2-Dec-83	153	0	10269.1357	2289.000
2-Dec-83	2-Jul-84	213	0	10269.1357	2502.000
2-Jul-84	2-Dec-84	153	0	10269.1357	2655.000
2-Dec-84	16-Jul-85	226	0	10269.1357	2881.000
	SUM=	2881			

Figure 70 History power used in MCNP [23] and used as reference for TRANSURANUS

$$q(z) = q_{max} cos\Big(\frac{\pi z}{L_{rod}}\Big) \tag{8.1}$$

L_{rod} is the total length of the rod and q_{max} is the maximum axial power attained at the center of the rod. Once the axial power function was obtained, the form factors were calculated as the rate of the local average power to the total average power as shown in Equation 8.2:

$$f = \frac{\frac{1}{\Delta L_{seg}} \int_{L_{inf}}^{L_{sup}} q_{max} cos(\frac{\pi z}{L_{rod}})}{\frac{1}{\Delta L_{rod}} \int_{-\frac{L_{rod}}{2}}^{\frac{L_{rod}}{2}} q_{max} cos(\frac{\pi z}{L_{rod}})} \tag{8.2}$$

where L_{seg} is the length of the segment, and L_{inf} and L_{sup} are the inferior and superior limits respectively of the segment where the form factor is calculated. The axial factors computed with Equation 8.2 for rod-N are listed in the table below :

Rod Segment	N01	N02	N03	N04	N05	N06
Length of Segment (mm)	256.03	542.75	537.74	537.69	539.57	221.46
Axial factor	0.237	0.907	1.475	1.454	0.853	0.206

Table 30 Rod segments length and axial factors for linear power rate for the fuel stack

Figure 71 helps to visualise the power axial profile of a fuel rod with the cosine function according to Equation 8.1. The axial power represented corresponds to the first time step in the simulation. The strict null value of the power on both extremes confirms the validation of this cosine function.

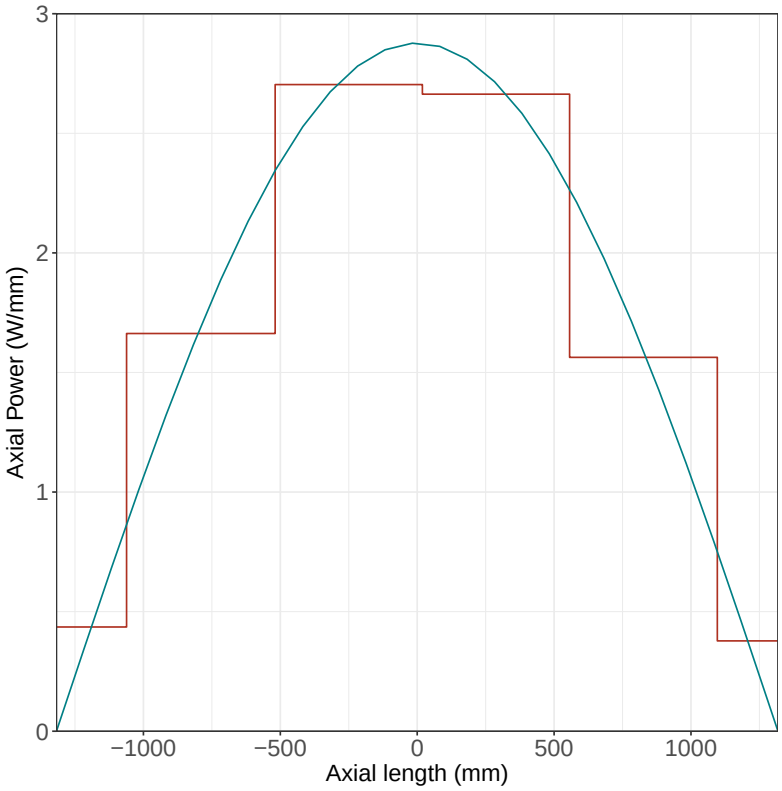

Figure 71 Axial profil introduced in TRANSURANUS (steeped) and estimated from [23] with Equation 8.1 [17]

Finally, the q_{max} was calibrated for each time step (Figure 72) to attain a 37 MWd/kg HM at EOL in the rodlet N-03 Figure 73.

The lack of information concerning axial power of the rods makes very difficult to derive the correct profile and values. The only value reported was a peak linear power in the full seed of 21.98 W/mm [21] that renders practically impossible to infer the linear power heat in a single

rod of the assembly, as was intended.

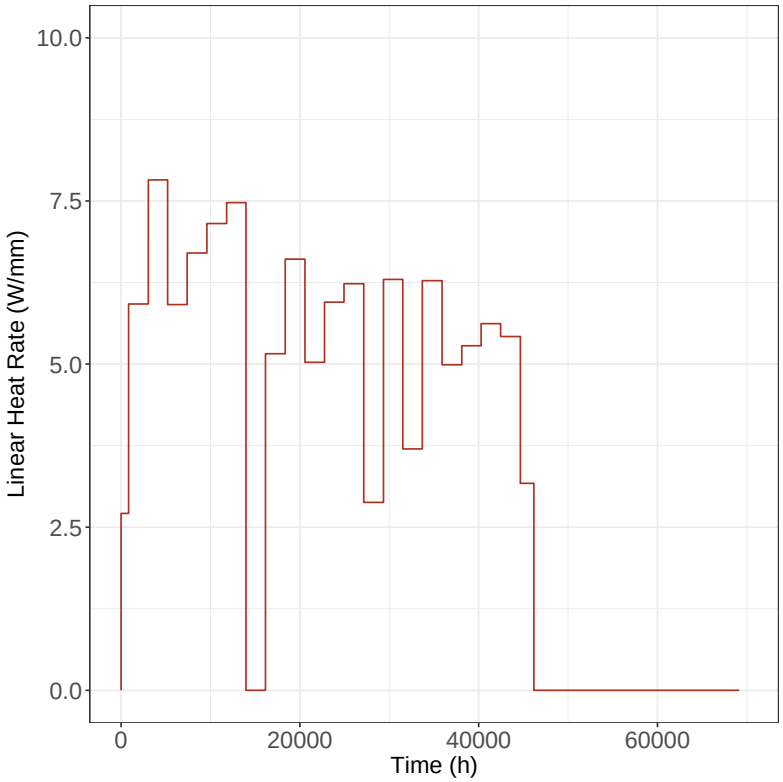

Figure 72 Linear heat power history for segment N03 [17]

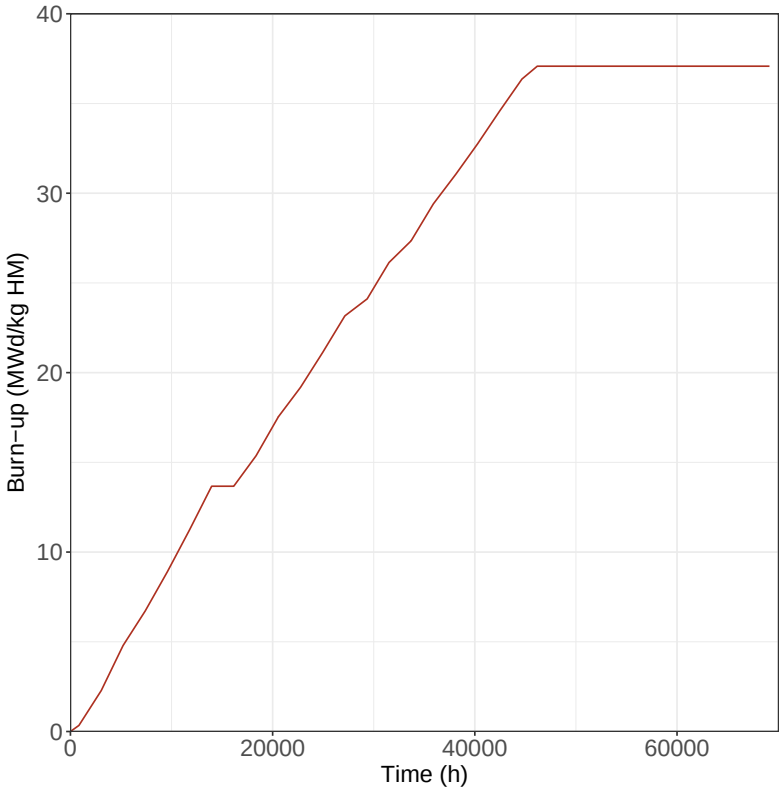

Figure 73 Burn-up evolution (in MWd/kg HM) for the segment N03 [17]

Figure 73 shows the evolution of the burn-up along the time in the fuel segment N03. The final burn-up obtained, 37 MWd/kg HM coincides to the estimated value based on the comparison of ^{137}Cs concentration performed with MCNP [23] to the experimental value measured.

Elements	LWBR	MCNP	TRANSURANUS	Serpent
^{232}Th		139.00	139.78	139.17
^{233}U	5.66	5.75	6.12	6.01
^{234}U	0.73	0.76	0.71	0.76
^{235}U	0.13	0.15	0.16	0.17
^{236}U	0.01	0.02	0.01	0.01
^{238}U	0.02	0.03	0.03	0.03
^{137}Cs	0.20	0.20	0.38	0.21
Xe	0.64	0.77	0.89	0.85
Kr	0.11	0.13	0.13	0.14

Table 31 Comparison of the quantities (in grams) measured in rodlet N03 to the different code simulations

Table 31 compares the simulated quantities of the three codes (MCNP, TRANSURANUS and Serpent) to the experimental data measured in the segment N03 for the nuclides ^{232}Th, ^{233}U, ^{234}U, ^{235}U, ^{238}U and ^{137}Cs and the elements Xe and Kr. As part of the LWBR programme [23] MCNP was coupled with ORIGEN2 to perform the nuclide depletion calculation. For each time step MCNP calculated the flux and the cross section that were then utilized by ORIGEN2 to perform the depletion calculation. This methodology was iterated until the computed concentration of ^{137}Cs was equal to the measurements. The final burn-up calculated through this iteration by MCNP was 37 MWd/kg HM that was then used for TRANSURANUS and Serpent simulations. The evaluated nuclear data libraries used by MCNP were ENDF/B-IV and ENDF/B-V [23].

The comparison of the quantities between the simulated results by the codes and the experimental data show a very good agreement. In contrast to the TRANSURANUS estimations for Thorium Cycle project, the agreement here for U is better in terms of relative difference, but still shows an overestimation of the concentration. For example the relative difference between observations and TRANSURANUS for ^{233}U and ^{234}U is 8% and 3%, when the disagreement between EPMA data and TRANSURANUS was 30% for the Thorium Cycle project. Despite of the lack of information for assessing the neutron absorption in ^{232}Th, MCNP, TRANSURANUS and Serpent show similar results for this nuclide. Moreover, as in the evaluation of the KWO (Th,Pu)O_2 rodlet, no data on the short-lived nuclide ^{233}Pa were

available. The impossibility of measuring and reporting ^{233}Pa due to its half-life neglects the assessment in TRANSURANUS (cf. Equation 4.11) of both the possible reduction of the concentration of ^{233}U and the improvement of the quantity of ^{234}U through the decay of ^{234}Pa.

Opposite to the (Th,Pu)O_2 case, TRANSURANUS presents larger differences to the measured quantities of ^{137}Cs and Xe. TRANSURANUS accounts for the isotopes ^{126}Xe and $^{128-136}$Xe, meanwhile in the Serpent simulation the isotopes ^{126}Xe, ^{130}Xe and ^{133}Xe were not included. Both in the MCNP simulation and in the measurements, the isotopes ^{126}Xe, ^{129}Xe, ^{133}Xe and ^{135}Xe were not taken into consideration either. The difference between TRANSURANUS and Serpent can be attributed to the absence in the Serpent simulation of ^{133}Xe, since the fission yield of this isotope (5.9825×10^{-2}) is not dismissible in comparison to the other isotopes of Xe. However, the overestimation of TRANSURANUS with respect to the experimental data should be proportional to the difference between TRANSURANUS and Serpent due to the absence in the measurements of ^{135}Xe. Indeed, the fission yield of ^{135}Xe (5.4715×10^{-2}) is similar to the fission yield of ^{133}Xe as reported in Table 13.

One should keep in mind, however, that the prediction of volatile elements and inert fission gas atom concentrations are prone to large errors, typically a factor of two in terms of integral values [99]. In view of these uncertainties, the results are acceptable and could explain the differences for TUBRNP and Serpent predictions in the previous section for ^{137}Cs. More precisely, the difference between TRANSURANUS and the measured value reaches almost 50% while in the case of (Th,Pu)O_2 the agreement was good. On the other side, Serpent estimations for ^{137}Cs are fair in contrast to (Th,Pu)O_2 results where the disagreement was approx. 50%.

The differences in Xe and ^{137}Cs quantities could also be attributed to the ^{233}U fission yields. Nevertheless, this would contradict the results of Subsection 6.1 and the overprediction of the Xe and Cs measurements would not be consistent with the overprediction of ^{233}U. The agreement of the Kr predictions is also acceptable, bearing in mind the low fission yields of ^{233}U for the Kr isotopes in Table 13. This may reduce the influence of the fission cross sections in the fission breeding rate. Neither in MCNP nor in the measurements the ^{80}Kr was accounted, nevertheless, its contribution to the total isotopic quantity can be neglected according to the value obtained in the Serpent simulation (3.705×10^{-8} g/cm^3). Nevertheless, a refinement of the one-group fission and radiative capture microscopic cross sections seems to be recommended in the future when more experimental data become available.

Isotopic measurements of ^{139}La and ^{148}Nd in thoria and binary pellets from the rod 0205071 that was positioned in cell Q1 in the same seed, showed a burn-up for the thoria segment of 18 MWd/kg HM and for the binary pellets (Th-U) of 49 MWd/ kg HM respectively [21]. The cell position Q1 is located in the periphery of the seed, next to the blanket as can be appreciated in Figure 67a. The burn-up of 37 MWd/ kg HM estimated with MCNP calculations through the comparison of the quantity of ^{137}Cs to experimental data contradicts the burn-up measured

through the ^{148}Nd amount in the periphery rod Q1. Since rod N was located in the middle of the module, it should have shown more burn-up than outer rods such as Q1. Nowadays, Nd is employed as burn-up monitor instead of ^{137}Cs for the reasons previously explained in Subsection 6.1.2.

8.2.2. Fission gas release

The fission gas release collected after puncturing rod N at the ANL resulted in a release ratio of 0.07%, very similar to the other measurements carried out at the same burn-up [21]. This value, together with the low burn-up attained (37 MWd/kg HM), indicates that athermal processes are the main mechanisms of fission gas release. Early simulations with TRANSURANUS showed that the Turnbull model [111], for conventional fuels, calculates a three times larger value of gas release. In order to overcome this overestimation, an extension of this model was implemented for thorium fuels as explained in Subsection 5.2.1. Figure 74 compares the Turnbull model for conventional fuels and the extension for thorium-based fuels with the value measured as part of the LWBR programme. The figure also proves that the former model simulates a factor of three folds larger than the experimental quantity.

Experiments have proven that the diffusion at BOL of fission gas atoms through the UO_2 are due to the trio-vacancy, because the atomic radius of fission gases like Xe is larger than the atomic radius of metals [133]. Recent computations done by Yun [93, 139] have shown that the energy values for Schottky trio, and Frenkel anion pairs are twice larger for ThO_2 than for UO_2. This implies that a fission fragment would have to spend more of its kinetic energy to jump from the point defect, where is placed, in a thorium oxide structure than in an uranium oxide lattice, hence making the release to outer surfaces more complicated. Additionally, the absence of 5f electrons in the thorium electronic configuration yields a strict valence of +4, meanwhile, the presence of those electrons in uranium produces three oxidation states (+4, +5 and +6). The unique valence of thorium prevents the formation of point defects due to the stronger bonds between anions and cations. The presence of stoichiometry in thoria avoids the anion vacancy formation, because the oxygen atoms tend to make chemical bonding with Xe to satisfy their electron affinity [93].

The fission gas release rate analysis carried out in the test (Th,Pu)O_2 rod segment in the Thorium Cycle project [2] showed a value of about 0.5% at a burn-up of 37.7 MWd/kg HM. Despite attaining the same burn-up, the result from the (Th,Pu)O_2 is higher than the measured value on the rod-N from Shippingport whose value was 0.07%. There are two main issues that differ from both experiments. On one side, the initial fresh fuel that was inserted in the Shippinport core was (Th,U)O_2 whereas in the Thorium Cycle the fuel studied was (Th,Pu)O_2, i.e. the initial burn-out material was ^{233}U and ^{239}Pu respectively. For the Xe and Kr isotopes, the fission yields of ^{233}U are slightly smaller than of ^{239}Pu. Therefore, less fission products are born from ^{233}U than from ^{239}Pu. The second important aspect is that the linear heat rate applied to the Shippingport rod fuel was an estimated average value of 57 W/cm, while the linear heat applied to the rodlet at KWO was c.a. 150 W/cm. Especially, this later

difference might be the reason of the disagreement in the fission gas release rate from both irradiation programmes. In the German-Brazilian cooperation programme in which (Th,U)O_2 fuel rods were irradiated at the Jülich Kernforschungsanlage fission gas realease observations were also performed. In this experiment fission gas release fractions measurements from irradiated fuels result 0.17% for a final burn-up of 9.6 MWd/kg HM with an average rod linear heat rate of 211 W/cm [57].

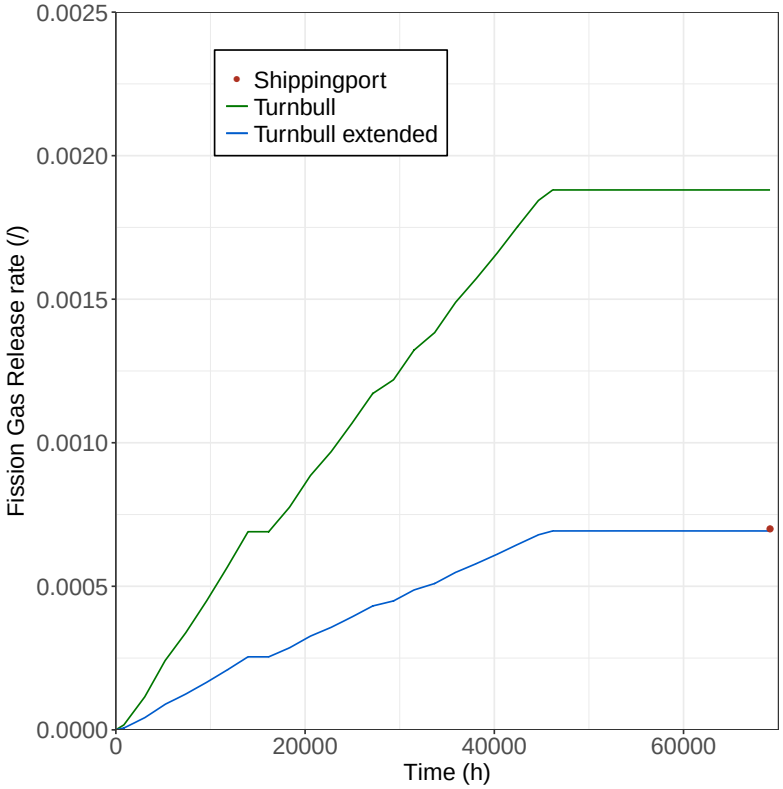

Figure 74 Comparison of the Turnbull a-thermal model with the Shippingport data point [17]

In addition, thoria and inert matrices of (Th,U)O_2 were irradiated in Halden at linear heating rates between 250 and 300 W/cm [140] with a final burn-up ranged between 17 and 30 MWd/kg HM. According to the on-line monitoring system, the fission gas release rate from the thoria and (Th,U)O_2 inert matrices was 26 and 36% respectively. These final values are higher than the values measured on the inert matrix of uranium in the same experiment whose on-line recorded values was 18% of release. Nevertheless, the fission gas release rate recorded in the rods is considerably high at the burn-up reached. Commonly, for a burn-up of 60 MWd/kg HM the fractional release is around 10% [92, 141]. This might be attributed to the very low density (around 80% of TD (Theoretical Density)) at which the pellets were manufactured that may enhance the release of fission gases [140].

It is still too soon to claim the lower release of fission gas in thorium-based fuels in comparison to the traditional fuels. Further experiments with thorium fuels irradiated in commercial reactor conditions are necessary to draw the final statement about the fission gas release in thorium.

Nevertheless, the better thermal conductivity and more stable microscopic configuration of thoria should produce, in principle, a lower gas release rate.

9

Summary and Outlook

As part of this doctoral thesis, a new TRANSURANUS version for thorium fuels was developed, implemented and validated. A quick comparison between thorium-based fuels and conventional fuels like UO_2 or MOX shows that thorium is a promising fuel for the nuclear industry. The well-distributed abundance throughout the Earth crust of thorium ore would make this fuel less dependent on speculations and territorial conflicts.

As a first step, a review of the material properties was done: elasticity constant, Poisson's ratio, strain due to swelling, thermal strain, thermal conductivity, creep rate, yield stress, rupture strain, heat capacity, density, solidus-liquidus melting temperature, heat of melting, emissivity and fraction of heavy metals for (Th,U)O_2 and (Th,Pu)O_2. In most of the cases the Vergard's law or Neumann-Kopp's law for heat capacity was applied as interpolation between propeties for pure ThO_2, PuO_2 and UO_2 oxides. Special attention was paid to thermal conductivity. This property is crucial for the behaviour of a fuel rod, nonetheless, the rigorous experimental correlation that implicitly depends on the burn-up, porosity and phonon temperature used already for MOX and UO_2, was not yet studied for thorium. Lucuta's model as the thermal conductivity degrades by factorizing those previously mentioned fission effects, was therefore implemented. In cases where neither ThO_2 nor PuO_2 are not available, UO_2 was used, for example for the creep rate.

In a second step, the TRANSURANUS burn-up model TUBRNP has been extended to perform thorium-based fuel study cases. The set of Bateman's equations for the thorium cycle were implemented as well as the bred of ^{235}U through neutron capture by ^{234}U in the first place. To complete the depletion set of equations, radial power profile functions have been analytically derived from neutronic Serpent simulations for ^{232}Th and ^{240}Pu that accounts for the absorption in the epithermal range of neutrons, as well as the calculations for the one-group effective cross sections. The TUBRNP development was completed by including the accumulative fission yields for the most important fission isotopes of Nd, Xe, Kr and Cs.

In a third step, the TRANSURANUS fission gas release treatment was considered. It is divided into three main contributions: athermal, intra-granular and inter-granular. The experimental athermal model implemented in TRANSURANUS was extended in the course of this work to consider thorium-based fuels by modifying the slope of its linear model. The modification of the intra-granular model that accounts for the diffusion of fission gases within the grain has been carried out by including a diffusion coefficient for thorium fuels after an extensive review of the literature. Finally, a review of the parameters involved in the simplified

inter-granular model was carried out, concluding that no extension was required since the value of these parameters are similar to UO_2.

The first step towards its testing for (Th,Pu)O_2 fuel types relies on experimental data from a sample with 38.8 MWd/kg HM average burn-up irradiated in KWO in the frame of the Thorium Cycle project of the European Commission. The normalised radial profiles of the elements Th, U, Pu, Nd, Cs and Xe depicted an excellent agreement with EPMA measurements, proving the accuracy in the derivation of the absorption radial functions. Moreover, there is a fair agreement between calculated and measured radially averaged concentrations of these elements. Nevertheless, attention must be paid to the U profile, whose relative differences in relation to EPMA data are considerable. This confirms similar observations about the radial averaged concentrations obtained with four codes used in a benchmark as part of the Thorium Cycle project in the open literature.

For (Th,U)O_2 fuels the first testing of TUBRNP was performed by comparing the calculations to the isotopic concentrations measured by destructive analysis in a segment with an average burn-up of 37 MWd/kg HM, that was sheared from a rod irradiated in the Shippingport power plant in 1982. In this case the U isotopes showed better agreements than in the (Th,Pu)O_2 case, whereas the calculated fission product concentrations of ^{137}Cs and Xe presented larger but still acceptable differences. Nevertheless, more experimental data need to be obtained and analysed by means of TUBRNP and Serpent before being able to draw definite conclusions. More recent data and up-to-date experimental techniques should also contribute to improve the accuracy of the results. From the same rod, the fission gas release rate measured after puncture was also compared to TRANSURANUS. The results showed a good agreement. According to lattice structure analysis and thermal conductivity comparisons, thorium fuels tend to release less fission gases, which is in line with what was investigated. Nevertheless, the irradiation conditions applied in the Shippingport reactor were not entirely identical to other U-MOX fuel cases to declare the lower release rate in thorium-based fuels at same burn-up.

The differences observed for U in (Th,Pu)O_2 and for ^{137}Cs and Xe in (Th,U)O_2 might also be attributed to the uncertainty in the computation of the one-group effective cross sections obtained with Serpent. This could be further analysed by means of a sensitivity analysis with other nuclear data libraries. In the present thesis the evaluated nuclear library employed was JEFF-3.1.1 whereas in the Shippingport programme and in the Thorium Cycle (TC) benchmark the nuclear libraries utilized were ENDF/B-IV until ENDF/B-VII [27, 23].

A first contribution to validation of the full TRANSURANUS version for (Th,Pu)O_2 developed in this thesis was carried out by comparing the on-line central temperature obtained from the two OMICO rods to the TRANSURANUS simulations. The relative differences (around 14 and 10%) between TRANSURANUS and measurements at full power in both rods showed that TRANSURANUS is in a good track for becoming a thorium fuel performance code with

the same level of accuracy of 9% achieved in the parallel analysis of the MOX rod G_i as part of the same OMICO programme. However, a sensitivity analysis was carried out in order to understand the relative difference deviation between both fuels by modifying the initial porosity to 6%, the swelling due to fission products to 0.32, 0.5 and 0.75% as recommended by Spino [58] and, eventually, disabling the relocation model in the TRANSURANUS input file. The result of this sensitivity analysis in both Th-MOX rods suggested the necessity of changing the swelling rate proposed in the OMICO report and adopted in TRANSURANUS in a first place. Those values may be utilized as reference for future experimental research on the fuel swelling in thorium materials. The TRANSURANUS assessment of the OMICO rods was completed by comparing the gap width between pellet and cladding reported in rods B_i and G_i at the end of irradiation to the values obtained from the sensitivity analysis. There has been a good agreement displayed in the comparison for the cases 'Swelling 0.75%' and 'Densification' for rods B_i and G_i respectively. Nonetheless, further examinations on rods B_i and G_i exhibited an apparent porosity of 20 and 30%, which is very unusual at the burn-up achieved. A dislodgement of powder grains attributed to the polishing and sintering steps in the pellet fabrication may explain this porosity showed on the periphery. This brittleness observed in both rods should raise caution in using these data.

In general two main conclusions from this thesis can be stated: according to the thermo-mechanical and neutronic characteristic, thorium can be seen as a promising nuclear fuel that can substitute or complement U-MOX-based fuels in LWR. Nevertheless, further experiments must be performed to attain the same level of knowledge as already achieved for uranium fuels. An enhancement in the expression of the thermal conductivity concerning the inclusion of the burn-up, temperature and other effects in the terms A and B corresponding to phonon heat transport would allow to substitute Lucuta's model adopted for thorium as a first approximation. Further elastic-plastic experiments must be carried out in thorium to improve in first place the yield stress and rupture strain whose correlation were derived from a diverse range of different and non-related samples. A deeper study in the Young's modulus above 1200 K must be done to check and prove the shortfall mentioned by Spinner [51]. And finally, the parameters in Solomon's creep model [69, 70, 68] for pure ThO_2 and PuO_2 should be fitted to experimental work. The full analysis of the thermo-mechanical properties will be completed with the optical experiments for the emissivity in thorium dioxide, especially at high temperatures. Regarding the fission gas release, further irradiation experiments should be done at the same conditions published for traditional (U,Pu)O_2 fuels to analyse not only the release of fission gases but also the swelling due to fission products.

The second conclusion drawn is the success in the extension of TRANSURANUS to thorium-based fuels. The versatility shown in the usage of Serpent to derive TRANSURANUS can be utilized in the future for a coupling among both codes. A revision of the averaged value for the uranium element in (Th,Pu)O_2 cases needs to be done because of its large discrepancy. The comparisons of the current result to a sensitivity analysis with other nuclear data libraries like ENDF or JAENDL might improve this disagreement and refine the differences in the other

elements or nuclides. A further TRANSURANUS simulation of the extension of the OMICO irradiation programme, THOMOX, for the non-instrumented rods will allow to study the fission gas release parameters already implemented for thorium cases. The irradiation that is currently carried out in the Halden reactor of (Th,U)O_2 and (Th,Pu)O_2 pellets manufactured by ThorEnergy will help in a more detailed analysis of the simulation of the thorium material properties under LWR irradiation conditions with TRANSURANUS. In the meantime attention should also be paid to code coupling. More precisely, as mentioned above, several codes have been coupled, for example MCNP-Origen2 for the LWBR Shippingport programme or the interface EET in the Thorium Cycle benchmark. In the present work both the spectrum-averaged cross sections and the radial shape functions were derived from Serpent and then used in TUBRNP, which can serve as a guideline to couple both codes in the frame of the ESSANUF project of the European Commission.

A

Approximation to diffusion

A nuclear reactor is a system in which fission reactions are maintained and controlled to produce energy. In this system, the neutrons undergo fission reactions when they collide with the heavy nuclides that form the nuclear fuel. Further reactions may happen when neutrons interact with the rest of materials like coolant, moderator or cladding. The behaviour of a reactor is hence driven by the distribution of neutrons. The Boltzmann transport equation is the most fundamental and rigorous mathematical model that describes the distribution of neutrons and their interactions with the environment [142]. This section aims to explain the process of deriving the diffusion equation from the Boltzmann transport equation by accounting several assumptions and simplifications. The neutron diffusion equation is finally utilized in the Transuranus burn-up model, TUBRNP.

The completed Boltzmann equation is (for further details about how is derived see [143]):

$$\begin{aligned}\frac{1}{v(E)}\frac{\partial\Psi(\vec{r},E,\vec{\Omega},t)}{\partial t}+\vec{\Omega}grad\Psi(\vec{r},E,\vec{\Omega},t)+\Sigma_t(\vec{r},E,t)\Psi(\vec{r},E,\vec{\Omega},t)=\\ \int_{4\pi}\int_0^{\infty}\Sigma_s(\vec{r},E'\rightarrow E,\vec{\Omega}'\rightarrow\vec{\Omega},t)\Psi(\vec{r},E',\vec{\Omega}',t)dE'd\vec{\Omega}'\\ +\frac{\aleph_p(E)}{4\pi}\sum_i(1-\beta^i)\int_{4\pi}\int_0^{\infty}\upsilon\Sigma_f^i(\vec{r},E',t)\Psi(\vec{r},E',\vec{\Omega}',t)dE'd\vec{\Omega}'\\ +\sum_l^7\aleph_l(E)\lambda_l C_(\vec{r},t)+q_{ext}(\vec{r},E,\vec{\Omega},t)\end{aligned}\tag{A.1}$$

where the variables $\vec{r}$, E, $\vec{\Omega}$, t stand for the vector of the position that in a fuel pellet is in cylindric coordinates, the energy of incident neutrons, the vector of the direction of the particle ($\vec{v}=v\vec{\Omega}$) and time respectively. $\Psi(\vec{r},E,\vec{\Omega},t)$ is the angular flux which is an scalar magnitude. $v(E)$ represents the velocity of neutrons previously mentioned and $\Sigma_t(\vec{r},E,t)$ is the total macroscopic cross section. The total macroscopic cross section is the sum of all the reaction cross sections, such as fission, elastic scattering, (n,2n), radiative capture and so on. $\Sigma_s(\vec{r},E'\rightarrow E,\vec{\Omega}'\rightarrow\vec{\Omega},t)$ is the differential elastic scattering macroscopic cross section and represents the probability that a neutron with an initial energy E' and direction, $\vec{\Omega}'$ scatters elastically with an outcome energy and direction of E and $\vec{\Omega}$, $\aleph_p(E)$ is the spectrum of the prompt fission neutrons, β^i is the fraction of fission neutrons which is delayed (the superscript i refers to the fissionable nuclide i-th), $\Sigma_f^i(\vec{r},E',t)$ is the macroscopic fission cross section, υ states the average number of neutrons born from the fission (for example for ^{239}Pu this number is 2.49), $\aleph_l(E)$ is the spectrum of delayed neutrons, with the subscript l referring the precursor type, λ_l represents the decay constant of the precursor nuclides that produce a

delayed neutron, $C_(\vec{r},t)$ means the concentration of the precursor l and $q_{ext}(\vec{r},E,\vec{\Omega},t)$ is an external source of neutrons. In a nuclear reaction the nucleus is not affected by the direction of the collision of neutrons, just in scattering reactions the scattering angle must be taken into consideration. Figure 75 displays the system in which the neutron is analyzed

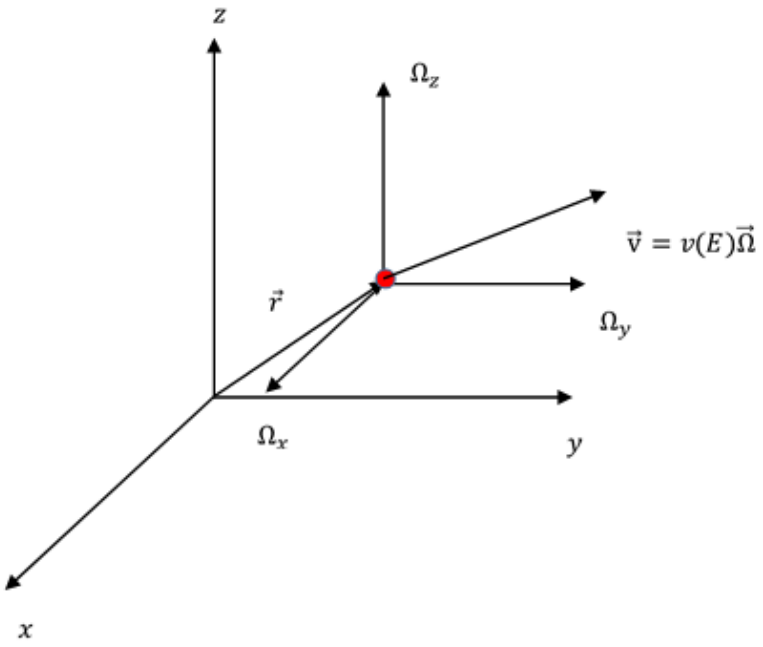

Figure 75 Representation of the neutron in the system

The scalar flux $\phi(\vec{r},E,t)$ is an scalar variable resulted of the integration of the angular flux over all directions (Equation A.2). This scalar variable is more important since a ceramic material does not show any preferential direction, i.e. the material is isotropic. Only when scattering reactions are studied the angular flux must be considered due to the importance of the vector of directions $\vec{\Omega}$:

$$\phi(\vec{r},E,t) = \int_{4\pi} \Psi(\vec{r},E,\vec{\Omega},t)d\vec{\Omega} \tag{A.2}$$

Another important quantity is the current, $\vec{J}(\vec{r},E,t)$ which is defined as:

$$\vec{J}(\vec{r},E,t) = \int_{4\pi} \vec{J}(\vec{r},E,\vec{\Omega},t)d\vec{\Omega} = \int_{4\pi} \vec{\Omega}\Psi(\vec{r},E,\vec{\Omega},t)d\vec{\Omega} \tag{A.3}$$

The first simplification assumed is that Equation A.1 does not depend on the time, whose immediately consequences are two. On one side, the time-dependent term can be neglected

$$\frac{1}{v(E)}\frac{\partial\Psi(\vec{r},E,\vec{\Omega},t)}{\partial t} \approx 0 \tag{A.4}$$

and on the other side, delayed neutrons may have no effect in the flux since they are the

result of the radioactive decay of certain unstable fission products.

$$\sum_{l}^{7} \aleph_l(E)\lambda_l C_(\vec{r},t) \approx 0, \beta^i \approx 0$$

The external source of neutrons $q_{ext}(\vec{r},E,\vec{\Omega},t)$ is also neglected to simplify Equation A.1. Therefore the Boltzmann equation can be simplified as:

$$\begin{aligned} \vec{\Omega} grad\Psi(\vec{r},E,\vec{\Omega}) + \Sigma_t(\vec{r},E)\Psi(\vec{r},E,\vec{\Omega}) = \\ \int_{4\pi}\int_0^\infty \Sigma_s(\vec{r},E'\to E,\vec{\Omega}'\to\vec{\Omega})\Psi(\vec{r},E',\vec{\Omega}')dE'd\vec{\Omega}' \\ + \int_{4\pi}\int_0^\infty \frac{\upsilon\aleph_p(E)}{4\pi}\Sigma_f(\vec{r},E')\Psi(\vec{r},E',\vec{\Omega}')dE'd\vec{\Omega}' \end{aligned} \tag{A.5}$$

As can be seen, the fission source can be integrated over the angular vector, simplifying the equation to

$$\begin{aligned} \vec{\Omega} grad\Psi(\vec{r},E,\vec{\Omega}) + \Sigma_t(\vec{r},E)\Psi(\vec{r},E,\vec{\Omega}) = \\ \int_{4\pi}\int_0^\infty \Sigma_s(\vec{r},E'\to E,\vec{\Omega}'\to\vec{\Omega})\Psi(\vec{r},E',\vec{\Omega}')dE'd\vec{\Omega}' \\ + \int_0^\infty \frac{\upsilon\aleph_p(E)}{4\pi}\Sigma_f(\vec{r},E')\phi(\vec{r},E')dE' \end{aligned} \tag{A.6}$$

In the next step, a strict linearity of the angular flux is going to be assumed, i.e. the angular flux weakly depends on angular variable

$$\Psi(\vec{r},E,\vec{\Omega}) \approx A(\vec{r},E) + \vec{\Omega}\vec{B}(\vec{r},E) \tag{A.7}$$

where $A(\vec{r},E)$ and $\vec{B}(\vec{r},E)$ are two parameters that are derived from the definitions of scalar flux (Equation A.2) and current (Equation A.3) respectively, according to [142, 138].

$$\begin{aligned} \int_{4\pi}\Psi(\vec{r},E,\vec{\Omega})d\vec{\Omega} = \\ \int_{4\pi}A(\vec{r},E)d\vec{\Omega} + \int_{4\pi}\vec{\Omega}\vec{B}(\vec{r},E)d\vec{\Omega} = \\ \phi(\vec{r},E) = 4\pi A(\vec{r},E) + \vec{B}(\vec{r},E)\underbrace{\int_{4\pi}\vec{\Omega}d\vec{\Omega}}_{0} \end{aligned} \tag{A.8}$$

$$\begin{aligned} \vec{J}(\vec{r},E) = \int_{4\pi}\vec{J}(\vec{r},E,\vec{\Omega})d\vec{\Omega} = \int_{4\pi}\vec{\Omega}\Psi(\vec{r},E,\vec{\Omega})d\vec{\Omega} = \\ \underbrace{\int_{4\pi}\vec{\Omega}A(\vec{r},E)d\vec{\Omega}}_{0} + \int_{4\pi}\vec{\Omega}\vec{\Omega}\vec{B}(\vec{r},E)d\vec{\Omega} = \\ \vec{B}(\vec{r},E)\int_{4\pi}\vec{\Omega}\vec{\Omega}d\vec{\Omega} = \frac{4\pi}{3}\vec{B}(\vec{r},E) \end{aligned} \tag{A.9}$$

Inserting Equation A.8 and A.9 in Equation A.7 the approximation of the angular flux to linearly

anisotropy is attained

$$\Psi(\vec{r}, E, \vec{\Omega}) \approx \frac{1}{4\pi}[\phi(\vec{r}, E) + 3\vec{\Omega}\vec{J}(\vec{r}, E)] \tag{A.10}$$

Now the momentum order-zero, $\int_{4\pi} d\vec{\Omega}$ is applied to Equation A.6. In first place the convection term is converted as

$$\int_{4\pi} \vec{\Omega} grad\Psi(\vec{r}, E, \vec{\Omega}) d\vec{\Omega} = \int_{4\pi} div\vec{\Omega}\Psi(\vec{r}, E, \vec{\Omega}) d\vec{\Omega} = \int_{4\pi} div\vec{J}(\vec{r}, E, \vec{\Omega}) d\vec{\Omega} = div\vec{J}(\vec{r}, E) \tag{A.11}$$

The removal term is transformed as

$$\int_{4\pi} \Sigma_t(\vec{r}, E)\Psi(\vec{r}, E, \vec{\Omega}) d\vec{\Omega} = \Sigma_t(\vec{r}, E) \int_{4\pi} \Psi(\vec{r}, E, \vec{\Omega}) d\vec{\Omega} = \Sigma_t(\vec{r}, E)\phi(\vec{r}, E) \tag{A.12}$$

For the scattering term

$$\begin{gathered}\int_{4\pi} \left(\int_{4\pi} \int_0^\infty \Sigma_s(\vec{r}, E' \to E, \vec{\Omega}' \to \vec{\Omega})\Psi(\vec{r}, E', \vec{\Omega}') dE' d\vec{\Omega}' \right) d\vec{\Omega} = \\ \int_{4\pi} \int_0^\infty \Sigma_s(\vec{r}, E' \to E)\Psi(\vec{r}, E', \vec{\Omega}') dE' d\vec{\Omega}' = \\ \int_0^\infty \Sigma_s(\vec{r}, E' \to E)\phi(\vec{r}, E') dE'\end{gathered} \tag{A.13}$$

And finally the fission term is transformed to

$$\int_{4\pi} \int_0^\infty \frac{\upsilon \aleph_p(E)}{4\pi} \Sigma_f(\vec{r}, E')\phi(\vec{r}, E') dE' d\vec{\Omega} = \int_0^\infty \upsilon \aleph_p(E)\Sigma_f(\vec{r}, E')\phi(\vec{r}, E') dE' \tag{A.14}$$

Gathering the four terms integrated over all directions, Equations A.11, A.12, A.13 and A.14, the momentum-zero Boltzmann equation is

$$\begin{gathered}div\vec{J}(\vec{r}, E) + \Sigma_t(\vec{r}, E)\phi(\vec{r}, E) = \\ \int_0^\infty \Sigma_s(\vec{r}, E' \to E)\phi(\vec{r}, E') dE' + \int_0^\infty \upsilon \aleph_p(E)\Sigma_f(\vec{r}, E')\phi(\vec{r}, E') dE'\end{gathered} \tag{A.15}$$

The next step is to do the same, but in this case, the neutronic transport equation was multiplied by the angular variable and integrated over all directions. This is also called the application of the momentum order-one $\int_{4\pi} \vec{\Omega} d\vec{\Omega}$.

The convection term is transformed:

$$\begin{gathered}\int_{4\pi} \vec{\Omega}[\vec{\Omega} grad\Psi(\vec{r}, E, \vec{\Omega})] d\vec{\Omega} = \int_{4\pi} \vec{\Omega}\vec{\Omega} grad\Psi(\vec{r}, E, \vec{\Omega}) d\vec{\Omega} \approx \\ \frac{1}{4\pi} \int_{4\pi} \vec{\Omega}\vec{\Omega} grad[\phi(\vec{r}, E) + 3\vec{\Omega}\vec{J}(\vec{r}, E)] d\vec{\Omega} = \\ \frac{1}{4\pi} \int_{4\pi} \vec{\Omega}\vec{\Omega} grad\phi(\vec{r}, E) d\vec{\Omega} + \frac{3\vec{J}(\vec{r}, E)}{4\pi} \int_{4\pi} \vec{\Omega}\vec{\Omega}\vec{\Omega} d\vec{\Omega} = \\ \frac{1}{3} grad\phi(\vec{r}, E)\end{gathered} \tag{A.16}$$

In Equation A.16 the approximation of the angular flux to linear dependence of the angular

variable explained in Equation A.10 was applied to compute the integrals.

On the other side, the removal term after applying the momentum order-1 remains as:

$$\int_{4\pi} \vec{\Omega}[\Sigma_t(\vec{r},E)\Psi(\vec{r},E,\vec{\Omega})]d\vec{\Omega} = \Sigma_t(\vec{r},E)\int_{4\pi} \vec{\Omega}\Psi(\vec{r},E,\vec{\Omega})d\vec{\Omega} = \Sigma_t(\vec{r},E)\vec{J}(\vec{r},E) \quad \text{(A.17)}$$

The term of scattering is in this way transformed:

$$\int_{4\pi} \vec{\Omega}\left[\int_{4\pi}\int_0^\infty \Sigma_s(\vec{r},E'\to E,\vec{\Omega}'\to\vec{\Omega})\Psi(\vec{r},E',\vec{\Omega}')dE'd\vec{\Omega}'\right]d\vec{\Omega} =$$
$$\int_{4\pi}\int_0^\infty \left(\int_{4\pi}[\vec{\Omega}\Sigma_s(\vec{r},E'\to E,\vec{\Omega}'\to\vec{\Omega})]d\vec{\Omega}\right)\Psi(\vec{r},E',\vec{\Omega}')dE'd\vec{\Omega}' = \quad \text{(A.18)}$$

If now Equation A.18 is multiplied twice by the direction vector before the scattering collision $\vec{\Omega}'$, it is attained:

$$\int_{4\pi}\int_0^\infty \left(\int_{4\pi}[\vec{\Omega}'\vec{\Omega}\Sigma_s(\vec{r},E'\to E,\vec{\Omega}'\to\vec{\Omega})]d\vec{\Omega}\right)\vec{\Omega}'\Psi(\vec{r},E',\vec{\Omega}')dE'd\vec{\Omega}' =$$
$$\int_0^\infty \left[\int_{-1}^1 \mu\Sigma_s(\vec{r},E'\to E,\mu)d\mu\right]\left[\int_{4\pi}\vec{\Omega}'\Psi(\vec{r},E',\vec{\Omega}')dE'd\vec{\Omega}'\right]dE' =$$
$$\int_0^\infty \Sigma_{sL}(\vec{r},E'\to E)\vec{J}(\vec{r},E')dE' \quad \text{(A.19)}$$

Figure 76 shows the interpretation of the term μ which is the scattering cosine $cos\theta$ as the scalar multiplication of the incident angular vector $\vec{\Omega}'$ and the outcome angular vector after the scattering collision $\vec{\Omega}$. The variable μ can take values between -1 (180°) and 1 (0°).

Figure 76 Representation of a elastic collision with the cosine of the scattering angle θ, μ calculated as the scalar product of the incident direction vector $\vec{\Omega}'$ times the outcome direction vector $\vec{\Omega}$

However, the term of fission source is neglected as can be appreciated in Equation A.20

$$\int_{4\pi}\vec{\Omega}\int_0^\infty \frac{\upsilon\aleph_p(E)}{4\pi}\Sigma_f(\vec{r},E')\phi(\vec{r},E')dE'd\vec{\Omega} = \int_0^\infty \frac{\upsilon\aleph_p(E)}{4\pi}\Sigma_f(\vec{r},E')\phi(\vec{r},E')dE'\int_{4\pi}\vec{\Omega}d\vec{\Omega} = 0 \quad \text{(A.20)}$$

As was done before, all the terms in which the momentum order-1 was applied, are gathered

again (see Equations A.16, A.17, A.19 andA.20). The following expression is obtained:

$$\frac{1}{3}grad\phi(\vec{r},E)+\Sigma_t(\vec{r},E)\vec{J}(\vec{r},E)= \int_0^\infty \Sigma_{sL}(\vec{r},E'\rightarrow E)\vec{J}(\vec{r},E')dE' \tag{A.21}$$

Here $\Sigma_{sL}(\vec{r},E'\rightarrow E)$ is the macroscopic elastic scattering cross section in the laboratory system. In case that in the laboratory system (subscript L) there is isotropic scattering, this term is equal to zero $\Sigma_{sL}(\vec{r},E'\rightarrow E)=0$. This approximation is not good for light nuclei therefore, can not be used when there would be a reactor with moderator. With this critical approximation the Equations A.15 and A.21 are simplified:

$$div\vec{J}(\vec{r},E)+\Sigma_t(\vec{r},E)\phi(\vec{r},E)=\int_0^\infty \upsilon\aleph_p(E)\Sigma_f(\vec{r},E')\phi(\vec{r},E')dE' \tag{A.22}$$

$$\frac{1}{3}grad\phi(\vec{r},E)+\Sigma_t(\vec{r},E)\vec{J}(\vec{r},E)=0 \tag{A.23}$$

A second strong simplification that makes the work with the equations simpler, is the assumption that the macroscopic cross sections do not depend on the position $\vec{r}$. This is not true again because a macroscopic cross section of a certain nuclide is defined as the multiplication of the microscopic cross sections (that only depends on the incident neutron energy (E) times the concentration the mentioned nuclide that effectively depends on the position. From this last equation, the first Fick's law can be derived:

$$\vec{J}(\vec{r},E)=-\frac{1}{3\Sigma_t(E)}grad\phi(\vec{r},E) \tag{A.24}$$

Being $\frac{1}{3\Sigma_t(E)}$ the diffusion coefficient $D(E)$.

Inserting the first Fick's law derived from the momentum order-1, Equation A.24 in the Equation A.22 obtained from the application of the momentum order-0 to Boltzmann transport equation

$$-lap(D(E)\phi(\vec{r},E))+\Sigma_t(E)\phi(\vec{r},E)=\int_0^\infty \upsilon\aleph_p(E)\Sigma_f(E')\phi(\vec{r},E')dE' \tag{A.25}$$

The definition of one-group, spectrum average of neutron incident energy is:

$$\sigma=\frac{\int_0^\infty \sigma(E)\phi(E)dE}{\int_0^\infty \phi(E)dE}=\frac{\int_0^\infty \sigma(E)\phi(E)dE}{\phi} \tag{A.26}$$

where ϕ is the scalar flux integrated over all energies, i.e. one energy group flux. In this case the diffusion coefficient is going to be considered as a cross section to apply the spectrum-average equation. Applying this to Equation A.25, the diffusion approximation is eventually

attained:

$$\int_0^\infty -lap(D(E)\phi(\vec{r},E))dE + \int_0^\infty \Sigma_t(E)\phi(\vec{r},E)dE = \int_0^\infty \int_0^\infty \upsilon\aleph_p(E)\Sigma_f(E')\phi(\vec{r},E')dE'dE$$
$$-lap\int_0^\infty (D(E)\phi(\vec{r},E))dE + \int_0^\infty \Sigma_t(E)\phi(\vec{r},E)dE = \int_0^\infty \int_0^\infty \upsilon\aleph_p(E)\Sigma_f(E')\phi(\vec{r},E')dE'dE$$
$$-lap(D\phi(\vec{r})) + \Sigma_t\phi(\vec{r}) = \int_0^\infty \upsilon\aleph_p(E)dE \int_0^\infty \Sigma_f(E')\phi(\vec{r},E')dE'$$
$$-lap(D\phi(\vec{r})) + \Sigma_t\phi(\vec{r}) = \upsilon\aleph_p\Sigma_f\phi(\vec{r}) \tag{A.27}$$

The total cross section is the sum of the fission cross section plus the absorption cross section.

$$-lap(D\phi(\vec{r})) = \Sigma_a\phi(\vec{r}) \tag{A.28}$$

Assuming symmetry in the axial and polar coordinate in a cylindrical system the $\vec{r}$ is simplified to just r. Since in the particular cases that are going to be studied the type of reactor is thermal, the macroscopic cross section Σ_a is only regarded in the thermal range of incident neutrons $\Sigma_a \rightarrow \Sigma_{a,therm}$

$$-lap\phi(r) = \frac{\Sigma_{a,therm}}{D}\phi(r) \tag{A.29}$$

A further step will entail the approximation of Σ_t to the elastic scattering cross section Σ_s, i.e. low absorption in the material. However, this step can only be applied in the moderator and structural materials where there is not absorption, while in the fuel as well as in the control rods, this assumption can not be carried out because the strong neutron absorption.

The linear spatial variation of the neutron distribution is only satisfied few mean free paths away from the boundary of large homogeneous media with relatively uniform source distributions [144].

Eventually, the third most important simplification, the isotropic scattering is only fulfilled by heavy atoms of mass. Nevertheless, the diffusion approximation provides a good approximation of the neutron behaviour in a very easy way. In case the the diffusion approximation is not valid, statistic approaches like Monte Carlo can overcome those limitations.

The first boundary condition of Equation A.29 is the continuity of the flux in the centerline of the pellet $\phi(r) < \infty$. The second boundary conditions depends on the scenario of the problem. The simplest scenario is the assumption that the pellet is surrounded by a vacuum or non-reflecting region. This particular case gives rise to the approximate vacuum boundary condition of zero neutron flux at a distance λ_{extrap} outside the physical boundary at x = a, or

$$\phi(a + \lambda_{extrap}) = \phi(aex) = 0 \tag{A.30}$$

where λ_{extrap} is $\lambda_{extrap} = 0.7104\lambda_{tr}$ calculated from the neutron transport theory. λ_{tr} is transport free mean path that is the inverse of the macroscopic transport cross section.

B

The improved Speight model of diffusion of fission gases in a spherical grain

The exchange of vacancies between the bubble and the solid makes the bubble to undergo Brownian motion [3, 103, 102, 101] and consequently the diffusion of the bubble through the grain is driven by the volume diffusion. With this last assumption and in stationary conditions in the reactor the diffusion of gas bubbles follows the second Fick's law in spherical coordinates:

$$\frac{\partial N_b(r,t)}{\partial t} = D_b lap N_b(r,t) \tag{B.1}$$

$N_b(r,t)$ is the local concentration of bubbles and D_b is the bubble diffusion coefficient. The local concentration of gases within the bubbles is defined as follows:

$$C_b(r,t) = m(r,t)N_b(r,t) \tag{B.2}$$

where $m(r,t)$ is the number of gas atoms per bubble. If now the number of gas atoms per bubble is spatially independent the and the intragranular bubbles are considered to be saturated, i.e. the number of gas atoms per bubble is constant and uniform [114] $m(r,t)$ becomes a constant that can be easily calculated through the modified Van der Waals equation of gases assuming that the hydrostatic pressure around the bubble is neglected in comparison with the surface tension.

The gas concentration in solution and within bubbles may be described by the following partial differential equations:

$$\begin{aligned}\frac{\partial C_s(r,t)}{\partial t} &= D_s lap C_s(r,t) - g(r,t)C_s(r,t) + b(r,t)C_b(r,t) + \beta_s \\ \frac{\partial C_b(r,t)}{\partial t} &= D_b lap C_b(r,t) + g(r,t)C_s(r,t) - b(r,t)C_b(r,t) + \beta_b\end{aligned} \tag{B.3}$$

where $C_s(r,t)$ is the local concentration of gas existing as single gas atoms in the lattice D_s is the single diffusion atom coefficient respectively, and β_s and β_b are the source terms that represent the effect in the first case the gas atom generation and in the second case the heterogeneous bubble nucleation [3], both from fission events, $g(r,t)$ is the probability per unit time of gas atoms in solution being captured by a bubble. Olander [3] and [103] state that $g(r,t)$ can be calculated:

$$g(t) = 4\pi \bar{R}_b D_s \bar{N}_b \tag{B.4}$$

where $\bar{N}_b$ and $\bar{R}_b$ are the average radius and number density of the intra-granular bubbles.

Thus, the trapping rate is independently of the geometry. $b(r,t)$ is the probability per unit time of a gas atom in bubble being re-dissolved. According to[3] and [114] $b(r,t)$ is directly proportional to the fission rate, $\dot{F}$; making the re-solution rate radially independent:

$$b(t) \propto \dot{F} \tag{B.5}$$

The total concentration of fission gas atoms within the grain, $C_t(r,t)$, is defined as the sum of the gas concentration solved in the material, $C_s(r,t)$ and trapped in bubbles in the grain, $C_b(r,t)$:

$$C_t(r,t) = C_s(r,t) + C_b(r,t) \tag{B.6}$$

Reordering Equation B.3 it is had

$$\frac{\partial C_t(r,t)}{\partial t} = lap[D_b C_b(r,t) + D_s C_s(r,t)] + \beta \tag{B.7}$$

where $\beta = \beta_s + \beta_b$. At this point [113] introduces the quasi-stationary approach in which intra-granular bubbles are saturated:

$$gC_s = bC_b \tag{B.8}$$

The combination of Equation B.6 and Equation B.8 yields the following equations:

$$\begin{aligned} C_s(r,t) &= \frac{b(t)}{b(t)+g(t)} C_t(r,t) \\ C_b(r,t) &= \frac{g(t)}{(b(t)+g(t)} C_t(r,t) \end{aligned} \tag{B.9}$$

Where now the Equation B.9 becomes:

$$\frac{\partial C_t(r,t)}{\partial t} = lap\left[D_b \frac{b(t)}{b(t)+g(t)} C_t(r,t) + D_s \frac{g(t)}{(b(t)+g(t)} C_t(r,t) C_t(r,t) \right] + \beta \tag{B.10}$$

Finally, this later equation can be further simplified, attaining Equation 5.3 in Subsection 5.2.2.

Commonly, a boundary condition in a spherical or cylindrical geometry is the continuity of the flux in the centerline

$$\left(\frac{\partial C_t(r,t)}{\partial r} \right)_{r=0} < \infty \tag{B.11}$$

The second boundary condition imposed from the original Booth's model [112] is the null concentration at the periphery of the spherical grain $C_t(r = 0, t) = 0$. This in principle can bring out the controversy with the inter-granular fission gas model of setting a saturation concentration from which the gas is released out. However, this condition implies that once the gas atom reaches the grain boundary, it can not enter again. To conclude, the initial condition is the null gas atom concentration at time zero, $C_t(r, t = 0) = 0$.

Bibliography

[1] M. Lung, “A present review of the thorium nuclear fuel cycles,” Tech. Rep. EUR 17771, European Commission, 1997.

[2] J. Somers, D. Papaioannou, J. McGinley, and D. Sommer, “Safety assessment of plutonium mixed oxide fuel irradiated up to 37.7 GW day tonne^{-1},” *Journal of Nuclear Materials*, vol. 437", pp. 303–309, February 2013.

[3] D. R. Olander, *Fundamental Aspects of Nuclear Reactor Fuel Elements*. No. TID-26711-P1 in ISSN 1865-3529, National Technical Information Service, U.S. Department of Commerce, Springfield, Virginia 22161: Technical Information Center, Office of Public Affairs, Energy Research and Development Administration, April 1976.

[4] L. G. Institute, *“Th”, Thorium Suppl*, vol. A3 of *Gmelin handbook of inorganic chemistry*. Springer-Verlag, 8^{t}h ed., 1988.

[5] P. E. Hart, C. W. Griffin, K. A. Hsieh, R. B. Matthews, and G. D. White, “ThO_2-based pellets fuels - their properties, methods of fabrication, and irradiation. A critical assessment of the state of the technology and recommendations for further work,” Tech. Rep. PNL-3064/UC-78, U.S. Department of Energy, September 1979.

[6] J. K. Fink, “Thermophysical properties of uranium dioxide,” *Journal of Nuclear Materials*, vol. 279, pp. 1–18, 2000.

[7] D. Manara, R. Böhler, K. Boboridis, L. Capriotti, A. Quaini, L. Luzzi, F. D. Bruycker, C. Guéneau, N. Dupin, and R. Konings, “The melting behaviour of oxide nuclear fuels: effects on the oxygen potential studied by laser heating,” *Procedia Chemistry*, vol. 7, pp. 505–512, 2012.

[8] J. Belle and R. M. Berman, *Thorium dioxide: Properties and nuclear applications*. DOE/NE-0060, Dist. Catergory UC-25. 78, Naval Reactors Office, United States Department of Energy, 1984.

[9] K. J. Geelhood, W. G. Luscher, and C. E. Beyer, *FRAPCON-3.4:A computer code for the calculation of steady-state thermal behavior of oxide fuel rods for high burnup*. Pacific Northwest National Laboratory, P.O. Box 999, Richland, WA 99352, March 2011.

[10] P. V. Uffelen and V. Sobolev, “Thermomechanical properties for homogeneous (Th,Pu)O_2 fuel,” Tech. Rep. EVOL – OMICO – D - 03, SCK•CEN, 2001.

[11] NEA, *Janis 3-4 User’s guide*. OECD NEA, May 2012.

[12] B. Ade, A. Worrall, J. Powers, S. Bowman, G. Flanagan, and J. Gehin, “Safety and Regulatory Issues of the Thorium Fuel Cycle,” Tech. Rep. NUREG/CR-7176-ORNL/TM-2013/543, Oak Ridge National Laboratory, February 2014.

[13] A. J. Mieloszyk and M. S. Kazimi, "Fuel performance analysis of a (ThU)O_2-fueled, reduced moderation boiling water reactor," *Nuclear Technology*, vol. 191, pp. 268–294, September 2015.

[14] C. Baker, "The fission gas bubble distribution in Uranium Dioxide from high temperature irradiated SGHWR fuel pins," *Journal of Nuclear Materials*, vol. 66, pp. 283–291, August 1976.

[15] R. J. White, "Equi-axed and columnar grain growth in UO_2," in *Proceedings of the IAEA technical committee meeting on water reactor fuel element modelling at high burnup and its experimental support* (IAEA, ed.), p. 419–427, 1994.

[16] S. Brémier, C. Walker, and R. Manzel, "Fission Gas Release and Fuel Swelling at Burn-ups higher than 50 MWd/kg U," in *Fission Gas Behaviour in Water Reactor Fuels* (N. E. Agency, ed.), pp. 93–107, 2000.

[17] L. de Benito, "Transuranus Fission Gas Release Simulation for Thorium-based fuels," master thesis, Technische Universität München, 2016.

[18] M. Suzuki, H. Saitou, Y. Udagawa, and F. Nagase, *Light Water Reactor Fuel Analysis Code, FEMAXI-7; Model and Structure*. Japan Atomic Energy Agency, 2-4 Shirakata Shirane, Tokai-mura, Naka-gun, Ibaraki-ken,319-1195, Japan, July 2013.

[19] D. Sommer, Bruch, Bernett, and Bö, "Thorium Cycle: Development Steps for PWR and ADS Applications," Tech. Rep. Th5-DOC-010, European Commission, December 2001.

[20] V. Sobolev, M. Weber, and T. Aoust, "Preliminary irradiation conditions," Tech. Rep. EVOL – OMICO – D - 02a, SCK•CEN, May 2002.

[21] G. L. Olson, R. K. McCardell, and D. B. Illum, "Fuel Summary Report: Shippingport Light Water Breeder Reactor," Tech. Rep. INEEL/EXT-98-00799, Idaho National Engineering and Environmental Laboratory, Idaho Falls, Idaho 83415, September 2002.

[22] H. C. Hecker, "Nuclear analysis and performance of the Light Water Breeder Reactor (LWBR) core power operation at Shippingport," Tech. Rep. WAPD-TM-1421, Bettis Atomic Power Laboratory, April 1984.

[23] J. W. Sterbentz, "Validation work to support the Idaho National Engineering and Environmental Laboratory calculation burn-up methodology using Shippingport Light Water Breeder Reactor spent fuel assay data," Tech. Rep. INEEL/EXT-99-O0581, Idaho National Engineering and Environmental Laboratory, Idaho Falls, Idaho 83415, August 1999.

[24] C. Grove and A. Worrall, "Comparison of thorium and uranium fuel cycles," Tech. Rep. NNL 11593 Issue 5, National Nuclear Laboratory, March 2012.

[25] O. S. Vălu, O. Beneš, R. J. M. Konings, and H. Hein, "The high temperature heat capacity of the (Th,Pu)O_2 system," *Journal of Chem. Thermodynamics*, vol. 68, pp. 122–127, September 2014.

[26] J. I. T. Cavia, R. Macián-Juan, A. Schubert, J. van Laar, P. V. Uffelen, S. Brémier, P. Pöeml, J. Somers, and M. Seidl, "Extension of the TRANSURANUS burnup model for (Th,Pu)O_2 type fuel in light water reactors," in *39th Enlarged Halden Programme Group Meeting*, 2016.

[27] K. I. Björk, S. Mittag, R. Nabbi, A. Rineiski, O. Schitthelm, and B. Vezzoni, "Irradiation of a thorium-plutonium rodlet: Experiment and benchmark calculations," *Progress in Nuclear Energy*, vol. 66, pp. 73–79, 2013.

[28] J. I. T. Cavia, R. Macián-Juan, M. Seidl, P. V. Uffelen, A. Schubert, S. Brémier, and P. Pöeml, "Transuranus burn-up extension for (Th,Pu)O_2 type fuel in Light Water Reactors," in *TOP Fuel 2015 Proceedings*, 2015.

[29] T. Aoust and V. Kouzminov, "Annex to D2 Neutronic Calculations," Tech. Rep. EVOL – OMICO – D - 02b, SCK•CEN, July 2002.

[30] V. Sobolev and P. V. Uffelen, "Design input data for the fuel segments," Tech. Rep. EVOL – OMICO – D - 01, SCK•CEN, July 2002.

[31] B. Boer, S. Lemehov, M. Wéber, Y. Parthoens, M. Gysemans, J. McGinley, J. Somers, and M. Verwerft, "Irradiaton performance of (Th,Pu)O_2 fuel under Pressurized Water Reactor conditions," *Journal of Nuclear Materials*, vol. 471, pp. 97–109, January 2016.

[32] M. Verwerft, S. E. Lemehov, M. Wéber, L. Vermeeren, P. Gouat, V. Kuzminov, V. Sobolev, Y. Parthoens, B. Vos, S. V. den Berghe, H. Segura, P. Blanpain, J. Somers, G. Toury, J. McGinley, D. Staicu, A. Schubert, P. V. Uffelen, and D. Haas, "Oxide fuels: Microstructure and Composition Variations (OMICO)," Tech. Rep. FIKS-CT-2001-00141, SCK•CEN, 2007.

[33] P. R. Hania and F. C. Klaassen, *Comprehensive nuclear materials*, ch. Thorium Oxide Fuel. Elsevier, North Holland, 2012.

[34] D. Das and S. R. Bharadwaj, *Thoria-based nuclear fuels. Thermophysical and Thermodynamic Properties, Fabrication, Reprocessing and Waste Management*. ISSN 1865-3529, W. Lafayette, Indiana 47907: Springer London Heidelberg New York Dordrecht, April 2013.

[35] K. I. Björk, , S. S. Drera, J. F. Kelly, C. Vitanza, C. Helsengreen, T. Tverberg, M. Sobieska, B. C. Oberländer, H. Tuomisto, L. Kekkonen, J. Wright, U. Bergmann, and D. P. Mathers, "Commercial thorium fuel manufacture and irradiation: Testing (Th,Pu)O_2 and (Th,U)O_2 in the Seven-Thirty program," *Annals of Nuclear Energy*, vol. 75, pp. 79–86, 2015.

[36] M. Verwerft, M. Gysemans, A. D. Bremaecker, O. Schitthelm, R. Nabbi, A. Rineiski, B. Vezzoni, V. Romanello, S. Mittag, S. Kliem, J. McGinley, S. V. Winckel, D. Papaioannou, A. Worral, C. Grove, D. F. da Cruz, R. Hania, F. Klaassen, N. Kivel, R. Restani, M. Martin, P. Darilek, J. Breza, and C. Strmensky, "LWR-Deputy," Tech. Rep. FI6W-036421, SCK•CEN, December 2011.

[37] K. Lassmann, "URANUS- a computer programme for the thermal and mechanical analysis of the fuel rods in a nuclear reactor," *Nuclear Engineering and Design*, vol. 45, pp. 325–342, 1978.

[38] K. Lassmann, C. O'Carroll, J. van de Laar, and C. T. Walker, "The radial distribution of plutonium in high burnup UO_2 fuel," *Journal of Nuclear Materials*, vol. 208, pp. 223–231, October 1994.

[39] K. Lassmann, C. T. Walker, and J. van de Laar, "Extension of the Transuranus burnup model to heavy water reactor conditions," *Journal of Nuclear Materials*, vol. 255, pp. 222–233, January 1998.

[40] A. Schubert, P. V. Uffelen, J. van de Laar, C. T. Walker, and W. Haeck, "Extension of the Transuranus burn-up model," *Journal of Nuclear Materials*, vol. 376, pp. 1–10, 2008.

[41] I. D. Palmer, K. W. Hesketh, and P. A. Jackson, "A Model for Predicting the Radial Power Profile in a Fuel Pin," tech. rep., British Nuclear Fuels Ltd, Springfields Works, Salwick, Preston, 1983.

[42] J. Leppänen, "Serpent- a continuous-energy Monte Carlo reactor physics burnup calculation code," tech. rep., VTT Technical Research Centre of Finland, March 2013.

[43] H. Matzke, "Gas Release Mechanisms in UO_2 - A Critical Review," in *Radiation Effects*, vol. 53, pp. 219–242, Gordon and Breach Science Publishers. Inc, January 1980.

[44] P. Pöeml, S. Brémier, J. Himbert, and J. I. T. Cavia, "LWR Deputy: Electron probe microanalysis of a high burn-up (Th,Pu)O_2 fuel section," Tech. Rep. JRC98186, European Commission, Joint Research Center, 2015.

[45] V. S. Yemel'yanov and A. I. Yevstyukhin, *The metallurgy of nuclear fuel. Properties and principle of the technology of Uranium, Thorium and Plutonium*. 68-18573, Pergamon Press, 1964.

[46] IAEA, "Thorium-based nuclear fuels: Current status and perspectives," Tech. Rep. IAEA-TECDOC-412, IAEA, March 1987.

[47] IAEA, "Thorium fuel cycle – Potential benefits and challenges," Tech. Rep. IAEA-TECDOC-1450, IAEA, May 2005.

[48] S. Peterson, R. E. Adams, and D. A. D. Jr., "Properties of thorium, its alloys, and its compounds," Tech. Rep. ORNL-TM-1144, Oak Ridge National Laboratory, June 1965.

[49] T. R. G. Kutty, A. Kumar, J. P. Panakkal, and H. S. Kamath, "Development and microstructural characterization of ThO_2-UO_2 fuels," *BARC Newsletter*, vol. 314, pp. 28–36, June 2010.

[50] K. Bakker, E. H. P. Cordfunke, R. J. M. Konings, and R. P. C. Schram, "Critial evaluation of the thermal properties of ThO_2 and $Th_{1-y}U_yO_2$ and a survey of the literature data on $Th_{1-y}Pu_yO_2$," *Journal of Nuclear Materials*, vol. 250, pp. 1–12, 1997.

[51] S. Spinner, L. Stone, and F. P. Knudsen, "Temperature dependence of the elastic constants of thoria specimens of varying porosity," *Journal of research of the National Bureau of Standards- C. Engineering and Instrumentation*, vol. 67C, pp. 93–100, January 1963.

[52] M. Hoch, "High-temperature specific heat of UO_2, ThO_2 and Al_2O_3," *Journal of Nuclear Materials*, vol. 130, pp. 94–101, 1985.

[53] L. J. Siefken, E. W. Coryell, E. A. Harvego, and J. K. Hohorst, *MATPRO - A library of material properties for Light Water Reactor Accident Analysis*. Division of Systems Technology Office of Nuclear Regulatory Research U.S. Nuclear Regulatory Commission and Idaho National Engineering and Environmental Laboratory, January 2001.

[54] J. I. T. Cavia, "(Th,Pu)O_2 Material Properties in Transuranus," Tech. Rep. ISBN 978-3-00-050385-6 NTECH-1501, Technische Universitä München, August 2015.

[55] V. Sobolev, "Modelling thermal properties of actinide dioxide fuels," *Journal of Nuclear Materials*, vol. 344, pp. 198–205, 2005.

[56] P. E. M. E. P. Loewen and J. Hoborst, "Recommended thoria materials properties modifications to FRAPCON-3," tech. rep., Idaho National Engineering and Environmental Laboratory, 2000.

[57] R. B. Pinheiro, F. A. N. Carneiro, F. S. Lameiras, R. A. N. Ferreira, W. B. Ferraz, M. S. Dias, M. L. L. Soares, E. P. de Andrade, H. A. Mascarenhas, A. M. M. dos Santos, L. C. M. Pinto, A. Santos, S. A. C. Filgueras, M. J. de O. Lopes, M. Peehs, G. Shlosser, F. Wunderlich, H. Gross, W. Doer, M. Gaertner, G. Kaspar, H. Finnemann, D. Porsch, M. Hrovat, M. Kadner, V. Maly, K. Reichardt, B. G. Brodda, and E. Zimmer, "Program of Research and Development on the Thorium Utilization in PWRs," Tech. Rep. ISBN 3-89336-019-0, Kernforschungsanlage Jülich GmbH, 1988.

[58] J. Spino, J. Rest, W. Goll, and C. T. Walker, "Matrix swelling rate and cavity volume balance of UO_2 fuels at high burn-up," *Journal of Nuclear Materials*, vol. 346, pp. 131–144, June 2005.

[59] Y. S. Touloukian, R. K. Kirby, R. E. Taylor, and T. Y. R. Lee, "Thermophysical properties of matter. thermal expansion in Nonmetallic Solids," Tech. Rep. DSA 900-76-C-0860, Purdue Institutionn, 1970.

[60] IAEA, “Thermophysical properties database of materials for light water reactors and heavy water reactors,” Tech. Rep. IAEA-TECDOC-1496, IAEA, June 2006.

[61] P. G. Lucuta, H. Matzke, and I. J. Hastings, “A pragmatic approach to modelling thermal conductivity of irradiated UO_2 fuel: review and recommendations,” *Journal of Nuclear Materials*, vol. 232, pp. 166–180, 1996.

[62] C. Cozzo, D. Staicu, J. Somers, A. Fernandez, and R. J. M. Konings, “Thermal diffusivity and conductivity of thorium-plutonium mixed oxides,” *Journal of Nuclear Materials*, vol. 416, pp. 135–141, 2011.

[63] M. Murabayashi, “Thermal conductivity of ceramic solid solutions,” *Journal of Nuclear Science and Technology*, vol. 7, pp. 559–563, November 1970.

[64] U. Basak, A. K. Sengupta, and C. Ganguly, “Hot hardness and thermal conductivity of ThO_2-PuO_2 and ThO_2-UO_2 sintered pellets,” *Journal of Materials Science Letters*, vol. 8, pp. 449–450, 1989.

[65] P. Rodriguez and C. V. Sundaram, “Nuclear and materials aspects of the thorium fuel cycle,” *Journal of Nuclear Materials*, vol. 100, pp. 227–249, 19891.

[66] R. J. M. Konings, P. J. A. M. Blankenvoorde, E. H. P. Cordfunke, and K. Bakker, “Evaluation of thorium based nuclear fuel,” Tech. Rep. ECN-R-95-007, Netherlands Energy Research Foundation ECN, July 1995.

[67] J. Weertman, “Theory of steady-state creep based on dislocation climb,” *Journal of Applied Physics*, vol. 26, pp. 1213–1214, 1955.

[68] A. A. Solomon, J. L. Routbort, and J. C. Voglewede, “Evaluation of thorium based nuclear fuel,” Tech. Rep. ANL-7857, Argonne National Laboratory, Materials Science Division, September 1971.

[69] A. A. Solomon, C. S. Yust, and N. H. Packan, “Primary creep of UO_2 and the effect of amorphous grain boundary phases,” *Journal of Nuclear Materials*, vol. 110, pp. 333–342, February 1982.

[70] K. M. Cochran and A. A. Solomon, “Fabrication and creep testing of UO_2 tensile specimens,” *Journal of Nuclear Materials*, vol. 119, pp. 162–169, August 1983.

[71] L. E. Poteat and C. S. Yust, “Creep of polycrystalline thorium dioxide,” in *Sixty-Seventh Annual Meeting, The American Ceramic Society*, March 1966.

[72] S. K. Evans, P. E. Bohaboy, and R. A. Laskiewicz, “Compressive creep of urania-plutonia fuels,” Tech. Rep. GEAP-13732, General Electric Company, August 1971.

[73] A. R. Massih, “Models for MOX fuel behaviour,” Tech. Rep. SKI Report 2006:10, Quantum Technologies AB, January 2006.

[74] A. L. B. Jr., “Tensile properties of irradiated thorium,” *Journal of Nuclear Materials*, vol. 6, pp. 969–83, 1962.

[75] S. Dash, S. C. Parida, Z. Singh, B. K. Ken, and V. Venugopal, "Thermodynamic investigations of ThO_2-UO_2 solid solutions," *Journal of Nuclear Materials*, vol. 393, pp. 267–281, June 2009.

[76] A. C. Victor and T. B. Douglas, "Thermodynamic properties of thorium dioxide from 298 to 1200 K," *Journal of Research of the National Bureau of Standards*, vol. 65, pp. 105–111, November 1960.

[77] H. Serizawa and Y. Arai, "An examination of the estimation method for the specific heat of TRU dioxides: evaluation with PuO_2," *Journal of Alloys and Compounds*, vol. 312, pp. 257–264, June 2000.

[78] S. G. Popov, J. J. Carbajo, V. K. Ivanov, and G. L. Yoder, "Thermophysical Properties of MOX and UO_2 Fuels including the effects of irradiation," Tech. Rep. ORNL/TM-2000/351, Oak Ridge National Laboratory, November 2000.

[79] European Commission, Joint Research Centre, Institute for Transuranium Elements, Postfach 2340, D-76125 Karlsruhe, *Transuranus Handbook*, v1m3j14 ed., September 2014.

[80] S. Peterson, R. E. Adams, and D. A. Douglas, "Properties of thorium, its alloys, and its compounds," Tech. Rep. ORNL-TM-1144, Oak Ridge National Laboratory, June 1965.

[81] J. H. Harding, D. G. Martin, and P. E. Potter, "Thermophysical and thermomechanical properties of fast reactor materials," Tech. Rep. EUR 12402, Commission of the European Communities, 1989.

[82] S. S. Drera and K. I. Björk, "Thorium fuel production and results from beginning of life irradiation," *Progress in Nuclear Energy*, pp. 1–6, 2013.

[83] K. W. Kang, J. H. Yang, K. S. Kim, K. W. Song, C. B. Lee, and Y. H. Jung, "(Th,U)O_2 Pellets: Fabrication and Thermal Properties," *Journal of the Korean Nuclear Society*, vol. 35, pp. 299–308, August 2003.

[84] A. G. Croff, *A User's Manual for the ORIGEN2 Computer Code*. Oak Ridge National Laboratory, July 1980.

[85] S. Yagnik, "Fuel performance analysis capability in FALCON," tech. rep., EPRI, Palo Alto, CA, USA, December 2002.

[86] J. Hales, S. R. Novascone, G. Pastore, D. M. Perez, B. W. Spencer, and R. L. Williamson, "BISON theory manual," tech. rep., INL, Idaho Falls, ID, USA, October 2013.

[87] K. T. Clarno, B. Philip, W. K. Cochran, R. S. Sampath, S. Allu, P. Barai, S. Simunovic, M. A. Berrill, L. J. Ott, S. Pannala, G. A. Dilts, B. Mihaila, G. Yesilyurt, J. H. Lee, and J. E. Banfield, "The AMP (Advanced MultiPhysics) nuclear nuel performance code," *Nuclear Engineering and Design*, vol. 252, pp. 108–120, 2012.

[88] S. Lemehov, J. Nakamura, and M. Suzuki, "Pluton: A three-group model for the radial distribution of plutonium, burnup and power profiles in highly irradiated LWR fuel rods," *Nuclear Technology*, vol. 133, pp. 153–168, February 2001.

[89] A. Soba, A. Denis, L. Romero, E. Villarino, and F. Sardella, "A high burnup model developed for the DIONISIO code," *Journal of Nuclear Materials*, vol. 433, pp. 160–166, 2013.

[90] K. I. Björk and P. Fredriksson, "Development of a fuel performance code for thorium-plutonium fuel," in *PHYSOR 2014- The Role of Reactor Physics toward a Sustainable Future*, 2014.

[91] H. Kleykamp, "The Chemical State of the Fission Products in Oxide Fuels," *Journal of Nuclear Materials*, vol. 131, pp. 221–246, October 1984.

[92] P. Blair, *Modelling of Fission Gas Behaviour in High Burn-up Nuclear Fuel*. PhD thesis, École Polytechnicque Fédérale de Lausanne, July 2008.

[93] Y. Yun, P. Oppeneer, H. Kim, and K. Park, "Defect energetics and Xe diffusion in UO_2 and ThO_2," *Acta Materialia*, vol. 57, pp. 1655–1659, January 2009.

[94] K. Shiba, A. Itoh, and M. Akabori, "The mechanisms of fission gas release from (Th,U)O_2," *Journal of Nuclear Materials*, vol. 126, pp. 18–24, April 1984.

[95] P. V. Uffelen, *Contribution to the Modelling of Fission Gas Release in Light Water Reactor Fuel*. PhD thesis, Université de Liége, 2002.

[96] J. A. Turnbull, "A Review of Irradiation Induced Re-solution in Oxide Fuels," in *Radiation Effects*, vol. 53, pp. 243–250, Gordon and Breach Science Publishers. Inc, January 1980.

[97] H. Blank, "Fission Fragment Re-solution Mechanisms," Tech. Rep. EUR 6600, Commission of the European Communities, European Institute for Transuranium Elements, Postfach 2266, D-7500 Karlsruhe, Germany, September 1979.

[98] R. White and M. Tucker, "A new Fission-Gas Release Model," *Journal of Nuclear Materials*, vol. 118, pp. 1–38, April 1983.

[99] G. Pastore, L. P. Swiler, J. D. Hales, S. R. Novascone, D. M. Perez, B. W. Spencer, L. Luzzi, P. V. Uffelen, and R. L. Williamson, "Uncertainty and sensitivity of fission gas behavior in engineering-scale fuel modeling," *Journal of Nuclear Materials*, vol. 456, pp. 398–408, October 2014.

[100] R. Hargreaves and D. A. Collins, "A quantitative model for fission gas release and swelling in irradiated uranium dioxide," *J. Brit. Nucl. Energy Soc.*, vol. 15, pp. 311–318, October 1976.

[101] V. F. Chkuaseli and H. Matzke, "Fission gas bubble behaviour in uranium dioxide," *Journal of Nuclear Materials*, vol. 201, pp. 92–96, October 1993.

[102] J. A. Turnbull, “The distribution of intragranular fission gas bubbles in UO_2 during irradiation,” *Journal of Nuclear Materials*, vol. 38, pp. 203–212, October 1971.

[103] R. M. Cornell, M. V. Speight, and B. C. Masters, “The Role of Bubbles in Fission Gas Release from Uranium Dioxide,” *Journal of Nuclear Materials*, vol. 30, pp. 170–178, 1969.

[104] R. J. White, “The development of grain-face porosity in irradiated oxide fuel,” *Journal of Nuclear Materials*, vol. 325, pp. 161–77, 2004.

[105] I. Goldberg, G. L. Sphar, L. S. White, L. A. Waldman, J. F. Giovengo, P. L. Pfennigwerth, and J. Sherman, “Fission gas release from ThO_2 and ThO_2-UO_2 fuels,” Tech. Rep. WAPD-TM-1350, Bettis Atomic Power Laboratory, West Mifflin, Pennsylvania, August 1978.

[106] J. F. Giovengo, I. Goldberg, and C. D. Sphar, “Fission-gas release from high-burn-up ThO_2 and ThO_2-UO_2 fuels irradiated at low temperature,” Tech. Rep. WAPDTM-1350, Bettis Atomic Power Laboratory, West Mifflin, Pennsylvania, May 1982.

[107] M. Akabori and K. Fukuda, “Release behavior of cesium in irradiated (Th,U)O_2,” *Journal of Nuclear Materials*, vol. 186, pp. 47–53, July 1991.

[108] K. N. G. Kaimal, A. S. Kerkar, A. N. Shirsat, D. Das, A. Datta, A. G. C. Nair, and S. B. Manohar, “Transport properties of iodine and tellurium in a thoria-2mol% urania matrix,” *Journal of Nuclear Materials*, vol. 317, pp. 189–194, January 2003.

[109] H. Kim, K. Park, B. G. Kim, Y. S. Choo, and W. S. Ryu, “Diffusion of Xenon Gas in Nuclear Fuels with Oxygen Potentials in 0.1 MWd/tU of a Burnup,” Tech. Rep. IAEA-TECDOC-CD-1635, IAEA-TECDOC-CD-1635, Vienna International Centre PO Box 100, 1400 Vienna, Austria, December 2009.

[110] A. N. Shirsat, M. A. Basu, S. Kolay, A. Datta, and D. Das, “Transport properties of I, Te and Xe in thoria-urania SIMFUEL,” *Journal of Nuclear Materials*, vol. 382, pp. 16–21, March 2009.

[111] IAEA, “Fuel Modelling at Extended Burnup (FUMEX-II),” tech. rep., IAEA, 2012.

[112] A. H. Booth, “A method of calculating fission gas diffusion from UO_2 fuel and its application to the X-2-f Loop Test,” Tech. Rep. CRDC-72, Atomic Energy of Canada Limited Chalk River Project Research and Development, September 1957.

[113] M. V. Speight, “A Calculation on the Migration of Fission Gas in Material Exhibiting Precipitation and Re-solution of Gas Atoms Under Irradiation,” *Nuclear Science and Engineering*, vol. 37, pp. 180–185, March 1969.

[114] P. V. Uffelen, G. Pastore, V. D. Marcello, and L. Luzzi, “Multiscale modelling for the fission gas behaviour in the TRANSURANUS code,” *Nuclear engineering and technology*, vol. 43, pp. 477–488, December 2011.

[115] K.Lassmann and H. Benk, "Numerical algorithms for intragranular fission gas release," *Journal of Nuclear Materials*, vol. 280, pp. 127–135, March 2000.

[116] J. A. Turnbull and C. E. Beyer, "Background and Derivation of ANS-5.4 Standard Fission Product Release Model," Tech. Rep. NUREG/CR-7003-PNNL-18490, USNRC, Pacific Northwest National Laboratory, January 2010.

[117] P. Lösönen, "Methods for calculating diffusional gas release from spherical grains," *Journal of Nuclear Materials*, vol. 325, pp. 61–77, 2004.

[118] K. Forsberg and A. R. Massih, "Diffusion theory of fission gas migration in irradiated nuclear fuel UO_2," *Journal of Nuclear Materials*, vol. 135, pp. 140–148, May 1985.

[119] K. Forsberg and A. R. Massih, "Fission gas release under time-varying conditions," *Journal of Nuclear Materials*, vol. 127, pp. 141–145, September 1985.

[120] P. T. Elton and K. Lassmann, "Calculation methods for diffusional gas release," *Nuclear Engineering and Design*, vol. 101, pp. 259–265, 1987.

[121] D. Pizzocri, C. Rabiti, T. Barani, P. V. Uffelen, and G. Pastore, "Polypole-1: An accurate numerical algorithm for intra-granular fission gas release," *Journal of Nuclear Materials*, vol. 478, pp. 333–342, 2016.

[122] M. C. Naik, *Diffusion processes in nuclear materials*, ch. Diffusion controlled and burst release of gaseous and volatile fission products from UO_2 and ThO_2. Elsevier, North Holland, 1992.

[123] K. Shiba, *Diffusion processes in nuclear materials*, ch. Diffusion controlled and burst release of gaseous and volatile fission products from UO_2 and ThO_2. Elsevier, North Holland, 1992.

[124] Y. Long, *Modelling the Performance of High Burnup Thoria and Urania PWR Fuel*. PhD thesis, Massachusetts Institute of Technology, Institute of Technology - Cambridge, MA 01239, USA, May 2002.

[125] M. Basu, R. Mishra, S. R. Bharadwaj, and D. Das, "Thermodynamic and transport properties of thoria-urania fuel of Advanced Heavy Water Reactor," *Journal of Nuclear Materials*, vol. 403, pp. 204–215, January 2010.

[126] D. M. Dowling, R. J. White, and M. O. Tucker, "The effect of irradiation-induced resolution on fission gas release," *Journal of Nuclear Materials*, vol. 110, pp. 37–46, March 1982.

[127] A. C. Martínez, *Mecánica de Fluidos*. ISBN 84-9732-292-4, Magallanes 25, 28015 Madrid, Spain: Thomson, 2006.

[128] G. C. Benson and E. Dempsey, "Cohesive and surface energies of some crystals possessing the fuorite structure," *Proc. Roy. Soc*, vol. A266, pp. 43–47, May 1962.

[129] P. S. Maiya, “Surface diffusion, surface free energy, and grain-boundary free energy of uranium dioxide,” *Journal of Nuclear Materials*, vol. 40, pp. 57–65, January 1971.

[130] Y. Y. Koo, B. H. Lee, and D. S. Sohn, “Cosmos: a computer code to analyze LWR UO_2 and MOX fuel up to high burnup,” *Annals of Nuclear Energy*, vol. 26, pp. 47–67, December 1999.

[131] C. Walker, “Electron probe microanalysis of irradiated nuclear fuel: an overview,” *Journal of Analytical Atomic Spectrometry*, vol. 14, pp. 447–454, 1998.

[132] E. Villarino, R. J. J. Stammler, A. Ferri, and J. J. Casal, “HELIOS: Angularly Dependent Collision Probabilities,” *Nuclar Science and Engineering*, vol. 112, pp. 16–31, 1992.

[133] H. Matzke, “Atomic Mechanisms of Mass Transport in Ceramic Nuclear Fuel Materials,” *Journal Chemistry Soc. Farady. Trans.*, vol. 86, pp. 1243–1256, January 1990.

[134] M. Pusa and J. Leppänen, “Computing the Matrix Exponential in Burnup Calculations,” *Nuclar Science and Engineering*, vol. 164, pp. 140–150, 2010.

[135] M. Pusa, “Solving linear systems with sparse gaussian elimination in teh chebyshev rational approximation method (cram),” *Nuclar Science and Engineering*, vol. 164, pp. 1–14, 2013.

[136] A. Schubert, P. V. Uffelen, H. Segura, M. Verwerft, and S. Lemehov, “Comparison of fuel performance calculations for the OMICO irradiation experiment,” tech. rep., European Commission, Joint Research Centre, Institute for Transuranium Elements, June 2007.

[137] R. Atherton, “Water cooled breeder program summary report,” Tech. Rep. WAPD-TM-1600, Bettis Atomic Power Laboratory, October 1987.

[138] J. J. Duderstadt and L. J. Hamilton, *Nuclear Reactor Analysis*. ISBN 0-471-22363-8, Ann Arbor, Michigan: Department of Nuclear Engineering, the University of Michigan, February 1975.

[139] Y. Yun and P. M. Oppeneer, “First-principles design of next-generation nuclear fuels,” *Materials Research Society*, vol. 36, pp. 178–184, March 2011.

[140] M. Streit, T. Tverberg, W. Wiesenack, and F. Vettraino, “Inert matrix and thoria fuel irradiation at an international research reactor,” *Journal of Nuclear Materials*, vol. 352, pp. 263–267, 2006.

[141] C. B. Lee, Y. S. Yang, D. H. Kim, S. K. Kim, and J. G. Bang, “A New Mechanistic and Engineering Fission Gas Release Model for a Uranium Dioxide Fuel,” *Journal of Nuclear Science and Technology*, vol. 45, pp. 60–71, October 2007.

[142] N. G. Herranz, “Curso de diseño de reactores nucleares, ETSII.” Chapters 4 and 5.

[143] E. E. Lewis and W. F. M. Jr., *Computational methods of neutron transport*. ISBN 0-89448-452-4, 555 N. Kensington Avenue, La Grange Park, Illinois 60525 USA: American Nuclear Society, Inc, June 1984.

[144] W. M. Stacey, *Nuclear Reactor Physics*. ISBN 0-471-22363-8, Wiley-VCH, 2007.